

A Study of Rapidly Solidified Al1.5wt%/3wt%Mg0.2wt%Sc Powders and Strips using
Impulse Atomization

By

Shengze Yin

A thesis submitted in partial fulfillment of the requirements for the degree of

Master of Science
in
Materials Engineering

Department of Chemical and Materials Engineering
University of Alberta

© Shengze Yin, 2016

Abstract

In this work, rapid solidification microstructures and mechanical properties of Al_{1.5}Mg_{0.2}Sc and Al₃Mg_{0.2}Sc are investigated. Samples in the form of powders and strips / deposits of different thermal histories are obtained by means of impulse atomization technique. Cooling rates of the powders, varying from 300K/s to 900K/s within the investigated size range, are estimated using a thermal model of a solidifying droplet in a stagnant gas. Whereas cooling rates of the strips are measured by a two-color pyrometer at the strip-substrate interface and is found to average 1.7K/s.

The effects of Mg content, cooling rate and melt superheat on the scale of microstructures and mechanical properties are investigated. The role of Sc is also analyzed.

The increase in Mg content and cooling rate are found to yield finer microstructures. For both powders and strips, a reduction in cell spacing is found to have limited impacts on microhardness. However, increasing Mg content (from 1.5wt% to 3wt %) is found to have a strengthening effect estimated by a hardness value of about 20 HV_{0.1}. While cell spacing of the powders is found to increase with melt superheat, no noticeable difference in cell spacing or microhardness is observed.

The effects of heat treatment on mechanical properties is also investigated. Aging of the as-atomized powders and strips are carried out at 300 °C for up to 2 hours in a DSC. Microhardness is measured on both as-atomized and aged samples. Maximum hardness is reached for both powders and strips after 2 hours of aging. For both alloy compositions, a hardness increase of 40 HV_{0.1} is obtained. From DSC results and phase diagram, Sc precipitation is found to be responsible for the aging response.

Compared with published industrial data on cooling rate, cell spacing, and response to aging, the combinations of the impulse atomization and impulse atomization with spray deposition exhibit the possibility of being used as a small scale platform for novel alloys testing and development for industrialized rapid solidification processes, such as twin-belt strip casting process.

Acknowledgements

There is an old saying in Chinese “高树靡阴, 独木不林”, which means: the taller the tree, the lesser the shade it provides; also, no single tree could be considered as a forest, no matter what kind of tree it is. The first part of this saying, in my mind, suggests that a scientific research, should aim of helping mankind improve our knowledge of the world and solving the real issues we dealt with. The second part of this saying shows a simple fact: everyone needs someone to achieve great things. Therefore, I would like to acknowledge the people who helped me in this section.

I am very grateful to my parents, Chunguang Yin and Shuyu Sun, for showing me their unconditional love and support throughout my life. I would also like to show my deepest appreciation for Dr. Hani Henein, who shows and helps me on how to do a scientific research and more importantly, how to be a scientific researcher. I would like to thank Dr. Mark Gallerneault and Dr. Vahid Fallah for their help me gain a deeper understanding in the field of this work.

My girlfriend Chenxin Zhou and my dearest friends (who are also my co-workers in the lab) Pusong Wang and Abdoul-Aziz Bogno have always been there for me whenever I needed them. I could not thank them enough.

I also want to thank Dr. J. B. Wiskel for helping me understand his thermal model and giving me suggestions on the temperature measurements. I thank my group members in AMPL (Jacob, Pooya, Jonas, Carlos, Mohsen, Billy, and the rest of them) for the companionship they provided me in the past few years.

Last but not the least, I would like to thank NSERC, Novellis, Alcerco, and ANR for funding this project. Without them, none of this is possible.

Table of Contents

Abstract.....	ii
Acknowledgements.....	iii
List of Tables	vii
List of Figures.....	viii
1. Introduction.....	1
2. Literature review	3
2.1. Al-Mg alloy.....	3
2.2. Strengthening of Al-Mg alloys	4
2.3. Sc addition in Al and Al-Mg alloys	8
2.4. Casting of Al alloys	11
2.5. Rapid solidification.....	12
2.6. Impulse atomization.....	14
2.7. Strip Casted Al-Mg-Sc Alloys.....	17
2.8. Summary	19
2.9. Objectives	19
3. Experiments and Results.....	21
3.1. Sample production	22
3.1.1. Impulse Atomization.....	22
3.1.2. Impulse Atomization with Spray Deposition.....	24
3.1.3. Sample Produced	25
3.2. Temperature Measurement	26
3.3. Sample Analysis.....	36
3.3.1. Sieving	36
3.3.2. Metallography.....	37

3.3.3. Inductively Coupled Plasma (ICP)	40
3.3.4. Cell spacing measurement	41
3.3.5. Microhardness measurements	47
3.3.6. Aging.....	49
3.4. Summary	50
4. Discussion	52
4.1. Thermal Profile	52
4.1.1. Thermal Model.....	52
4.1.2. Interface temperature measurement	56
4.2. Cell Spacing and Cooling Rate	60
4.2.1. Powder	60
4.2.2. Spray deposit.....	64
4.3. Microhardness.....	65
4.3.1. Powders.....	65
4.3.2. Spray deposit.....	67
4.3.3. Cell Spacing vs. Microhardness.....	68
4.4. Age Hardening	69
4.4.1. Age Hardening Effect on Powders	70
4.4.2. Spray deposits	72
4.4.3. DSC.....	74
4.5. Industrial Relevance.....	78
4.6. Summary	80
5. Conclusions and Future Work	82
5.1. Conclusions.....	82
5.2. Future Works	83

References.....	84
Appendix.....	92
Calculations for θ and h	92
Calibration profile for K-type thermocouples.....	93

List of Tables

Table 2.1. Classification of solidification based on cooling rates [41].....	13
Table 3.1: Runs done in this study.....	25
Table 3.2: Emissivity probe and infrared camera calibration data	33
Table 3.3: Temperature recorded against hole-size	34
Table 3.4: Calibration data by changing the emissivity slope	35
Table 3.5: Sieve Data for Al3Mg0.2Sc_Ar	36
Table 3.6: D ₅₀ and R ² from sieve analysis	37
Table 3.7: Polishing procedure suggested by the manufacturer	38
Table 3.8: Suggested etchant and procedure.....	38
Table 3.9: ICP Result.....	40
Table 3.10: Segregating power of elements in aluminum [60].....	44
Table 4.1: Material properties used in thermal model	52
Table 4.2: Summary of thermal model result for spray deposition runs	56
Table 4.3: Calculated constant B	63

List of Figures

Figure 2.1: Al-Mg phase diagram [19]	4
Figure 2.2: Solute concentration in percent weight to the increase in yield strength	5
Figure 2.3: Alloying elements in atomic percent to tensile strength [23].....	6
Figure 2.4: Rolling strain vs. tensile strength for pure aluminum and Al-Mg alloys during cold rolling [24]	7
Figure 2.5: (a)Al-Sc phase diagrams; (b) Al corner in Al-Sc phase diagram [29]	8
Figure 2.6: Precipitates size's effect on CRSS [23].....	10
Figure 2.7. The change in scale of the structure as the cooling rates are increased [42]..	13
Figure 2.8. Schematic of impulse atomization process [12].....	14
Figure 2.9. Cell spacing of Al-5%Cu and Al-17% Cu droplets atomized in N ₂ and He. .	17
Figure 2.10: Vickers hardness for as-cast Al ₃ Mg and Al ₃ Mg _{0.4} Sc at different temperature and holding different time period [4].....	18
Figure 2.11: Bright field TEM images; Al ₃ Sc precipitates during aging [4].....	18
Figure 3.1: Schematic of the AMPL IA tower [10].....	22
Figure 3.2: Schematic of the IASP set-up [10].....	24
Figure 3.3: Sample produced from (a)IA and (b) IASD.....	25
Figure 3.4: The schematic of temperature measuring setup	26
Figure 3.5: Simplified block diagram of the emissivity probe [48].....	27
Figure 3.6: Schematic of measuring position	28
Figure 3.7: Transmission rate vs. Wavelength (μm) for (a) Germanium IR window with 3-12 μm AR coating and (b) Uncoated Calcium Fluoride window [50, 51]	29
Figure 3.8: Schematic of the fiber optic head [56]	31
Figure 3.9: (a)Schematic drawing of the fiber optic lens; (b) fiber optic installed onto the substrate support with a holder	32
Figure 3.10: Calibration setup to test the effect of small holes	33
Figure 3.11: Schematic of the test for the effect of the emissivity slope.....	35
Figure 3.12: lnD vs. z-factor for Al _{1.5} Mg _{0.2} Sc and Al ₃ Mg _{0.2} Sc powders.....	37
Figure 3.13: Al ₃ Mg _{0.2} Sc_Ar_600-710 etched with 1ml HF and 200 ml water and swabbed with cotton for 15 s	39

Figure 3.14: Al ₃ Mg _{0.2} Sc_ 710-850 powder etched by Keller’s etchant for (a); (b)	39
Figure 3.15: Cell spacing measurement procedure.....	41
Figure 3.16: Cell spacing for Al _{1.5} Mg _{0.2} Sc and Al ₃ Mg _{0.2} Sc powders.....	42
Figure 3.17: Constitutional undercooling region in the front of a dendritic tip [60].....	44
Figure 3.18: Sample images of strip Al ₃ Mg _{0.2} Sc_900°C.....	45
Figure 3.19: Cell spacing for Al _{1.5} Mg _{0.2} Sc_800 and Al ₃ Mg _{0.2} Sc_800 deposits at different sampling locations.....	46
Figure 3.20: Cell spacing for Al _{1.5} Mg _{0.2} Sc and Al ₃ Mg _{0.2} Sc deposits	47
Figure 3.21: Al _{1.5} Mg _{0.2} Sc_Ar_250-300 with 10s dwell time	48
Figure 3.22: DSC curve for Al _{1.5} Mg _{0.2} Sc powders with 710-850 μm size range.....	50
Figure 3.23: DSC curve for Al _{1.5} Mg _{0.2} Sc powders with 710-850 μm size range subtracted by the pure aluminum baseline	50
Figure 4.1: Al _{1.5} Mg _{0.2} Sc Scheil solidification path	53
Figure 4-2: Curve fitting Scheil solidification path for Al _{1.5} Mg _{0.2} Sc.....	54
Figure 4-3: Powder size vs. cooling rate for Al _{1.5} Mg _{0.2} Sc and Al ₃ Mg _{0.2} Sc	55
Figure 4.4: Emissivity Probe reading for Al _{4.5} Cu	57
Figure 4.5: Two color pyrometer reading for Al _{4.5} Cu.....	58
Figure 4.6: Emissivity Probe reading for Al ₃ Mg _{0.2} Sc	59
Figure 4.7: Two color pyrometer reading for Al ₃ Mg _{0.2} Sc.....	59
Figure 4.8: Cell spacing vs. cooling rate for Al _{1.5} Mg _{0.2} Sc and Al ₃ Mg _{0.2} Sc powders .	61
Figure 4.9: The pre-exponential factor M change with temperature	62
Figure 4.10: Cell spacing for Al _{1.5} Mg _{0.2} Sc_800 and Al ₃ Mg _{0.2} Sc_800 deposits at different sampling locations.....	64
Figure 4.11: Cell spacing for Al _{1.5} Mg _{0.2} Sc and Al ₃ Mg _{0.2} Sc deposits	65
Figure 4.12: Microhardness for Al _{1.5} Mg _{0.2} Sc and Al ₃ Mg _{0.2} Sc powders	66
Figure 4.13: Microhardness for Al _{1.5} Mg _{0.2} Sc_900 and Al ₃ Mg _{0.2} Sc_900 at different axial locations	67
Figure 4.14: Microhardness for Al _{1.5} Mg _{0.2} Sc and Al ₃ Mg _{0.2} Sc deposits.....	68
Figure 4.15: Microhardness for Al _{1.5} Mg _{0.2} Sc and Al ₃ Mg _{0.2} Sc deposits.....	69
Figure 4.16: Microhardness for Al _{1.5} Mg _{0.2} Sc powders aged at 300 °C.....	70
Figure 4.17: Microhardness for Al ₃ Mg _{0.2} Sc powders aged at 300 °C.....	71

Figure 4.18: Microhardness for Al _{1.5} Mg _{0.2} Sc deposits aged at 300 °C	72
Figure 4.19: Microhardness for Al ₃ Mg _{0.2} Sc deposits aged at 300 °C	73
Figure 4.20: DSC result for two trials done on Al _{1.5} Mg _{0.2} Sc powders in 600-710µm diameter size range	75
Figure 4.21: A corner of Al-Mg-Sc ternary phase diagram at 300°C.....	75
Figure 4.22: TEM micrograph of Al ₃ Sc precipitates for Al-2wt%Mg-0.2wt%Sc aged at 300°C for 24 hrs [5]	76
Figure 4.23: Al ₃ Sc precipitates radius growth at the different aging time under different aging temperature. [72].....	77
Figure 4.24: Random walk distance vs. time.....	78
Figure 4.25: Al ₃ Mg _{0.4} Sc as-casted grain structure [4].....	79
Figure 4.26: Vickers microhardness vs. aging time for Al ₂ Mg _{0.2} Sc at 300°C [5].....	80

1. Introduction

Aluminum and its alloys receive much attention due to their high strength to density ratio and excellent resistance to corrosion. They have been widely used in automotive, aerospace, food packing and some chemical processing applications [1]. With the addition of Mg, improved mechanical properties are achieved through solid solution hardening and strain strengthening. However, a high Mg content would lead to a higher possibility of stress corrosion cracking [2]. If a higher strength is sought after without compromising Al-Mg alloy's resistance to corrosion, an alternative method should be applied.

Sc is reported to strengthen Al and Al-Mg alloys effectively even with a small addition. The strengthening of Sc addition in Al is achieved through precipitation hardening [3]. Supersaturation of Sc in the aluminum matrix is required to reach a good aging effect. For traditional Direct Chill (DC) casting, the cooling rates are reported in the range of 1K/s to 10K/s [4]. With such low cooling rates, a good supersaturation of Sc generally has to be obtained after casting, by homogenization or solutionizing and quenching. Due to the low solubility and diffusivity of Sc in aluminum, this process is carried at a very high temperature (around 620°C) for a relatively extensive period (about 20 hours) [5].

Rapid solidification processing could be used so that the Sc will be supersaturated in solidified condition and therefore, eliminate the energy and time-consuming steps, such as homogenization, hot rolling, solutionizing, and quenching. Semi-continuous DC casting, spray forming, or powder metallurgy processed Al-Mg-Sc alloys showed better mechanical properties after aging without the additional supersaturation steps due to their high cooling rate [6] [7] [8]. Due to the high cost of Sc (\$134/g of 99.9%Sc ingot or \$220/kg of an Al-2%Sc master alloy in 2015 in USD [9]), it is important to determine the most cost effective addition of Sc for strengthening at minimal cost. Based on a previous research, it is suggested that for twin-belt casted Al₃Mg_{0.4}Sc strips, only about 80% of the 0.4wt%Sc added contributes to the age hardening behavior and therefore, less Sc could be used to achieve a similar strengthening. This work aims to study the strengthening effect of a lower Sc level (0.2wt %) in an Al alloy with two different Mg levels.

To achieve a rapid solidification, Impulse Atomization (IA) and IA with spray deposition (IASD) process were in this study. Both of these techniques are developed in the Advanced Materials and Processing Laboratory (AMPL). IA has shown the ability to achieve a cooling rate in the range of 10^2 - 10^4 K/s [10]; while IASD utilizes the droplets produced by IA to form a strip on a moving substrate with controlled dimensions [11]. Their heat profile during IA was simulated by the use of a thermal model reported in [12] [13]. A temperature measurement setup was developed in this work to monitor the heat profile of strips deposited during spray deposition. Cell spacing measurements and microhardness measurements were performed on the produced powders and strips. The age hardening effect of Sc was investigated by furnace aging and Differential Scanning Calorimetry (DSC) aging of the produced powders and strips.

This study will be described in this thesis using the following structure. In Chapter 2, a literature review of the background research will be shown followed by the objective and scope of this study. The experimental setups and procedures for this work and the corresponding preliminary results will be presented in Chapter 3. Chapter 4 will be of the analysis and discussions of the results. Finally, in Chapter 5, the conclusions from this work will be drawn along with the proposed work for the future.

2. Literature review

In this chapter, the advantages of aluminum magnesium (Al-Mg) alloy will be presented first. To understand the reasoning behind the excellent properties of Al-Mg alloys comparing to pure aluminum, strengthening mechanisms for Mg additions in aluminum will be discussed. To achieve for a better mechanical property, the addition of Sc to Al-Mg alloys will be presented along with the precipitation hardening mechanism for the Sc addition. After discussions of Al-Mg and Al-Mg-Sc alloys, their traditional casting processing methods will be introduced, and the need for rapid solidification will be established. The method used to achieve a high cooling rate during solidification process in this study, IA, will then be introduce. At the end, the objectives formulated based on the findings from literature review will be listed.

2.1. Al-Mg alloy

Aluminum is the most abundant structural metal on earth (8wt% of the earth's crust) and the most consumed non-ferrous metal (24 million tons per year) in the world [14] [15]. Aluminum and its alloys feature a combination of low density, high strength, and good corrosion resistance. Their applications include automobiles, packing of food and beverages, construction of buildings, production of defense and aerospace equipment and many others [14]. Besides these conventional applications, aluminum and its alloys also can be found in the trendy additive manufacturing industry, such as ultrasonic additive manufacturing, laser additive manufacturing, wire and arc additive manufacturing in their form of powders [16] [17].

Among all the aluminum alloys, the 5000 series aluminum-magnesium alloys stand out due to their outstanding strength and corrosion resistance. Al-Mg alloys with low Mg contents also feature excellent formability and surface finishing [18]. Al-Mg alloys are widely used as structural materials in marine and automotive industries; and their casting products could be found in dairy, food handling, and chemical processing applications [1]. Aluminum magnesium phase diagram is shown in Figure 2.1 below:

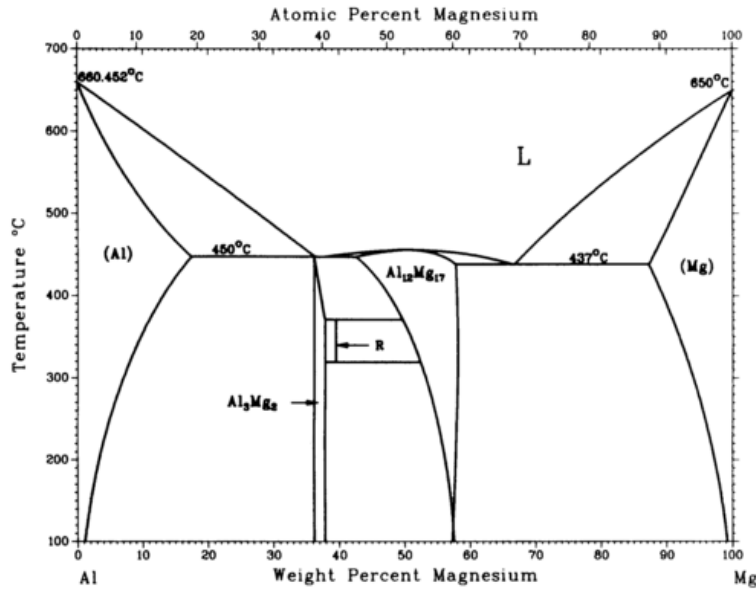


Figure 2.1: Al-Mg phase diagram [19]

Showing on the left corner of the phase diagram, Al α phase is a face-centered cubic Al solid solution. The maximum solubility of Mg in Al α phase is 17.1wt% at a eutectic temperature of 450 °C. The eutectic composition is reported to be 37wt% [20]. The β phase presented is a face-centered Al₃Mg₂; however, the difficulty in nucleating the β precipitates makes the 5000 series non-heat-treatable in general [18]. For casting Al-Mg alloys with a high Mg content (over at least 5wt%), age hardening can be achieved if the right heat treatment was to be applied [21].

2.2. Strengthening of Al-Mg alloys

The as-casted Al-Mg alloys are strengthened mainly by two mechanisms: solid-solution strengthening and cold working.

Solid-Solution Strengthening

Solid solution strengthening of Mg in Al-Mg alloys could be explained by Suzuki locking. Mg solute atoms tend to segregate around the dislocations and the stacking faults between dislocations. By doing so, the overall energy of the system is reduced. As a result, more energy will be needed to move these dislocations.

The increase in Vickers hardness ΔH_v can be expressed as a function of the solute fraction f_s , the solute and aluminum atom radius r_s and r_{Al} as follow [22]:

$$\Delta H_v = K \left(\left| \frac{r_s - r_{Al}}{r_{Al}} \right| f_s \right)^{1.33} \quad \text{Eq. 2.1}$$

Figure 2.2 shows that among all the elements, Mg could provide the highest increase in yield strength per unit weight due to its low molar weight comparing to other alloying elements and high atom radius difference comparing with Al atoms [23].

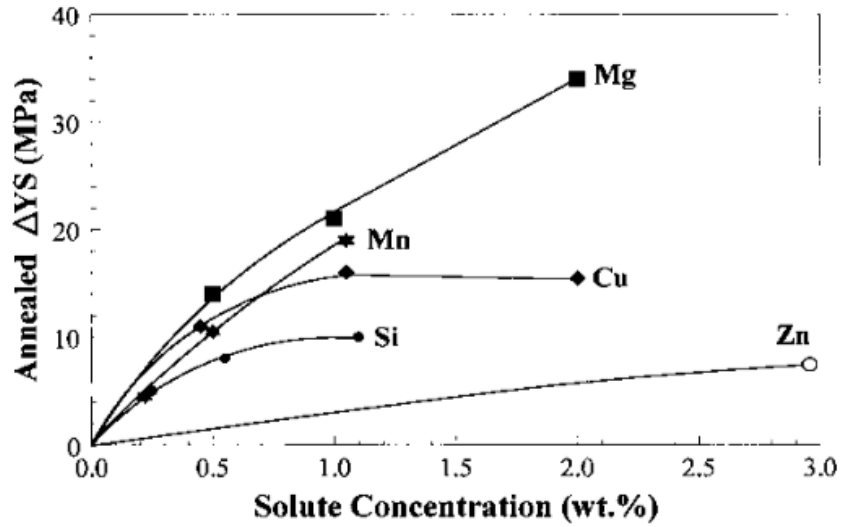


Figure 2.2: Solute concentration in percent weight to the increase in yield strength

The strength increase due to different Mg additions can be expressed in the function as follow:

$$\sigma_f = 15.5 (wt\%Mg) \quad 2.2$$

The coefficient 15.5 in the above equation could change by the difference in the size and texture of grains [23].

Cold Working

In cold working (or strain hardening), randomly distributed dislocations are created and existing dislocations are multiplied. Stress fields generated in this process help to obstacle the movement of dislocations. In Al-Mg alloys, Mg solute is found to promote the work hardening process by precipitating Al_2Mg_3 around the dislocations to block the dislocation movements, increasing the rate of dislocation multiplication to build up the dislocation

density, and reducing the rate of recovery to improve the efficiency of the work hardening process [23].

Figure 2.3 shows the difference in UTS with the addition of different solutes. Due to the elongations in different aluminum alloys are similar, their UTS would be a good indication of how effective each of the solute elements helps to work harden aluminum. Mg shows the second best UTS increase per atom percent.

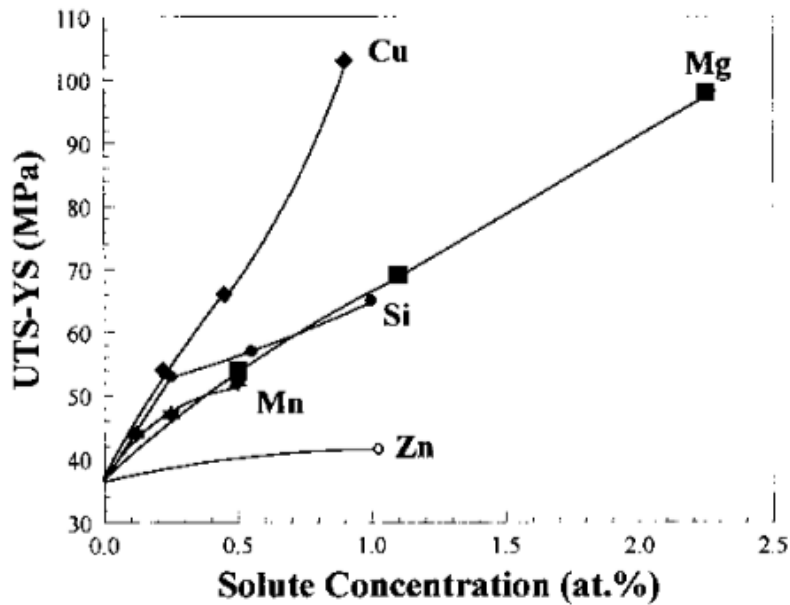


Figure 2.3: Alloying elements in atomic percent to tensile strength [23]

Figure 2.4 shows the increase in cold working of pure aluminum and different Mg addition levels during cold rolling. It suggests a higher Mg addition will lead to a better response to cold work, at least up to 4.5wt%.

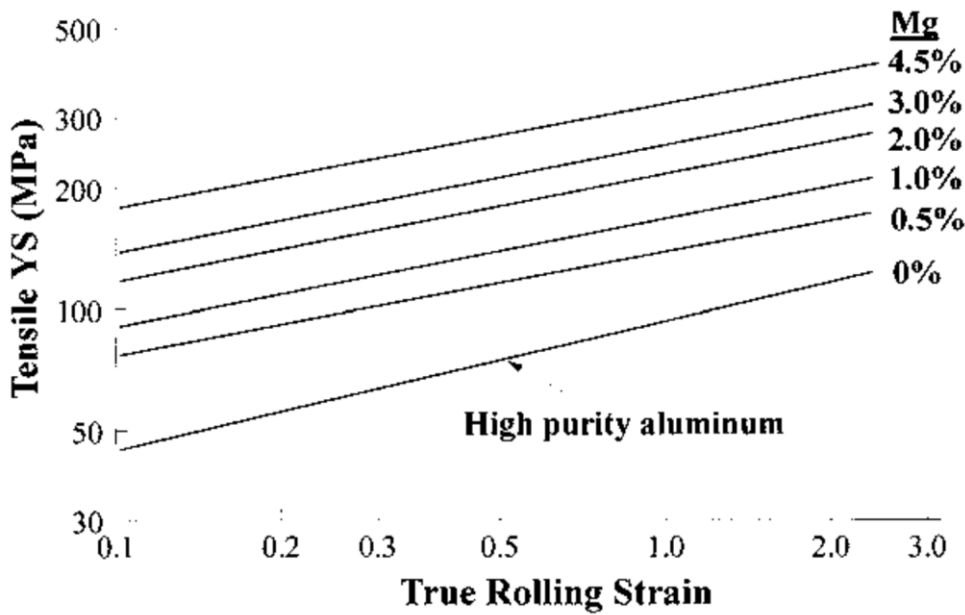


Figure 2.4: Rolling strain vs. tensile strength for pure aluminum and Al-Mg alloys during cold rolling [24]

Therefore, it can be summarized that more Mg addition is extremely useful for Al-Mg alloys to reach a better mechanical property. However, a high Mg content is also found to be responsible for some difficulties in processing as well as decreasing the resistance to stress corrosion cracking [2]. The effective weight percent of Mg for hardening was found to be less than 5wt [25].

Other potential strengthening methods for Al-Mg

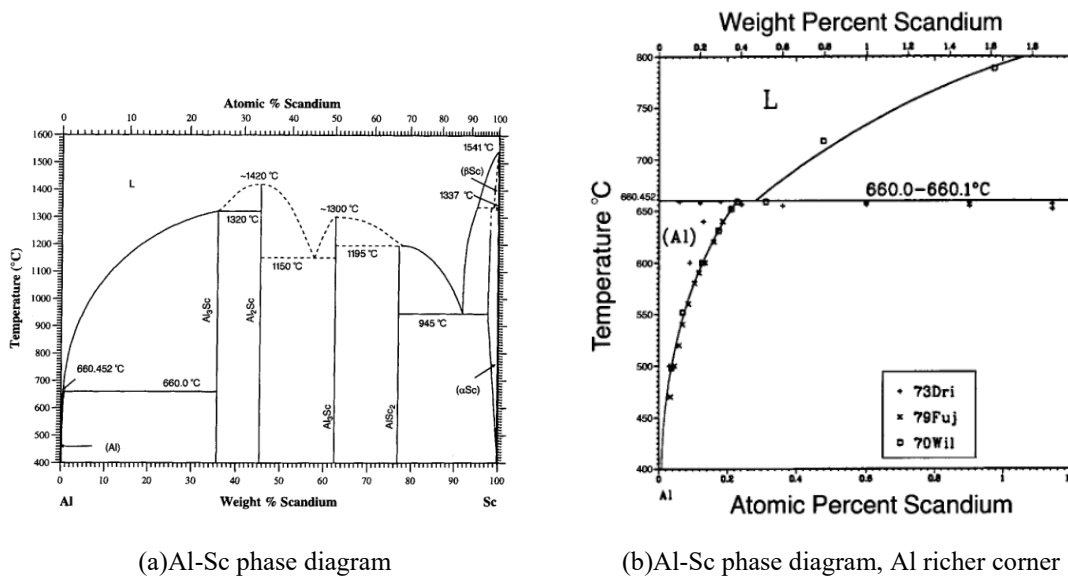
Grain size reduction could strengthen 5000 series O temper products (annealed after hot forming processes) by 7 – 28 MPa; but it does not have a tremendous impact on enhancing other Al-Mg alloy products [18]. Al-Mg is considered to be non-heat treatable. Binary Al-Mg alloys are reported to show an abnormally little response to aging, and precipitation hardening effect only observed until the Mg content exceeds 5wt% [23].

Another alternative strengthening method for Al-Mg alloys is through the addition of scandium into the alloying system. Among all the aluminum alloying elements and strengthening mechanisms, scandium is found to be the most effective strengthening addition per atomic percent [26]. For example, the casted Al6Mg0.17Sc alloy shows a significantly higher 0.2%-proof-stress (~55% higher), a higher tensile strength (~20%

higher), a higher microhardness (~30% higher) and a slightly lower ductility than the casted Al-Mg alloy [27].

2.3. Sc addition in Al and Al-Mg alloys

In 1971, L. A. Willey discovered Sc's effect of improving the strength of Al-Mg alloys for the first time [28]. The Al-Sc phase diagram is shown in Figure 2.5. The maximum Sc solubility in aluminum achieved at a eutectic temperature of 655 °C for solid and liquid aluminum are 0.38 wt% and 0.52wt%, respectively.



(a) Al-Sc phase diagram (b) Al-Sc phase diagram, Al richer corner
 Figure 2.5: (a) Al-Sc phase diagrams; (b) Al corner in Al-Sc phase diagram [29]

Sc strengthens Al and Al-Mg alloys through age hardening process with the formation of the L12 β phase Al_3Sc . The Al_3Sc precipitate strengthens the material by its ability to block the dislocation movement [3]. Mg and Al_3Mg_2 β phase are nearly not soluble in Al_3Sc precipitates; hence the precipitation hardening effect of Sc addition becomes additive to the solid solution strengthening effect provided by Mg addition [30].

Another attribute for Al_3Sc precipitates is its ability to stabilize fine grains preventing them from grain growth. This refinement effect allows more work hardening to be done to the alloy for extra strength and toughness [30]. The stabilizing effect of Al_3Sc will also minimize the loss of strength for Al-Mg alloys during toughness recovery processes. With the Sc addition, the recrystallization temperature of Al-Mg-Sc alloys increases to above

600 °C due to the stabilization effect of Al₃Sc, higher than those heat-treatable aluminum alloys. This makes Al-Mg-Sc alloys heat-treatable [31].

During age hardening process, Al₃Sc nucleates into clusters that grow to larger particles and then start to coarsen. According to bowing and cutting mechanism, small particles intercept dislocation movement effectively by cutting while the dislocations bow around coarsened particles with less obstacles. Therefore, during aging, it would be optimum for the particles to grow without coarsening. However, for Al₃Sc, it is found that the growth and coarsening of Al₃Sc precipitates take place simultaneously. The coarsening stage is transformed from the mixed stage of both growth and coarsening when the growth rate is reduced. The hardness for the alloys starts to decline at the mixed stage [32]; and therefore, a relatively low aging temperature and a small amount of Sc addition would be a good combination of achieving decent age hardening effect. On the bright side, Al₃Sc has similar lattice parameters as the Al matrix, and thus, its precipitates coarsening rate is reduced compared to other precipitates [33].

The age hardening temperature is suggested to be 300 °C based on previous researchers. Coherent Al₃Sc precipitates were observed from solution-treated alloys at 300 °C in alloys with 0.0006 wt% Sc and 0.03 wt% Sc [31], and the peak hardness for Al3Mg0.15Sc as-cast sample occurred at 300 °C for 8.33 hrs [34].

Precipitation Strengthening

The precipitation hardening effect of Sc follows the Orowan Strengthening mechanism. During aging, the supersaturated Sc in the alpha aluminum matrix precipitates out to form Al₃Sc precipitates. Depending on their size, the precipitates are either sheared or looped by dislocation during deformation.

For small particles, which are coherent or partially coherent with the aluminum matrix, shearing by dislocation will occur. The increment in yield strength due to the presence of these small precipitates can be expressed by the following equation [35]:

$$\Delta\sigma_y = cf^m r_p^q \quad 2.3$$

Where, c, m, and q are constants; f is the volume fraction of precipitates, and r_p is the radius of precipitates. In Equation 2.3, m and q are positive, and are reported to be around 0.5 in

most of the cases [35]. Hence, for precipitates that are sheared by moving dislocations, their fraction and size have a positive impact on the strength of the alloy.

As aging process continuous, the precipitates will grow and lose coherency. Instead of shearing, moving dislocations will loop around the precipitates, and this strengthening mechanism could be expressed as the following equation [35]:

$$\Delta\sigma_y = \beta r_p^{-1} f^{0.5} \quad 2.4$$

The volume fraction, f , is a positive factor contributing the increase of strength while the precipitate size is inversely proportional to the strengthening effect. Figure 2.6 summarizes the effect of precipitates size on the critical resolved shear stress (CRSS).

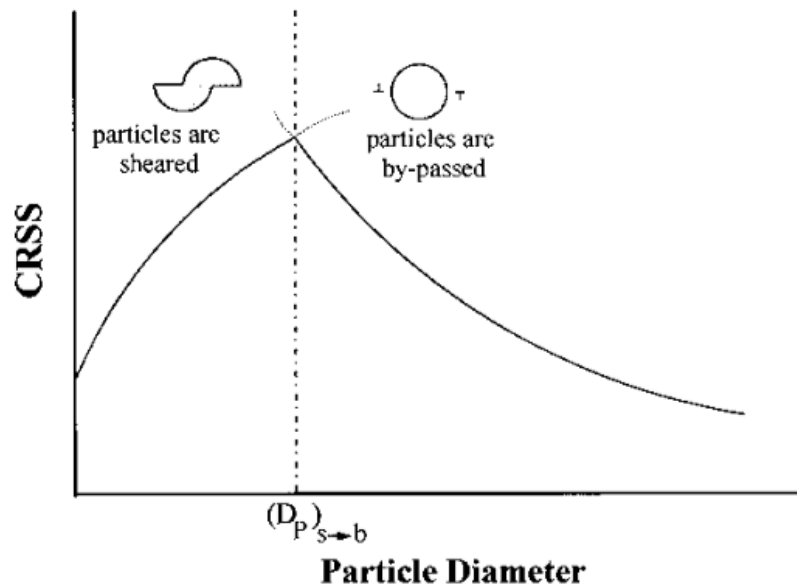


Figure 2.6: Precipitates size's effect on CRSS [23]

A critical size $(D_p)_{s \rightarrow b}$ is established representing the theoretical maximum of the CRSS could be achieved. This holds true for all the precipitation hardening phenomenon follow Orowan Strengthening mechanism. For Al_3Sc precipitates, this critical particle diameter is reported to be in the range of 2-3.7nm [4].

In addition to the volume fraction and the precipitate size, precipitates spacing and their shape can affect their strengthening performance as well. The precipitates are expected to be uniformly distributed so that their strengthening effect is uniform. If the distance

between each precipitate is too long, smaller dislocations will pass through them without any effective interaction; while on the other hand, if the precipitates are too close, the larger dislocations would bypass many precipitates leading to an inefficient use of these precipitates. Therefore, the precipitation hardening effect is maximized when the curvature radius of the moving dislocation equals to the spacing between the precipitates [23]. The shape of the precipitate varies with its misfit with the matrixes. Spherical particle tends to form at a small misfit. Since misfit reduces the ductility of the material and enhances precipitate coarsening rate during aging, a lower misfit between the precipitate and the matrix, and therefore a spherical shape of precipitates is preferred [36].

2.4. Casting of Al alloys

Aluminum is one of the newest metal to cast, as compared to copper, gold, tin, lead and silver, which were first to cast at least 10,000 years ago [37]. During casting, aluminum alloys go through melting, alloying, fluxing, degassing, melt refining, filtration, and solidification processes [38].

In fluxing, undesired particles in the melt will be separated and removed. Degassing is applied to reduce hydrogen dissolution in the alloy. This helps to avoid hydrogen induced cracking or internal porosities. Melt refining is done to eliminate impurities presented in the system to ensure the integrity of the cast product. During the filtration process, inclusions contained in the liquid alloy are captured by filters the melt is passed through [37]. After these steps, the alloy melt is sent to solidify into the desired form.

Among all the casting processes, solidification is the most critical step as it determines the microstructure and therefore the properties of the final product. The microstructural features in consideration are dendritic arm spacing, grain structure and the formation of eutectic and intermetallic phases. The spacing between the secondary dendritic arms (SDAS), for a given composition, is solely controlled by the solidification rate; both mechanical and physical properties increase as the SDAS is reduced. As for the grain structure, an equiaxed grain is reported to offer a better resistance to hot tearing, a better surface finish, a less microsegregation, and a more homogenized grain compared to a columnar grain. Equiaxed grains can be achieved by a high cooling rate or by mechanical agitation [37]. A high solidification rate is also suggested to reduce the detrimental effects

of intermetallic phases. For instance, at a low cooling rate, the formation of needle shaped intermetallic phases β -Al₅FeSi is found to reduce the mechanical properties of the products in aluminum castings [39].

Some post-casting treatments are done to the material to achieve better material properties through strain hardening and/or heat treatment. For the conventional DC casting, the average cooling rate is about 1K/s. This gives time for the solute to precipitate and growth to occur during the casting process. To develop a supersaturation of the solute element in the as cast aluminum, solid solution heat treatment or solutionizing refers to the process where the alloys are held near yet below their eutectic temperature for a relatively long period and then quenched. The time for solutionizing varies from minutes to twenty plus hours based on the thickness of the products. When the material is heated up close to its eutectic temperature, many problems could occur. Incipient melting caused by localized solute concentration leads to non-visible defects that significantly reduce the mechanical properties of the alloy. High-temperature oxidization and surface blistering due to moisture could also occur [40]. If a higher cooling rate could be established through rapid solidification process during casting, the precipitation and growth of solute would not occur; and this solid solution step could then be avoided.

2.5. Rapid solidification

A process can be termed as a rapid solidification process if it can generate very high cooling rate in the system that solidifies the processed material with a significant deviation from equilibrium. The most commonly used definition of cooling rate is the averaged ratio of temperature and time, for material from the temperature where the solidification of primary phase begins to the temperature where the solidification of eutectic structure is complete. The ratio can be expressed as following,

$$\dot{T} = \frac{\Delta T}{t_f} \quad 2.5$$

Where \dot{T} represents the cooling rate; ΔT is the solidification range; and t_f is the overall solidification time [41].

Different solidification processes can be categorized based on the difference in their cooling rates. Table 2.1 shows such a categorization. Solidification processes with cooling rates ranging from 10^{-6} K/s to 10 K/s (Very low and low) can be referred as “normal solidification”. Medium-rapid to Ultra-rapid solidifications are considered to be rapid solidification processes. These processes happen when a system, which has one dimension being minuscule compared to the others, experiences a large heat sink [41].

Table 2.1. Classification of solidification based on cooling rates [41]

Cooling Rate (K/s)	Designation
$10^{-6} - 10^{-3}$	Very Low
$10^{-3} - 10$	Low
$10 - 10^3$	Medium-Rapid
$10^3 - 10^6$	Rapid
$10^6 - 10^9$ and above	Ultra-rapid

Figure 2.7 shows a plot of cooling rate vs. secondary dendrite arm spacing. The smaller the distance between the centers of two secondary dendrite arms implies a finer structure.

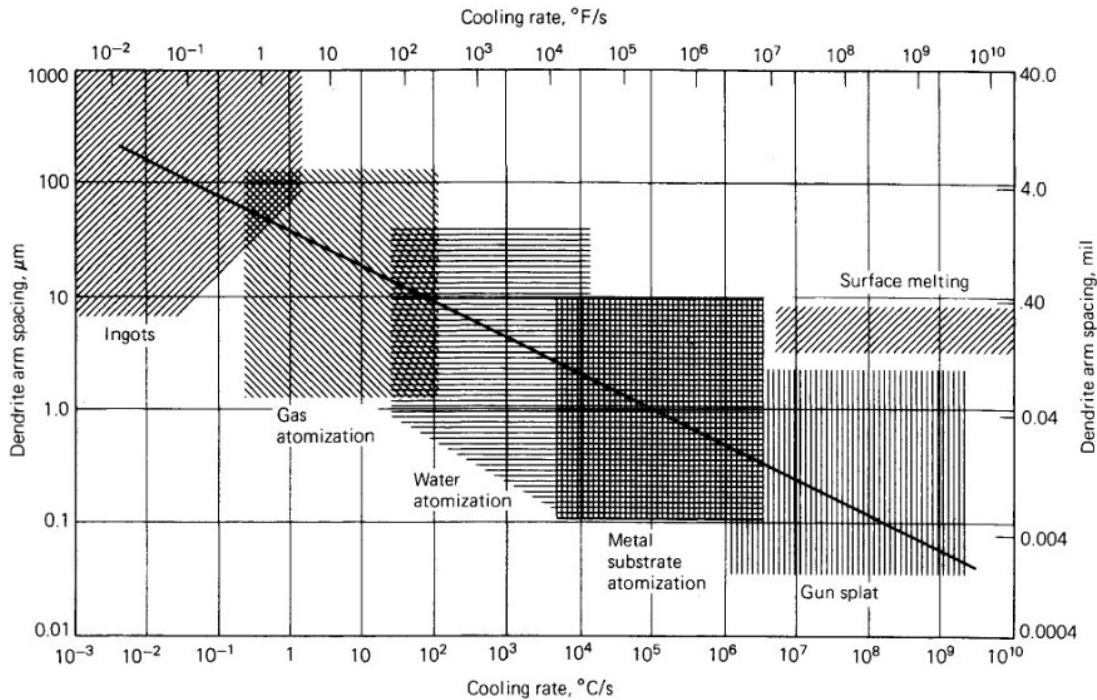


Figure 2.7. The change in scale of the structure as the cooling rates are increased [42]

The graph above suggests that a higher cooling rate can solely lead to the formation of a finer microstructure, without the help of inoculation or other methods that affect the integrity of the products. Hence, rapid solidification is known to generate finer structures with increased chemical homogeneity.

2.6. Impulse atomization

Impulse Atomization (IA) was developed and patented at the Advanced Material and Processing Laboratory, University of Alberta, Canada. IA is a single-fluid atomization process. Single-fluid atomization refers to a stream formed when exiting an orifice, then subsequently breaking down due to gravity or vibration instead of interaction with air, oil or other inert gas (two-fluid) [41].

Figure 2.8 shows a brief schematic of this process. An impulse generator is used to shake a plunger attached to it at a relatively low frequency and high amplitude. The plunger is positioned into the melt to be atomized. The melt in a tundish is accelerated by the movement of this shaking plunger and goes through a nozzle with a numbers of small orifices. The stream passes through the orifices, then breaks-up into spherical droplets with a controlled size distribution.

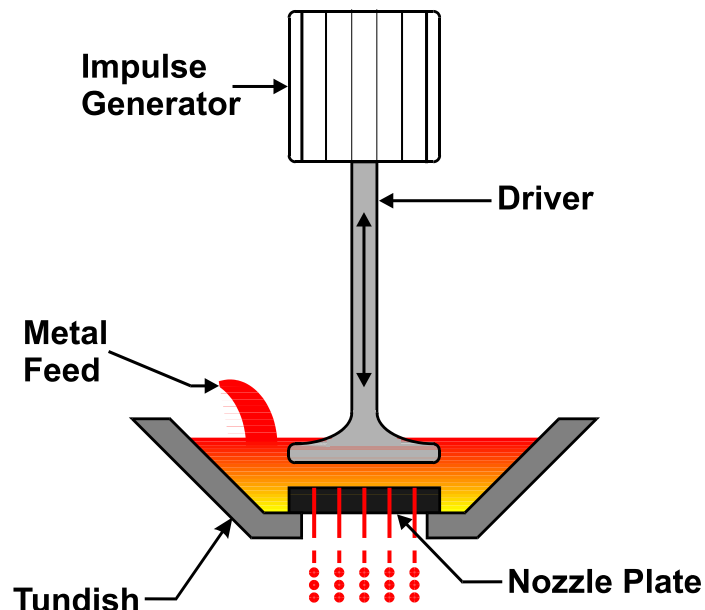


Figure 2.8. Schematic of impulse atomization process [12]

The droplets produced are solidified during their free fall while their heat is being extracted by the atomization fluid, usually an inert gas. The IA process can reproducibly yield powders of uniform size distribution with cooling rates as high as 10^4K/s [41].

Thermal Model

A mathematic model has been developed by Dr. J.B. Wiskel to describe the cooling profile of the droplets during an IA process [12]. The thermal model relates the distance of the droplets from the nozzle orifice to the temperature and solid fraction of the droplets.

Some assumptions are made in this model. The thermal model neglects the temperature gradient within the droplets since the droplet size is small and the Boit number is less than 0.1, where Boit number describes the heat transfer resistance ratio inside and at the surface of a body. The time for stream to break-up and for the spherodization of the ligament is also neglected since this time is short compared to the freezing range of the droplet [43]. The thermal model assumes the initial velocity of the stream from the orices to be 0.5 m/s, a constant ambient gas temperature, and no thermal interaction between droplets based on previous researches [44] [45]. The effect of undercooling is also neglected as the undercooling is found to have very limited effect on the soldification distance [44].

The first part of this thermal model is to define the temperature change through time, and it is expressed in equation 2.5 below:

$$\frac{dT_m}{dt} = -\frac{6h_{eff}}{\rho_m \cdot C_{p_m} \cdot D} (T_m - T_\infty) \quad 2.5$$

where $\frac{dT_m}{dt}$ is the change in droplet temperature with time, ρ_m and C_{p_m} are the droplet density and effective specific heat, respectively, D is the diameter of the droplet and T_∞ is the ambient gas temperature; and the effective heat transfer coefficient h_{eff} and effective heat capacity C_{p_m} are expressed in equations 2.6 and 2.7 below:

$$\frac{h_{eff}D}{k_s} = 2 \cdot \frac{B}{k_s \cdot (m+1)} \cdot \frac{(T_s^{m+1} - T_\infty^{m+1})}{(T_s - T_\infty)} + (0.4Re^{0.5} + 0.06Re^{2/3}) \cdot Pr^{0.4} \left(\frac{\mu_\infty}{\mu_s}\right)^{1/4} \quad 2.6$$

And

$$C_{p_m} = \frac{dH}{dT_m} = \frac{df_s}{dT_m} \cdot \Delta Latent + C_p \quad 2.7$$

where k_s is the gas conductivity at the droplet surface temperature, B and m are constants related to atomization gas, Re and Pr are the Reynolds and Prandtl numbers calculated at ambient temperature, $\frac{\mu_\infty}{\mu_s}$ is the ratio between the viscosity at ambient temperature and droplet surface temperature, f_s is the fraction solid at temperature T_m , $\Delta Latent$ is the latent heat of fusion, and C_p is the droplet heat capacity. The use of effective heat capacity takes the latent heat released during solidification into consideration.

The second part of this model is to predict the droplet velocity changing with time. Newton's Second Law of motion for a free falling body is used. After balancing all the forces on the droplets (gravity, gas buoyancy and drag), the following equation is established:

$$\frac{dv}{dt} \frac{(\rho_m - \rho_g)}{\rho_m} g - 0.75 \frac{\rho_g}{\rho_m} \frac{C_d}{D} v^2 \quad 2.8$$

Where ρ_m and ρ_g are the densities of the droplet and gas respectively, g is the gravitation acceleration, C_d is the drag coefficient which is calculated by $C_d = \frac{18.5}{Re^{0.6}}$, and v is the relative velocity of the droplet to the ambient gas. By integrating Equations 2.5 and 2.8 with the respect of time, the temperature and distance from the orifice of a droplet with certain size could be estimated as well as its fraction liquid or solid.

The equations above suggest that if all the rest conditions remain the same, the cooling rate should increase with the decrease in particle size and increase in gas thermal conductivity. Also, as stated in previous section, cell spacing reduces with increase cooling rates. Thus, for particles having the same composition, an increase in particle size will lead to a reduction in cell spacing. Figure 2.9 shows such a result for Al4.3Cu, Al4.5Cu, and Al17Cu atomized in nitrogen and helium [41].

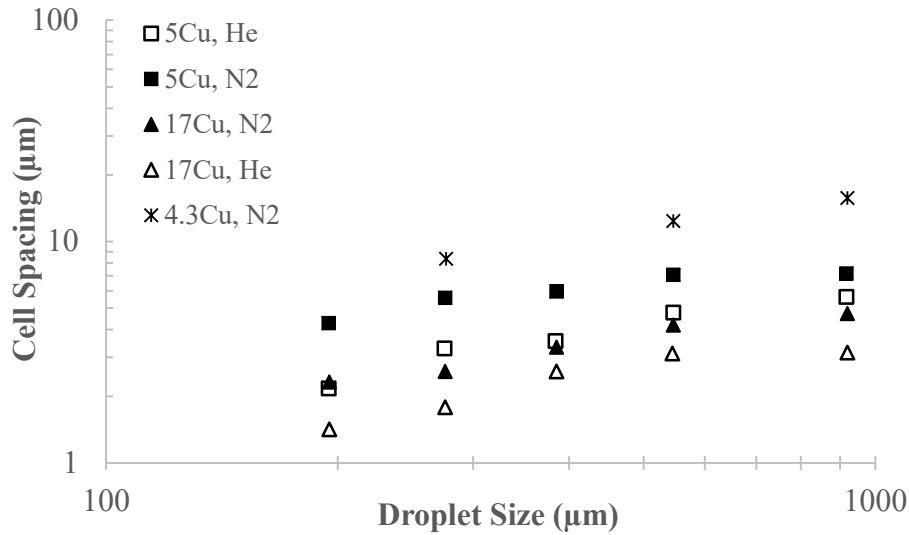


Figure 2.9. Cell spacing of Al-5%Cu and Al-17% Cu droplets atomized in N₂ and He.

2.7. Strip Casted Al-Mg-Sc Alloys

In industrial, one of the methods for achieving a rapid solidification process is twin-belt casting. The effects of 0.4wt%Sc in Al3Mg alloys produced by twin-belt casting was investigated previously [4]. A lab-scale twin-belt caster with a high cooling rate of 100K/s was used to produce strips of Al-3wt%Mg and Al3Mg0.4Sc alloys. Due to this high cooling rate compared to conventional direct chill casting (1-10K/s), a supersaturation of Sc in the aluminum alpha matrix was found [4].

To study the precipitation hardening of Sc, a part of the as-casted sample were heat treated at 300°C and 400°C from the 30s to 72hrs. To understand Sc's effect on obstacle grain growth, another set of as-cast sample underwent 80% cold rolling before they were annealed at the same condition. Vickers hardness measurements were performed on those samples. A summary of the result is shown in Figure 2.10.

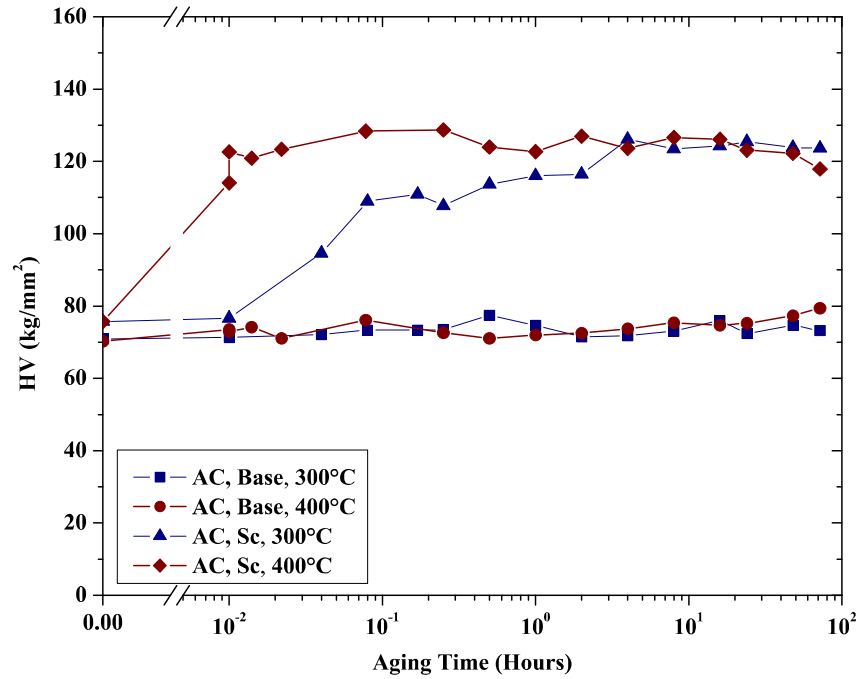
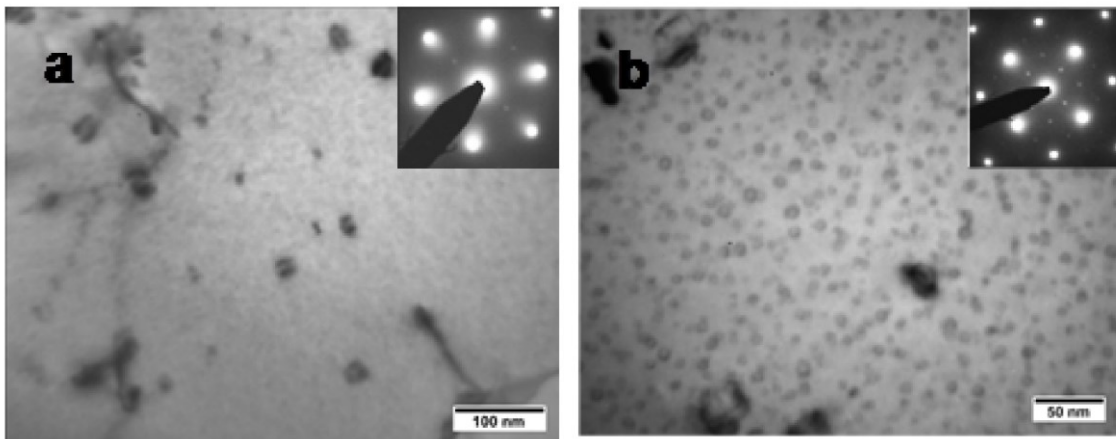


Figure 2.10: Vickers hardness for as-cast Al3Mg and Al3Mg0.4Sc at different temperature and holding different time period [4]

The presence of 0.4wt% Sc in the Al-3wt% alloys was found to increase the hardness after age hardening. Upon TEM examination, nano-sized coherence Al₃Sc precipitates were observed after aging that contributes to the age hardening effect. The TEM images are shown in Figure 2.11.



(a) As-Cast, age hardened at 300°C for 24hrs (b) As-Cast, age hardened 400°C for 15 min

Figure 2.11: Bright field TEM images; Al₃Sc precipitates during aging [4]

One of the future work proposed in this work is to perform similar microstructural, and mechanical property tests to Al-Mg alloys with lower Sc addition due to the high cost of Sc.

2.8. Summary

Aluminum being the most abundant element in the earth crust also shows a great combination of excellent strength and light weight. Among all the alloying elements, Mg has the best strengthening per weight percent ratio due to Mg's low density and outstanding solid solution hardening effect. However, excessive amount of Mg could not be added into aluminum without introducing concerns such as fragile to stress corrosion cracking. Sc could be added to further strengthen aluminum magnesium alloy. The strengthening mechanism for the Sc addition to aluminum alloy is precipitation hardening, which requires supersaturation of Sc. In order to achieve a supersaturation of Sc, solutionizing and quenching have to be done to casting products whose cooling rate is low. However, these processing methods are not cost or time efficient and many problems could occur during the treatments, such as oxidization and surface blistering. To avoid these additional heat treatment steps, a rapid solidification process could be used to produce Al-Mg-Sc alloys with the supersaturation of Sc as-casted, such as IA, IASD or twin belt strip casting. Al₃Mg with 0.4Sc produced by twin-belt casting shows a great increase in microhardness after aging compared to Al₃Mg without Sc addition. It has been proposed that the Sc addition could be reduced by at least 20wt% but still maintain a good precipitation hardening effect.

Thus, this work aims to determine the effect of strengthening on an Al-Mg alloy with 0.2wt%Sc undergoing rapid solidification. A breakdown of the approach used in this work to carry out this objective is outlined as follows:

2.9. Objectives

- Rapidly solidified Al_{1.5}Mg_{0.2}Sc and Al₃Mg_{0.2}Sc alloys will be produced with IA and IASD trying to cover the cooling rate range of twin belt strip casting;
- The cooling rate of IA powders will be simulated with the use of a thermal model that has been developed and verified in previous research [12] [13];

- A temperature measurement system will be developed, by which the cooling rate of the IASD process could be measured;
- Cell spacing measurement will be carried out on the powders and strips; and a correlation between the cooling rate and cell spacing will be established and compared with published work;
- Aging will be performed on the powders and strips performed at 300°C for varies period;
- Microhardness will be measured on as-produced and after aged powders and strips; a comparison will be drawn to see the precipitation hardening effect;
- DSC will be done to simulate the age hardening process to see if this hardening effect is due to the addition of Sc ;
- A comparison between cooling rate, cell spacing, and response to aging will be drawn between impulse atomized powders, spray deposited strip and twin belt casted strips to see if these the two processing method used in this work could be used to evaluate the performance of an new alloy in twin belt casting process.

3. Experiments and Results

In this chapter, the IA and IASD procedures will be introduced along with a list of the sample produced. The development of a temperature monitoring setup for IASD process is presented. Sieve analysis for IA powders will be shown. Different etchants and etching time to reveal the microstructure will be described. Inductively coupled plasma (ICP) of the chemical analysis of atomized powders and strips will be presented. Cell spacing measurement and microhardness measurement performed in this work will be introduced. Finally, furnace aging and DSC aging will be exhibited.

3.1. Sample production

3.1.1. Impulse Atomization

The schematic of the IA apparatus at the Advanced Materials and Processing Laboratory (AMPL) is shown in Figure 3.1.

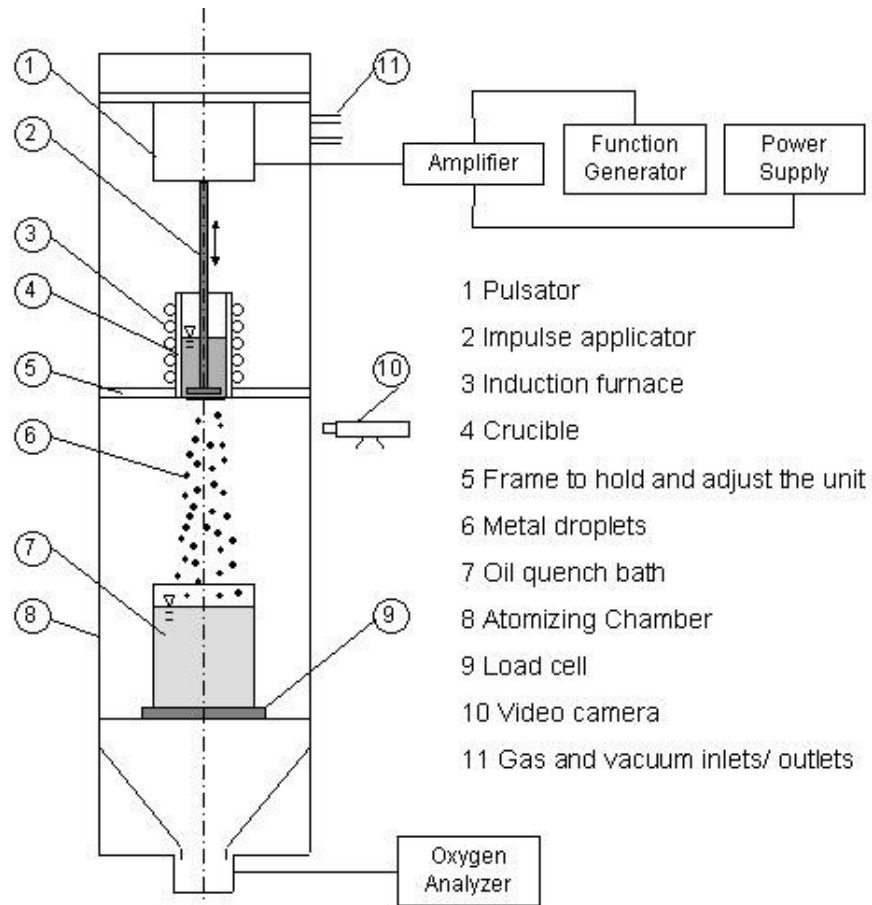


Figure 3.1: Schematic of the AMPL IA tower [10]

For all the IA runs performed in this study, 3mm thick graphite nozzle plates with 37 orifices (350 μm in diameter) were used along with graphite crucibles (4 in the schematic). Graphite was chosen for the nozzle plates and crucibles materials due to its excellent thermal and electrical conductivities for better heating efficiency using an induction furnace (3 in the schematic). The nozzle plates were glued to the bottom of the graphite crucibles with a graphite glue.

During the setup, an alumina plunger (2 in the schematic) was fixed onto the pulsator (1 in the schematic) with bearings. The plunger was set above the nozzle plate at a distance equals to the shaking displacement. A pre-calibrated Fisher brand K-type thermocouple was inserted into the crucible. A ceramic tube was used to protect the thermocouple from the melt. The covered K-type thermocouple was placed way from the plunger to avoid any blockage to plunger movement. The metal charge of known weight was added into the crucible. A glass beaker (8 in the schematic) filled with oil was put on top of a load cell (7 in the schematic) located in the bottom chamber.

The IA could be considered as a three stages process: the atmosphere setting stage, the temperature setting stage, and the atomization stage. At the atmosphere setting stage, an Ar (or other gas as desired) atmosphere with less than 10 ppm oxygen level was established with vacuuming and purging. This is done because aluminum is very sensitive to oxidization. A slight positive pressure was maintained throughout the atomization process to keep the atmosphere in the atomization chamber at low oxygen level. At the temperature setting stage, the metal charge was slowly heated up to the desired atomization temperature and then stabilized for at least half an hour. At the atomization stage, the plunger was shaken at a proper frequency and amplitude so that a continuous stream of powders could be generated through the orifices. The atomized powders were collected in the beaker filled with oil 4m below the nozzle plate. The mass flow rate was recorded with the load cell.

3.1.2. Impulse Atomization with Spray Deposition

In an IASD process, instead of collecting the fully solidified powders in a beaker, semi-solid droplets were deposited onto a moving substrate to form a strip, mimicking the strip casting process. The schematic of the IASD set-up is shown in Figure 3.2:

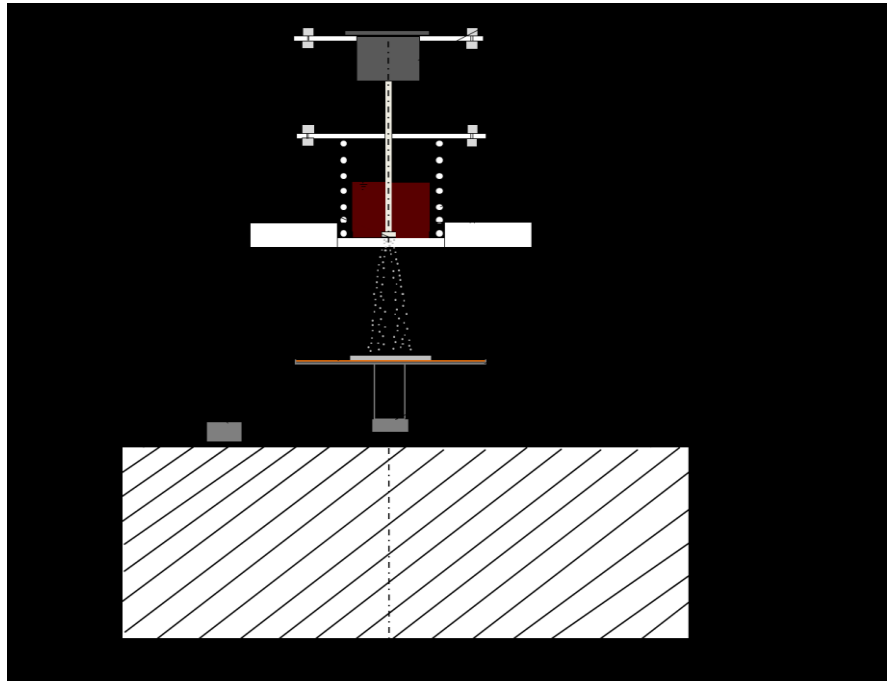


Figure 3.2: Schematic of the IASP set-up [10]

The top part of the IASD setup was the same as the top chamber of the IA tower described in the previous section. In the bottom chamber, or a turret in this case (6 in the schematic), a moving copper substrate (8 and 9 in the schematic) was put at 378mm (or other distances desired) below the nozzle plate. The copper substrate was clamped on the top of a substrate support, which was motorized to move horizontally at a speed of 5mm/s (or other speed of choice). The top surface of the copper substrate was sandblasted and sprayed with a thin layer of oil to achieve a better thermal contact between the copper substrate and the strip. The copper substrate was preheated to above 100°C by two heating blocks located on the substrate support. This was done to evaporate any moist on the substrate.

The IASD process could be considered as an IA process with an additional deposition stage, at which semi-solidified droplets continuously deposited on the moving copper substrate.

3.1.3. Sample Produced

Figure 3.3 shows the powder and strip samples produced from IA and IASD processes.

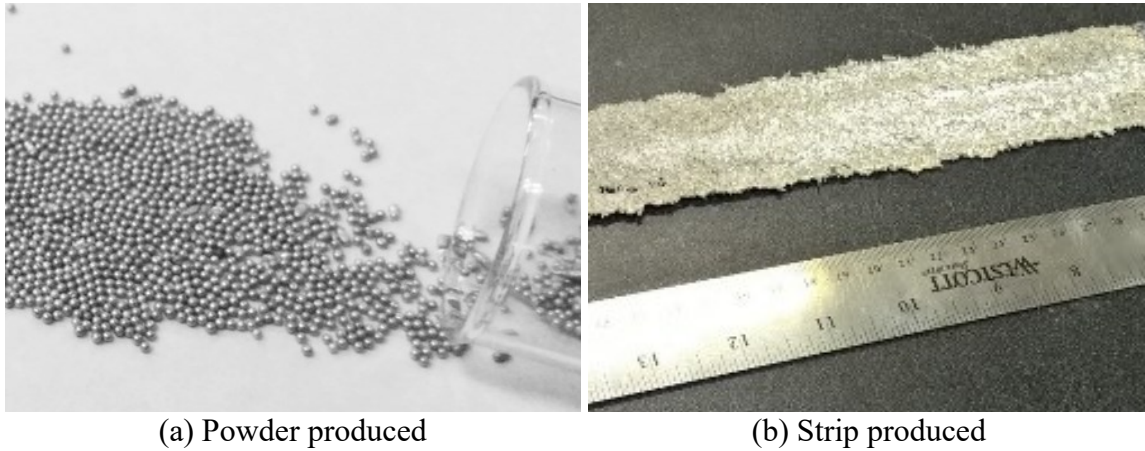


Figure 3.3: Sample produced from (a)IA and (b) IASD

A summary of IA and IASD runs performed in this work is shown in Table 3.1.

Table 3.1: Runs done in this study

Run #	Composition	Size	T _{initial} (°C)	Comments
IA1	Al1.5Mg0.2Sc	350 μm	900	Produced powders with different size ranges
IA2	Al3Mg0.2Sc	350 μm	900	
SD1	Sn	250 μm	400	Test run
SD2	Al1.5Mg0.2Sc	350 μm	1000	Cell spacing, eutectic fraction, micro hardness, age hardening at varies time @300 °C and its effect after aging were to be measured
SD3	Al1.5Mg0.2Sc	350 μm	900	
SD4	Al1.5Mg0.2Sc	350 μm	800	
SD5	Al3Mg0.2Sc	350 μm	1000	
SD6	Al3Mg0.2Sc	350 μm	900	
SD7	Al3Mg0.2Sc	350 μm	800	
SD8	Al4.5Cu	350 μm	800	
SD9	Al3Mg0.2Sc	350 μm	1000	

3.2. Temperature Measurement

In this study, a temperature monitoring system was developed to measure the top and bottom interface temperature of the strips. The top interface refers to the boundary between the top surface of the strip and the inert atmospheres; and the bottom interface means the boundary between the bottom surface of the strip and the copper substrate. A schematic of the temperature measurement setup is shown in Figure 3.4:

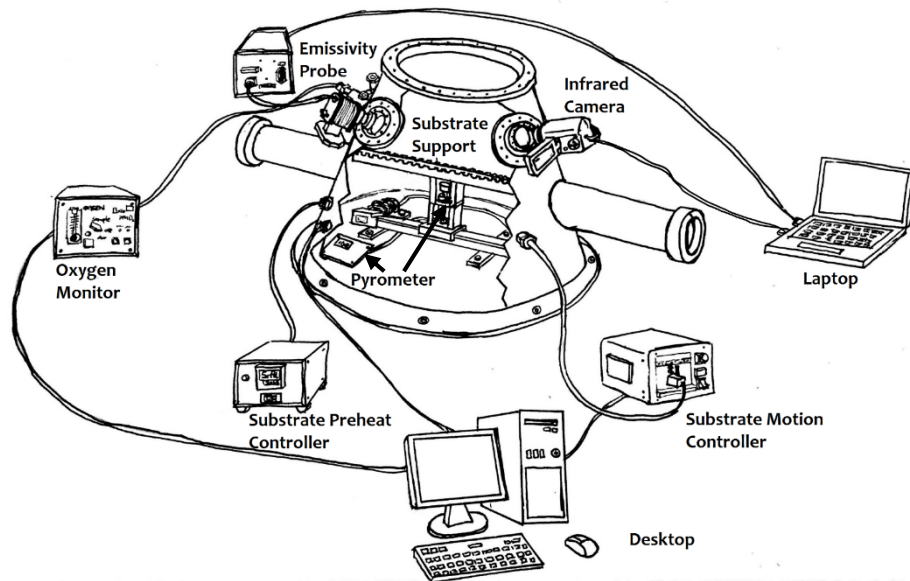


Figure 3.4: The schematic of temperature measuring setup

Infrared camera and emissivity probe

Mikron M7640 Infrared Camera and Mikron QL3600C-2B Infrared Quantum II Emissivity Probe were used in this work to measure the top interface temperature. They had shown their capability in measuring the top interface temperature in similar applications of other researches [46] [47].

An infrared camera measures the surface temperature of an object by converting the radiation emitted by that object. However, an object also reflects radiations from other objects at the same time. The emissivity is required to eliminate the reflection radiation for accurate infrared temperature measurement. In this work, Mikron QL3600C-2B Infrared Quantum II Emissivity Probe was used to measure the emissivity of the top surface of the strip. Figure 3.5 shows the block diagram of this device.

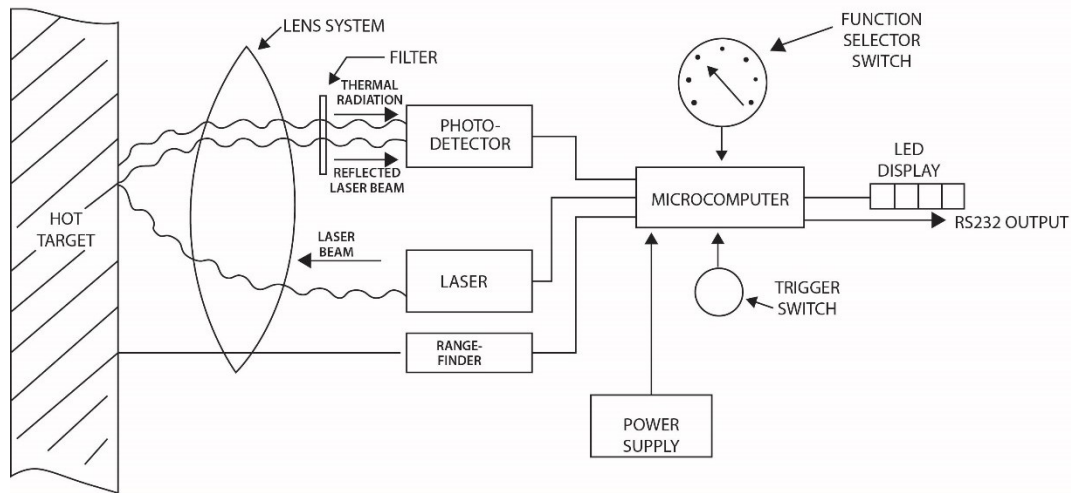


Figure 3.5: Simplified block diagram of the emissivity probe [48]

During measuring, a modulated infrared laser beam is sent to the target. The photodetector detects the intensity of the modulated infrared laser from the object. For an opaque object,

$$Emissivity = 1 - \%Reflected \quad 3.1 [48]$$

Since the infrared beam is modulated, a reflected beam from the object at the same wavelength could be distinguished by this device. The intensity of the infrared radiation decays with their travel distance. The “range-finder” in the emissivity probe helps to determine the distance between the device and the object in focus. When the %Reflected of the modulated beam is determined, the emissivity of the object can then be calculated by the microcomputer built-in the device based on the aforementioned equation. A temperature output could also be generated based on the radiation energy from the object at the same time.

The two observation windows on the previous IASD turret were modified to be the measuring windows for these two infrared devices. There are two issues that need to be addressed in order to do that: the position of the window and the property of the glass. The emissivity of an object depends mainly on two factors: the temperature of the object and the measuring angle (the angle between the sight of the infrared camera or the emissivity probe and the normal line from the measuring surface) if it is greater than 40° [49]. It is important to make sure that both of the devices are measuring the objects at the same sight

intersection point from the same angle. A schematic of the measuring position is shown in Figure 3.6.

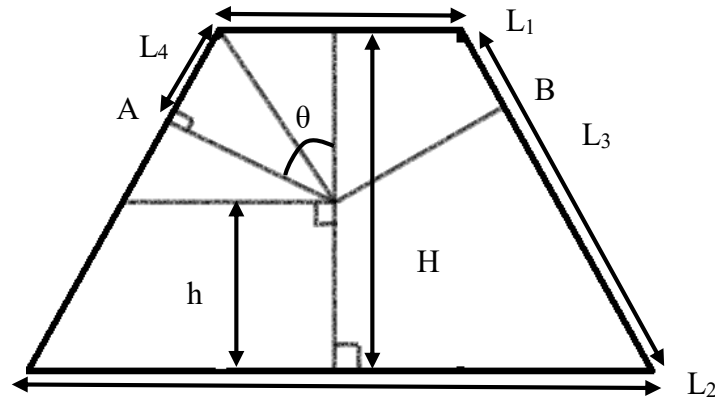


Figure 3.6: Schematic of measuring position

Points A and B show the location of the two observation windows. The height H of the turret is measured to be 51.5 cm. The upper diameter L_1 and lower diameter L_2 of the turret are measured to be 46 cm and 122 cm respectively. The turret wall length L_3 is measured to be 64 cm. The distance between the center of the observation window and the top edge of the turret along the turret wall L_4 is measured to be 14 cm. The measuring angle θ and the height of the devices measuring sight intersection point h are calculated to be 53.6° and 17.2 cm. The detailed calculations could be seen in Appendix A.

It is found that θ is larger than 40° and therefore, the emissivity probe has to be put at the same measuring angle as the infrared camera to get the specific effective surface emissivity at this angle. The height h is similar to the height of the substrate support, which is measured to be 18.5 cm. Therefore, it should be safe to say that the positions of those two observation windows were will intersect at the same point on the surface of the deposit. The intersection point is right next to where the spray of droplets occurs.

The infrared camera measures the radiation energy at a spectral band of 8-12 μm ; the emissivity probe shoots out a laser at the wavelength of 1.55 μm and the measures the intensity difference between its projection laser and laser reflected from the object surface. Therefore, the each of windows that those two devices measuring through need to have a minimal and known absorption loss at 8-12 μm and 1.55 μm respectively.

A 75mm in diameter Germanium with 3-12 μm AR coating IR window from Edmund Optics was used with the infrared camera. It has an above 95% transmission rate for light at a wavelength between 3 to 12 μm . A 75 mm in diameter Calcium Fluoride uncoated IR window from Edmund Optics was selected for the emissivity probe. It has an above 90% transmission rate for light at a wavelength of 1.0 to 2.0 μm . Their transmission rate vs. wavelength plot could be seen in Figure 3.7. According to the supplier, both of these two IR windows could take up to 69 kPa pressure difference as well as a slightly elevated temperature (40 $^{\circ}\text{C}$). In our case, the maximum pressure difference in IASD tower should be 34 kPa.

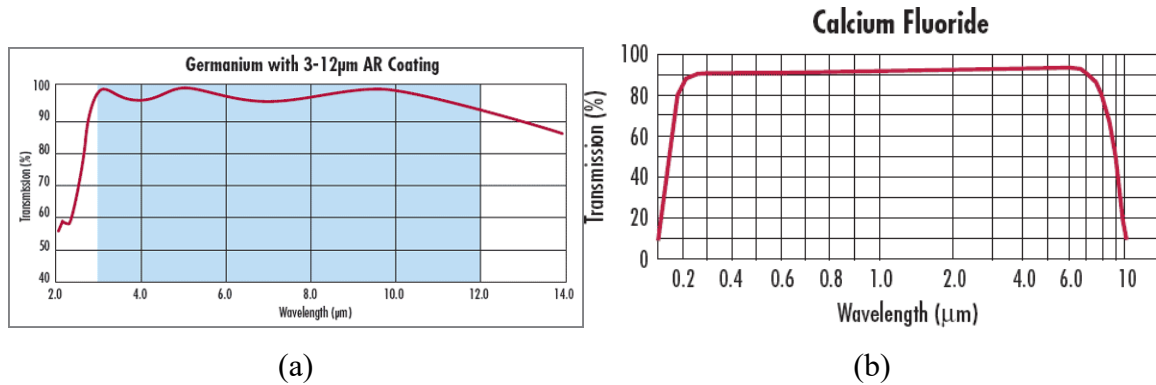


Figure 3.7: Transmission rate vs. Wavelength (μm) for (a) Germanium IR window with 3-12 μm AR coating and (b) Uncoated Calcium Fluoride window [50, 51]

2-color pyrometer

The bottom interface temperature is the temperature between the copper substrate and the bottom surface of the strip. A non-contact temperature measurement method has to be developed to avoid any additional heat sinks that could interference with the original condition.

An approach was proposed by the researcher previously worked on this project. It is to use three self-assembled InGaAs photodiodes to measure the radiation emitted by the strip through three small holes (0.5 mm in diameter), and then, converting the detected radiation energy into temperature reading through calibrating the energy signal against known temperature. However, this idea did not work because the measuring spot size for the photodiode was unknown but surely large enough to not be able to read through the 0.5mm

holes. Although this method was not feasible, it provides some insights into the final solution.

As mentioned above, the conversion of the radiation energy to temperature is related to the emissivity of the objects. Apart from measuring angle, the emissivity of an object is also temperature and surface roughness dependent [52] [53] [54].

The limiting factors of selection a proper temperature measuring tool for bottom interface temperatures are:

- Space: the measuring device has to be able to put underneath the substrate within the stage.
- The emissivity of aluminum: the emissivity of aluminum is relatively small. This means that the measured light contains lights that are reflected and refracted. Therefore drawing errors into the measurement.
- Non-contact: the intrusion of this temperature measurement has to be minimized to present the actual data.
- Small spot size: to prevent the deposit from dripping through the holes, the hole size is limited (<0.5 mm from experiment).

An infrared temperature measurement device is the major and relatively mature non-contact temperature measurement method available. There are two types of infrared device: single-color and two-color.

Single color devices detect light in a single wavelength. Emissivity value is required for a valid measurement. During the solidification process, due to the changing temperature and the phases, the emissivity keeps changing as well. A single-color pyrometer that is specified for aluminum measurement is also available. It focuses on a particular wavelength that corresponds to the smallest emissivity change for aluminum [55]; however, the smallest spot size for this device is above 1.1 mm. A general purpose single-color pyrometer will provide a smaller spot size (down to 0.45 mm at 88 mm distance) but an emissivity monitoring device will then be needed to measure the change in emissivity. Due to the space and temperature limitation, a fiber optic will then be required to be connected to the emissivity monitoring device. After checking with the supplier, there is no standard

fiber optical component available for our emissivity probe. So if this approach is used, a custom built connection is required. The lens from the emissivity probe has to be removed and connected to a fiber optic directly and then to the light sensor inside the emissivity probe. This could be done if the light sensor has a smaller surface area than the spot size; otherwise, the reading will not be accurate due to the fact that it will consider the light is coming from the whole area. Also, the optical fiber has to be aimed precisely at both ends, the sensor and the hole. Theoretically, this will work if the sensor has a smaller surface area than 0.5 mm but a lot of skill and work has to be put in, not accounting for the risk of reducing accuracy from any human errors. An alternative method should be considered.

A two-colored pyrometer measures simultaneously with two sensors in adjacent wavelengths. It calculates the temperature by rationing the radiation intensities of these two wavelengths. The absolute emissivity is not required. In addition, this technique eliminates some factors that reduce the accuracy of a conventional single color instrument, such as field of view, dirty viewing window, and dust or other contaminations.

A two-colored pyrometer with a temperature range of 350-1200 °C was identified [56]. It came with a fiber optic head. Figure 3.8 shows the schematic of this fiber optic head.

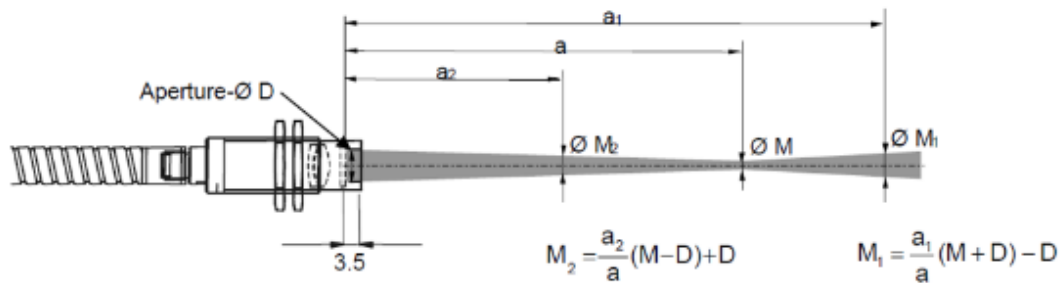


Figure 3.8: Schematic of the fiber optic head [56]

In the front of this fiber optic, there is a lens that is able to read a smallest spot size of 0.45mm at a focal distance of 87 mm. A laser targeting system is built inside the device allowing it to emit laser for easy targeting. This device could change from single color mode to two color mode if needed. The lens is enhanced so that it could be used at up to

250 °C. Considering the temperature of the copper substrate is less than 250 °C during the run, this protection is sufficient [57]. A built-in laser targeting light is provided to help the lens focus on the hole.

As stated above, the 0.45mm spot size could be achieved at a focal distance of 87mm. It is important to fix the lens at such distance from the top surface of the copper substrate (where metal/substrate interface occurs). First, a holder was implanted. A schematic is shown in Figure 3.9 (a). And Figure 3.9 (b) presents the actual setup. Two plastic screws were used to hold the fiber optic head. By loosening and tightening the screws, the height of the lens could be adjusted. The holder was attached to the center of the substrate support.

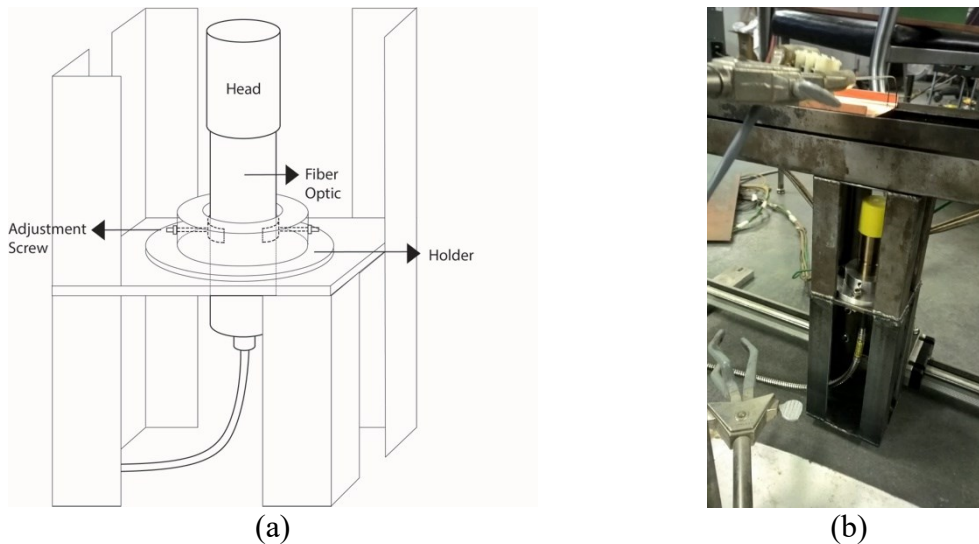


Figure 3.9: (a) Schematic drawing of the fiber optic lens; (b) fiber optic installed onto the substrate support with a holder

Calibration of devices

The infrared camera and the emissivity probe were calibrated together as they were to be used at the same time. The heat block used to preheat the substrate is used as a calibration heat source for the infrared camera and the emissivity probe. The temperature of the heating block was monitored by a K-type thermocouple. The temperature of the heat block was set to be 500 °C. The emissivity probe was used first without the installation of the IR window. At the same time, the infrared camera was also used to record the temperature of that block by setting the emissivity to 1.00. The point of interests was selected on the center of the view from the software. The infrared camera temperature was then calculated based on the

measured emissivity from emissivity probe. The experiment was carried out again through the IR windows. The result can be seen in the table below.

Table 3.2: Emissivity probe and infrared camera calibration data

Device	Emissivity Probe		Infrared Camera	
	Emissivity	T (°C)	T ($\epsilon=1$), °C	T (ϵ =measured), °C
Without IR window	0.896±0.018	503.3±4.2	566.8±5.8	508
With IR window	0.954±0.021	496.5±6.0	529.4±8.1	505

Less than 5% difference between the data recorded with and without IR windows was recorded. This suggests the selection of these IR windows is valid. The temperature recorded by the infrared camera after applying the measured emissivity was less than 5% lower than 500°C. Therefore, it is safe to say that both of the infrared camera and the emissivity probe are calibrated.

The effect of small holes on temperature readings was then studied. The experiment set-up is shown in Figure 3.10.



Figure 3.10: Calibration setup to test the effect of small holes

An iron wire was heated up by a power supply. The actual temperature of the iron wire was not monitored since it was the difference in temperature with and without the small holes that was interested at this stage. The goal here was to establish a comparison between the temperature measurements through different hole sizes and substrate thicknesses. The temperature calibration against an object with known temperature will be presented later. Two substrates (0.9 mm and 1.2 mm in thickness) with hole sizes of 0.45 mm, 0.55 mm,

and 0.65 mm were used. The wire was fixed by the clipper and held right on the top of the substrate. The substrate was then moved out of the view of the lens. The position of the wire was adjusted until there was a reading from the pyrometer. The substrate was moved back, and the focusing laser was turned on. The results are shown in Table 3.3.

Table 3.3: Temperature recorded against hole-size

	T for 0.9 mm thick substrate	T for 1.2 mm thickness substrate
Without Substrate	757.7 ± 4.0 °C	788.0 ± 4.6 °C
0.65 mm hole	726.7 ± 3.1 °C	757.7 ± 2.1 °C
0.55 mm hole	724.7 ± 2.5 °C	--
0.45 mm hole	--	--

Although the smallest spot size for the lens was specified at 0.45 mm, the smallest hole size that the pyrometer could read through was 0.55 mm, due to human error in alignment and setting the exact measuring distance. A 30 °C difference in the readings was noticed during the measurement. This could be explained by the small-hole effect, where the radiation intensity reduces approximately as the square of the ratio of hole diameter to length [58]. Due to the need of reading through small holes, a combination of 0.55mm hole and a 0.9 mm thick substrate was selected to be setup for temperature measurement.

The two-color pyrometer simultaneously measures the radiation intensities of two wavelengths with two sensors. The temperature is calculated based on the ratio of these two measured radiations and assuming the emissivity does not change with wavelength. By doing so, the effect of emissivity is minimized. However, for aluminum and most metals, their emissivity does change with wavelength. The two-color pyrometer selected has the ability to change the emissivity slope so that the actual temperature could be measured with higher accuracy. To find a correct emissivity slope, a comparison test with a thermocouple probe is suggested in the user manual [56]. Al3Mg0.2Sc sample cut from the strips were used as a test object. The setup of the calibration process is shown as follow:

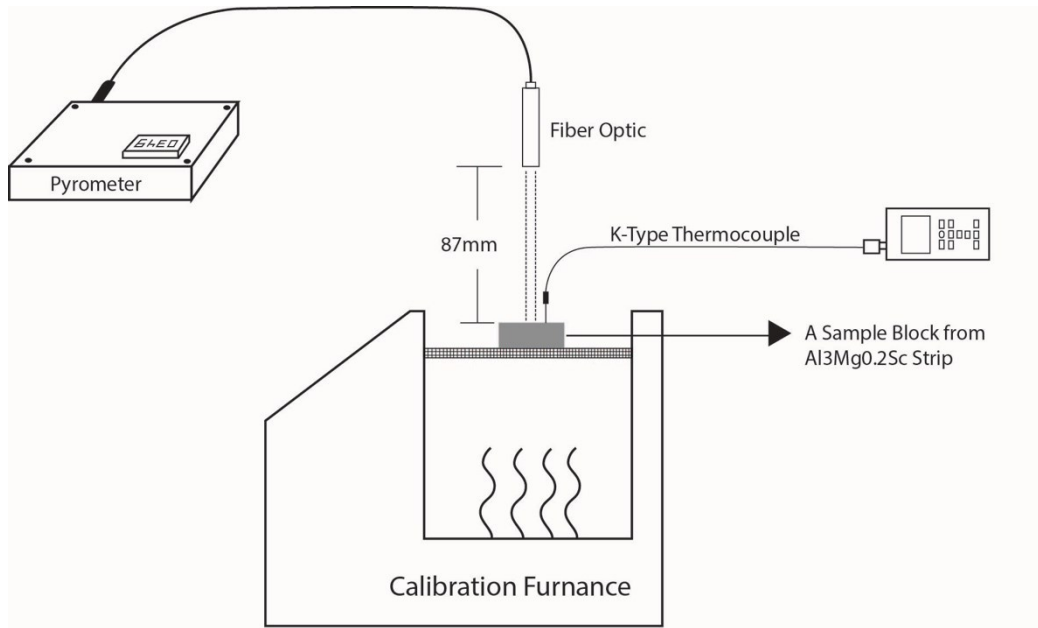


Figure 3.11: Schematic of the test for the effect of the emissivity slope

A small block of Al₃Mg_{0.2}Sc strip was put into a calibration furnace. The sample block was heated by the furnace while a calibrated K-type thermocouple was used to monitor the temperature on the block surface. The calibration profile of the K-type thermal couple could be found in Appendix B. The optic fiber lens was held at 87 mm from the top of the sample with a stand. The sample was first heated up to 400 °C. Emissivity ratio in the pyrometer was changed so that the temperature of the pyrometer is 400 °C plus 30 °C. The extra 30°C was added so that the temperature reduction due to the effect of measuring through a small hole could be compensated. The sample was then heated up to 500 °C and 600 °C. The temperature from the pyrometer is recorded (Table 3.4).

Table 3.4: Calibration data by changing the emissivity slope

Emissivity slope K	1.0	1.1	1.2
@400 °C	390.3± 2.5°C	414.7± 2.5°C	433.0± 2.0°C
@500 °C	486.7 ± 1.5° C	506.3± 3.8°C	526.3 ± 4.0° C
@600 °C	588.3± 1.5°C	614.3± 2.5°C	629.7 ± 4.2° C

The K value was set to be 1.2 where the extra 30°C reading met. With the increase of the temperature, there was some fluctuation in the temperature readings; however, this was still in the acceptable range of less than 5%. The calibration was performed up to 600°C.

3.3. Sample Analysis

3.3.1. Sieving

The collected powders were sieved using W.S. TYLER Sound Enclosure 6027 automatic sieving machine. ASTM B214 - 16 was followed. Sieve analysis was performed to find out the size distribution of the produced sample. Particles with size above 1000 μm were omitted from this analysis as they were not categorized as “powders” in this study and they represented a small portion of the total weight below 1000 μm . Table 3.5 shows the sieve data for Al3Mg0.2Sc_Ar.

Table 3.5: Sieve Data for Al3Mg0.2Sc_Ar

Avg. Size D (um)	Weight (g)	Weight Fraction	Wt% Cumla.	lnD	z
925	16.5	0.0771	100	6.83	3.34
780	31.7	0.148	92.3	6.66	1.42
655	49.0	0.229	77.5	6.48	0.753
550	38.3	0.179	54.6	6.31	0.115
462.5	26.5	0.123	36.7	6.14	-0.344
390	17.8	0.0832	24.3	5.97	-0.697
327.5	15.2	0.0711	15.9	5.79	-0.998
275	10.5	0.0491	8.84	5.62	-1.38
231	8.40	0.0393	3.93	5.44	-1.76
Total	213.9				

“Avg. Size D” is calculated by taking the average of the upper and lower sieves size. “Weight” is the weight of the sample in the corresponding size range. “Weight Fraction” is calculated by dividing the weight measured for each size range with the total weight. “Wt% Cumla” shows the cumulative weight percent at each size range. Cumulative weight fraction shows the weight fraction for powders of the size equal or smaller than the specified size range. “lnD” means the natural log of the specified average size. “Z” is the z-factor get from the z-table correspond to log-normal distribution [12]. “lnD” and “z” are plotted against each other. The plot is shown in Figure 3.12:

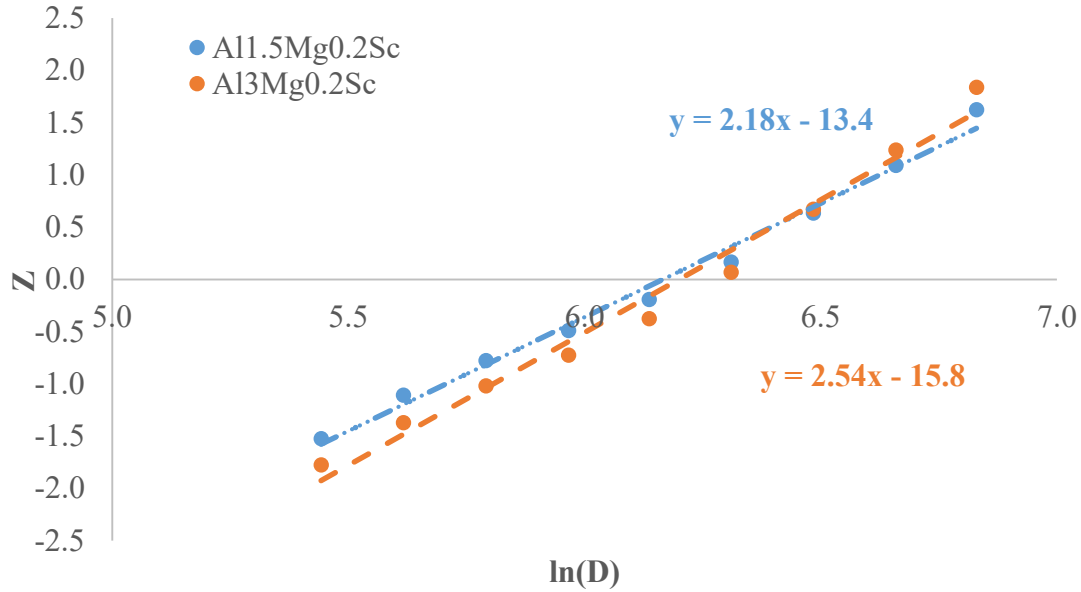


Figure 3.12: $\ln D$ vs. z -factor for Al1.5Mg0.2Sc and Al3Mg0.2Sc powders

A trend line and the corresponding equation are added to the plot. R^2 shows how well the powder size distribution to a log-normal one. “ $\ln D$ ” and “ z ” follows the equation 3.3.

$$z = \frac{1}{\ln \sigma_{gm}} \ln D - \frac{\ln D_{gm}}{\ln \sigma_{gm}} \quad 3.3$$

The results are tabulated in to Table 3.6.

Table 3.6: D_{50} and R^2 from sieve analysis

Run Label	Orifice Diameter	D_{50}	σ_{gm}	D_{50}/D_{Nozzle}
Al1.5Mg0.2Sc_Ar	350 μm	493 μm	1.48	1.41
Al3Mg0.2Sc_Ar	350 μm	477 μm	1.58	1.36

To sum up, the powders produced by IA have a log-normal distribution with a D_{50} being about 1.4 times the orifice size.

3.3.2. Metallography

Prior to microscopy and microhardness measurement, the powder and strip samples were mounted. For sample mounting, the epoxy is mixed and poured into a mold. The samples were put into a mold filled with epoxy. A small sheet of paper with the run number, composition and size range information was placed into the epoxy for reference purpose.

The samples were polished with Buehler’s AutoMet 250 auto polisher. The polishing procedure was based on the suggested polishing method provided by the manufacturer of aluminum alloys as shown in Table 3.7.

Table 3.7: Polishing procedure suggested by the manufacturer

Grade	RPM (head)	Load N (lb)	Direction	Time (min:sec)
320 grit	240	22.2 (5)	Com	Until plane
1200 grit	150	26.7 (6)	Com	6:00
3µm	140	26.7 (6)	Com	4:00
0.05 µm	120	26.7 (6)	Contra	10:00

To fully remove the adherence of the 0.05 liquid, the last step was repeated for another 1 minute with water instead of diamond liquid. The samples were then cleaned with tap water. After air drying, the samples were put into a glassware container filled with alcohol. The container was placed into an ultrasonic bath to wash for another 40 minutes.

Etching was performed on moulder powders and strips samples to reveal the grain boundaries. The procedure for sample metallography for aluminum magnesium alloys suggested in ASTM standard E407-07 “Standard Practice for Micro-etching Metals and Alloys” [59] are tabulated in Table 3.8 below.

Table 3.8: Suggested etchant and procedure

Etchant	Composition	Procedure
1a	0.5% HF	Swab with cotton for 15 s.
2	3 % HF	Swab 10 s to reveal general structure.
3	Keller’s	Immerse 10–30 s. Wash in a stream of warm water.
6	25% HNO ₃	Immerse 40 s at 70°C (160°F). Rinse in cold water
8a	10% H ₃ PO ₄	Immerse 1–3 min at 50°C (120°F).

Due to safety concerns and accessibility of the chemicals, etchant 1a and 3 were tested and used in this study. A 710-850µm diameter range Al3Mg0.2Sc powder sample was used as the etchant trial sample. The selection of larger particle size powders is due to their relatively large cell spacing suggested from the literature review.

Etching with 0.5% HF

Figure 3.13 shows an optical microprobe image taken after 0.5% HF was swabbed with medical use cotton Q-tip for 15 s. No observable structure was revealed after this etching. Several attempts were made for swabbing a longer time, but no change could be observed. The next tested etchant is Keller's solution

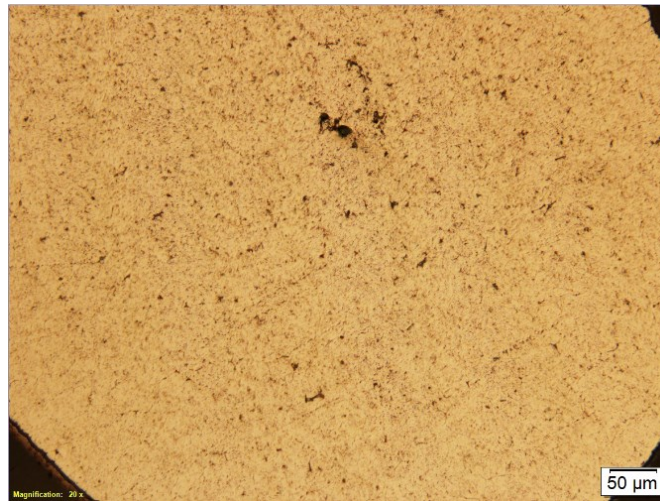


Figure 3.13: Al₃Mg_{0.2}Sc_Ar_600-710 etched with 1ml HF and 200 ml water and swabbed with cotton for 15 s

Etching with Keller's solution

Figure 3.14 shows Al₃Mg_{0.2}Sc_Ar_710-850 powder sample etched with Keller's etchant.

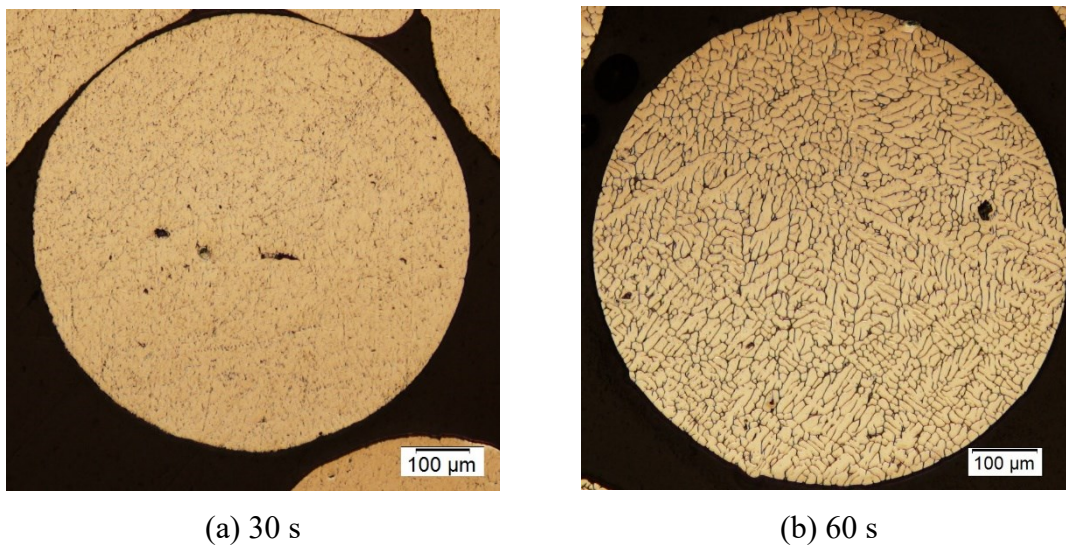


Figure 3.14: Al₃Mg_{0.2}Sc_710-850 powder etched by Keller's etchant for (a); (b)

The etchant was applied for 10 s, 20 s and 30 s; at the 30s, some faint grain boundaries was observed. But they were not bright enough for cell spacing measurements. The sample was etched for an additional 30 s; and as shown in (b), the dendritic structure was clearly revealed. Therefore, Keller’s etchant etching for 1 minute was selected to procedure for all the powder and strip samples in this study.

3.3.3. Inductively Coupled Plasma (ICP)

During atomization runs at temperatures higher than 800°C, Mg deposits were observed around the cooling tubes inside the tower. Samples of IA and SD samples were sent to Cambridge Materials Ltd for ICP analysis. The samples were reported to be digested with HCl, HF, and H₂O₂ solution. The ICP results could be seen in Table 3.9. The nominal Mg composition for the charge material was given by the supplier. The Mg content decreases with increasing atomization temperature. For the IA samples, the Mg concentration is closer to the charge metal than the SD samples. This could be explained by to the shorter holding time at the atomization temperature.

Table 3.9: ICP Result

Mg. Content	ICP	
Sample	Al1.5Mg0.2Sc	Al3Mg0.2Sc
Charge Material	1.53 wt%	3.12 wt%
SD_Ar_800C	1.40 wt%	2.98 wt%
SD_Ar_900C	1.38 wt%	2.91 wt%
SD_Ar_1000C	1.36 wt%	2.78 wt%
IA_Ar_900C	1.46 wt%	2.84 wt%

3.3.4. Cell spacing measurement

Optical Microscope

The washed and dried samples were examined under Olympus BX61 optical microscope. The optical microscope was connected to a computer and the software Olympus Stream was used to control the microscope. The eye lens was fixed at 10x. The observation lens was set to 20x to achieve an overall 200x magnification. A 500x magnification was also used in this study for finer structure. A sample image could be seen in Figure 3.15.

After polishing, the top and bottom surface of a mounted sample were not parallel to each other. Therefore, the top of the sample surface would not be parallel to the horizontal surface on which the sample was placed. This would lead to an image with a focus on one part and blur on the other part. The “Z-Stack” feature built in the microscope was used to acquire clear images. The “Z-Stack” feature enables us to combine images taken at different focal level and automatically produced an image with clear resolution.

Cell Spacing Measurement

Linear line intercept method introduced in ASTM E112-13 was employed in this study for cell spacing measurement. A sample measurement procedure is shown in Figure 3.15:

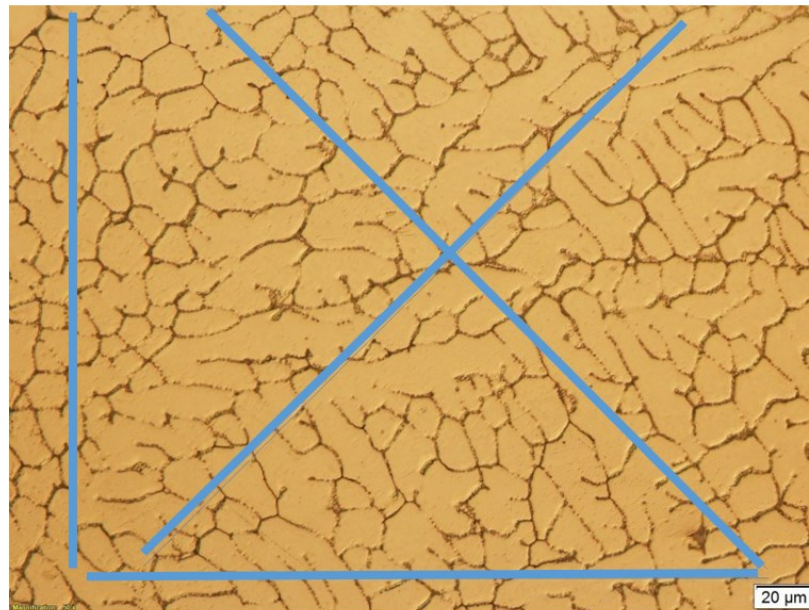


Figure 3.15: Cell spacing measurement procedure

Images acquired from the optical microscope was analyzed further using ImageJ. After setting the scale, four lines with known distances were drawn on the image. “Cell Counter” feature built-in the software was used to record times that the drawn line intersects with the cell boundaries. If a line is tangent to a grain or either end of the drawn line falls into the grain, a half intersection point was recorded. The final cell spacing would be the total length of the drawn lines divided by the number of interception points.

Powder

Figure 3.16 shows the cell spacing for Al1.5Mg0.2Sc and Al3Mg0.2Sc as a function of powder sizes.

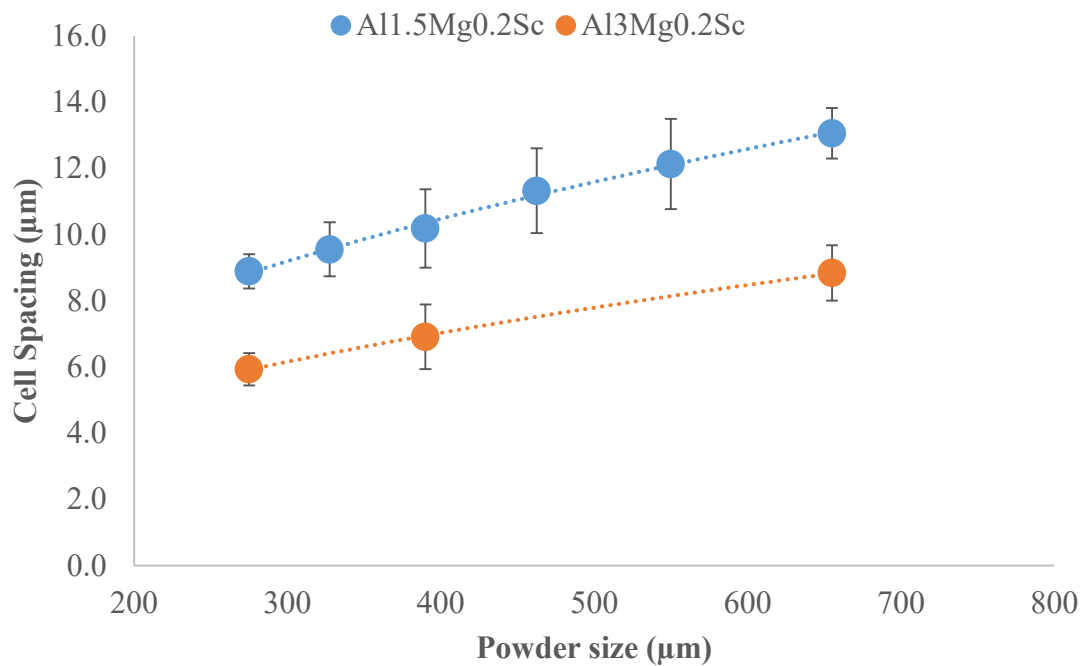


Figure 3.16: Cell spacing for Al1.5Mg0.2Sc and Al3Mg0.2Sc powders

The effect of cooling rate

One thing could be noticed from Figure 3.16 is that for powders of the same composition, cell spacing reduces with decreasing powder size.

Smaller powder size means the larger surface area to volume ratio. For powders produced by Impulse Atomization, their cooling rate $\frac{dT_m}{dt}$ could be expressed [12]:

$$\frac{dT_m}{dt} = -\frac{6h_{eff}}{\rho_m \cdot C_{pm} \cdot D} (T_m - T_\infty) \quad 3.2$$

Where h_{eff} is the effective heat convective coefficient, ρ_m and C_{pm} are the density and effective specific heat where latent heat was considered for the droplet; D is the droplet size; T_m and T_∞ are the temperatures for the droplet and tower atmosphere respectively. Equation 3.2 shows that the increase in droplet size will lead to a decrease in cooling rate. The increase in cooling rate will promote the amount of undercooling the droplet undergone and produce more effective nucleation sites for more grain to be formed in a fixed volume. Also, a fast cooling rate means a short time for grain growth to take place. By combining the above two factors, a smaller powder size will lead to a smaller cell spacing.

The effect of Mg

At the same particle size and therefore, similar cooling rate, Al3Mg0.2Sc powder has a smaller cell spacing compared to Al1.5Mg0.2Sc powder. This phenomenon could be explained by the constitutional undercooling. During a solidification process, the formation of Al alpha phase is accompanied by ejecting Mg into the liquid phase following the liquidus and solidus line on the phase diagram. At the liquid/solid interface, if the ejected Mg is not diffused away efficiently, a local enrichment of Mg will be resulted, which in turn, will lead to a higher liquidus temperature. If the thermal gradient is lower than the liquidus temperature gradient, a constitutional undercooling zone will be formed. Figure 3.17 shows an example of constitutional undercooled region at the growth tip.

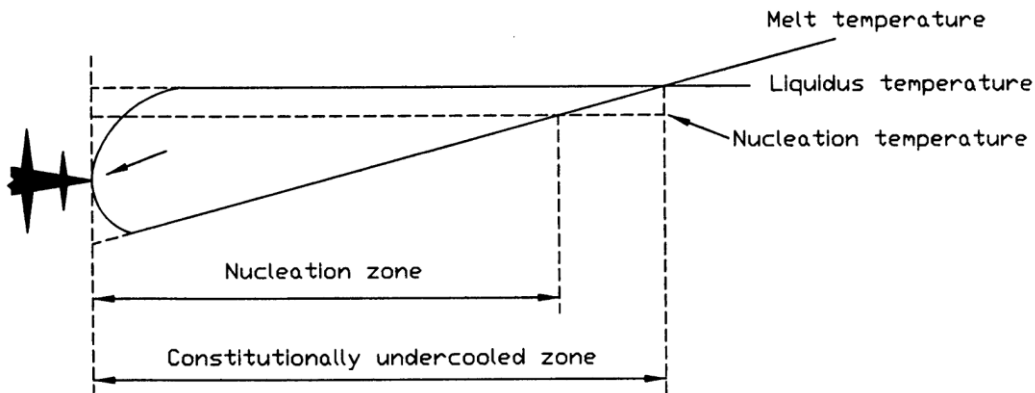


Figure 3.17: Constitutional undercooling region in the front of a dendritic tip [60]

The formation of this constitutional undercooled zone will promote nucleation such as the formation of secondary dendritic arms on the main dendritic arm walls, and therefore a smaller cell spacing. In addition, the growth restricting factor (GFR) is used to describe the segregation power of an element. GFR is expressed in equation 3.3:

$$GFR = m \cdot c_0 \cdot (k - 1) \quad 3.3$$

Where m is the liquidus gradient, c_0 is the bulk composition, and k is the partition coefficient [61]. In this equation, m and k could be considered constant for an alloy. Hence, GFR increases with higher solute concentration. It is reported that an initial rapid decrease in grain size with the increase GFR and reaches a minimum grain size at a critical solute concentration. In Table 3.10, the maximum concentration of Mg in aluminum is suggested to be about 3.40wt%, higher than the 1.5wt% and 3.0wt% Mg addition in the present work.

Table 3.10: Segregating power of elements in aluminum [60]

Element	k_i	m_i	$(k_i - 1)m$	Maximum concentration (wt%)	Reaction type
Ti	~ 9.0	30.7	245.6	15.00	Peritectic
Ta	2.5	70.0	105.0	~ 0.10	Peritectic
V	4.0	10.0	30.0	~ 0.10	Peritectic
Hf	2.4	8.0	11.2	~ 0.50	Peritectic
Mo	2.5	5.0	7.5	0.10	Peritectic
Zr	2.5	4.5	6.5	~ 0.11	Peritectic
Nb	1.5	13.3	6.6	~ 0.15	Peritectic
Si	0.11	- 6.6	5.9	~ 12.60	Eutectic
Cr	2.0	3.5	3.5	~ 0.40	Peritectic
Ni	0.007	- 3.3	3.3	~ 6.00	Eutectic
Mg	0.51	- 6.2	3.0	~ 3.40	Eutectic
Fe	0.02	- 3.0	2.9	~ 1.80	Eutectic
Cu	0.17	- 3.4	2.8	33.20	Eutectic
Mn	0.94	- 1.6	0.1	1.90	Eutectic

In summary, both the addition of Mg and the reduction in powder size will result in a smaller cell spacing, which means leading to a powder with finer grain.

Strip

The effect of different locations

Areas at various locations on the deposit experience different cooling rates. The top surface was cooled by heat convection of the gas present in the tower, the middle part was cooled by heat conduction to the upper and lower surfaces of the deposit, and the bottom surface was cooled by heat conduction to the copper substrate. As mentioned in the previous section, the difference in cooling rate should result in a difference in cell spacing. Therefore, cell spacing measurement was performed on the different locations along the axial direction of the spray deposit cross-section. A sample of images taken at various locations could be seen in the Figure 3.18.

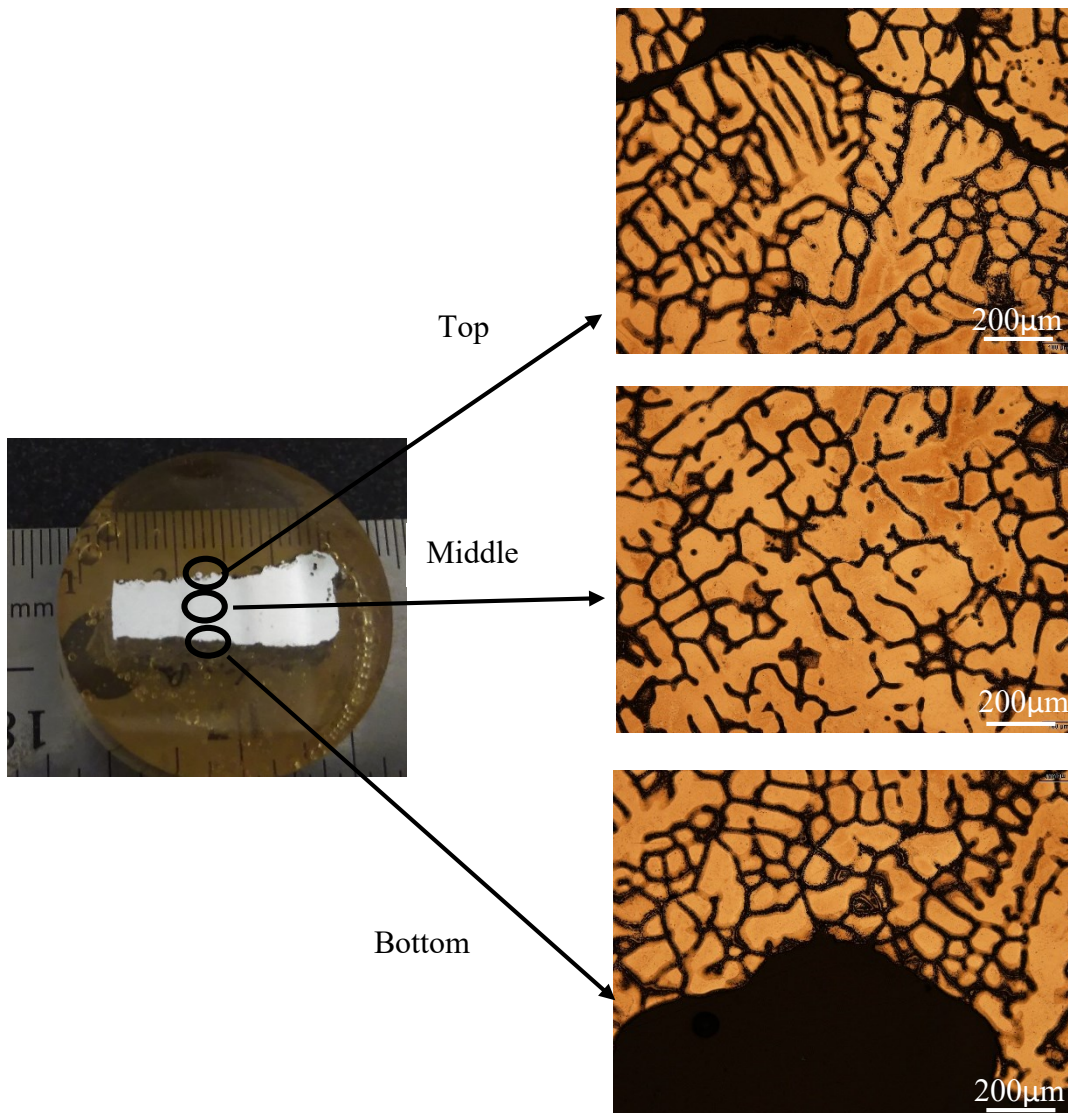


Figure 3.18: Sample images of strip $Al_3Mg_{0.2}Sc_{900^\circ C}$

Figure 3.19 below shows the cell spacing of Al1.5Mg0.2Sc and Al3Mg0.2Sc measured at different locations in the deposit.

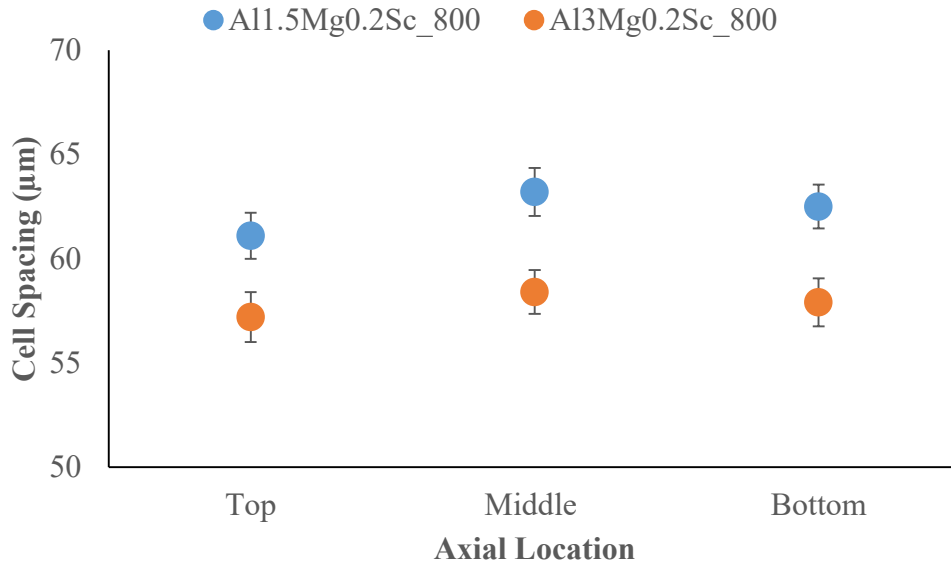


Figure 3.19: Cell spacing for Al1.5Mg0.2Sc_800 and Al3Mg0.2Sc_800 deposits at different sampling locations

The results do not show a noticeable difference in cell spacing through the thickness of the deposit. A similar trend has been observed in previous research done on the spray deposition process [62]. The strips produced by spray deposition are thin. This will lead to a low thermal history difference along the vertical direction. That being said, both of the alloys show a small cell spacing increase in the middle height of the strip, where the lowest cooling rate should be achieved among the three locations.

The Effect of Atomization Temperature

Figure 3.20 below shows that the increase of atomization temperature will lead to an increase in cell spacing. First, a higher superheat will lead to a lower percent solid upon landing the substrate. The cooling rate the droplets experienced on a flight is much higher compared with cooling on the substrate. Moreover, from the ICP result, more Mg are found to evaporate under high atomization temperature. This will lead to a reduction in Mg concentration in the alloy. As discussed above, solute contributes to reducing the cell spacing during solidification. Combined with these two factors, a higher cell spacing is observed with higher atomization temperature.

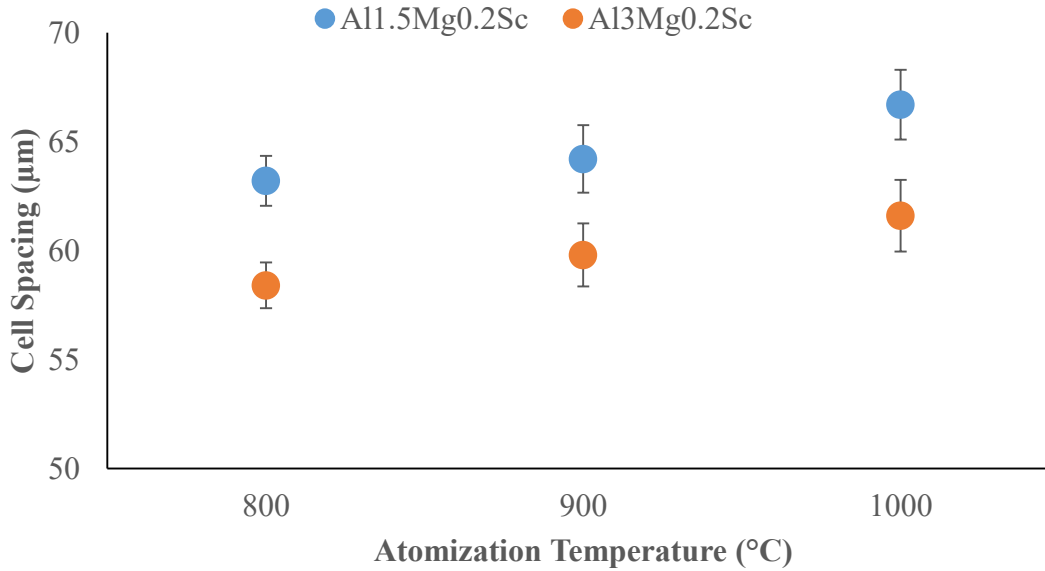


Figure 3.20: Cell spacing for Al_{1.5}Mg_{0.2}Sc and Al₃Mg_{0.2}Sc deposits

3.3.5. Microhardness measurements

The microhardness of mounted and polished samples were measured by using Buhler VH 3100 microhardness machine. The device is calibrated using a steel block provided by the manufacturer. According to the ASTM E113-e11, the temperature range of the samples is within the range of 10 – 35 °C. Since the samples are stored in the fridge at 0 °C to prevent natural aging, the samples are placed at room temperature for at least one hour prior to microhardness testing. The samples are then cleaned with warm water and alcohol and air dried before the hardness measurement.

The dwell time and load are set to be the same for all the measurements made on both powders and deposit. The dwell time is set to be 10 s which is within the range suggested by the ASTM standard. There is no specific requirement of the load to be used; however, it is mentioned in the ASTM standard that the larger the diagonal under the particular objective of view, the more accurate the result it would be. Hence, the biggest load is preferred if its indentation mark could be measured under X80 objective without a severe hardness drop. The optimum load is determined experimentally. The test starts with the lowest load available for the machine, 0.05gf and then this is increased to the point where the load starts to drop due to the powders being pushed into the mount. The smallest size

range 250-300 μm is selected as the test sample since it is the most sensitive to the load change. The plot of load vs. microhardness is shown in Figure 3.21.

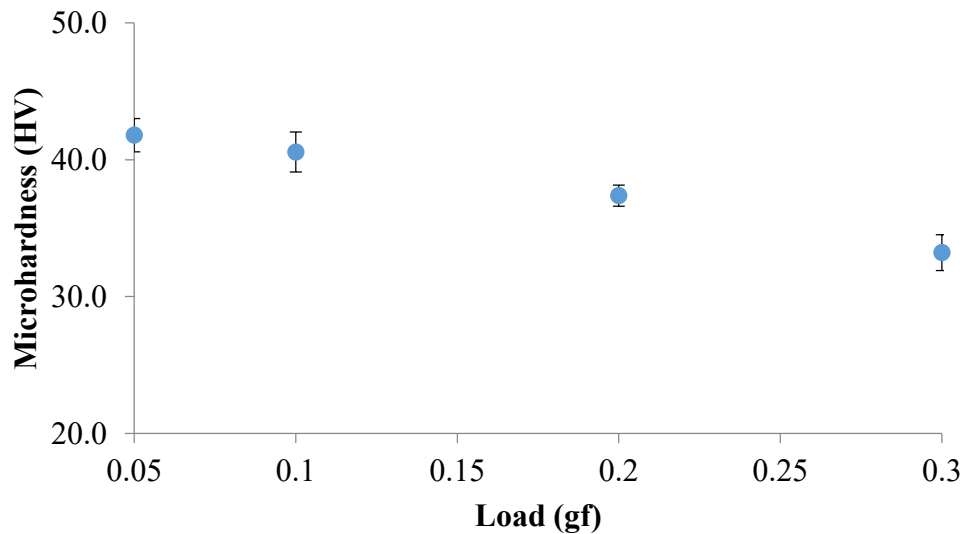


Figure 3.21: All.5Mg0.2Sc_Ar_250-300 with 10s dwell time

The hardness starts to drop when the load reaches to 0.2 gf; and therefore, 0.1gf is selected to be the test load.

For the powders, 10 points are measured on each sample, and both the hardness value and the diagonal length is recorded. According to the ASTM standard, the value could be accepted if both of the diagonals are longer than 19 μm , and the length of the two diagonals are within 5%. The measured points have to be validated so that they are representative. Average values and standard deviations are then calculated based on the measurement. The standard deviation is treated as an error during the comparison. The standard deviation is limited to be less than 5% if not; more points will be taken.

For the deposit, the overall thickness of the deposit is measured by the tool provided in the software. Moreover, the value is divided by 3 to differ the range of the area where is considered to be top, middle and bottom. Within each field, 10 points are taken, and the distance between each point should be at least 2.5 times larger than the diagonal of each indentation mark.

3.3.6. Aging

Furnace

Both the strips and the powders were age hardened with the use of Hageus Supermatic furnace. The strips were cut into 5mm width pieces along the length before putting into the furnace. The powders were poured into a small ceramic container before putting into the furnace. Before use, the oven was preheated to 300 °C. Eurotherm control box was used to set the aging time. The powders and sections of strips were heated for 30min, 1 hour, 1.5hours, and 2 hours; after the aging time was reached, the samples were then removed from the furnace and air cooled back to room temperature.

DSC

DSC analysis was performed on the IA and SD samples to monitor the heat flux variation during age hardening process. About 20mg of powders were weighed and put into TA Instrument DSC 2910. Nitrogen was used as the shielding gas. Before heating, the samples were equilibrated at 30 °C. The sample temperature was then ramped to 500°C at a rate of 20°C/min. After reaching the set temperature, forced air cooling was used to return the samples back to room temperature. Figure 3.22 below shows one of the DSC results of Al1.5Mg0.2Sc powders in the size range of 710-850µm.

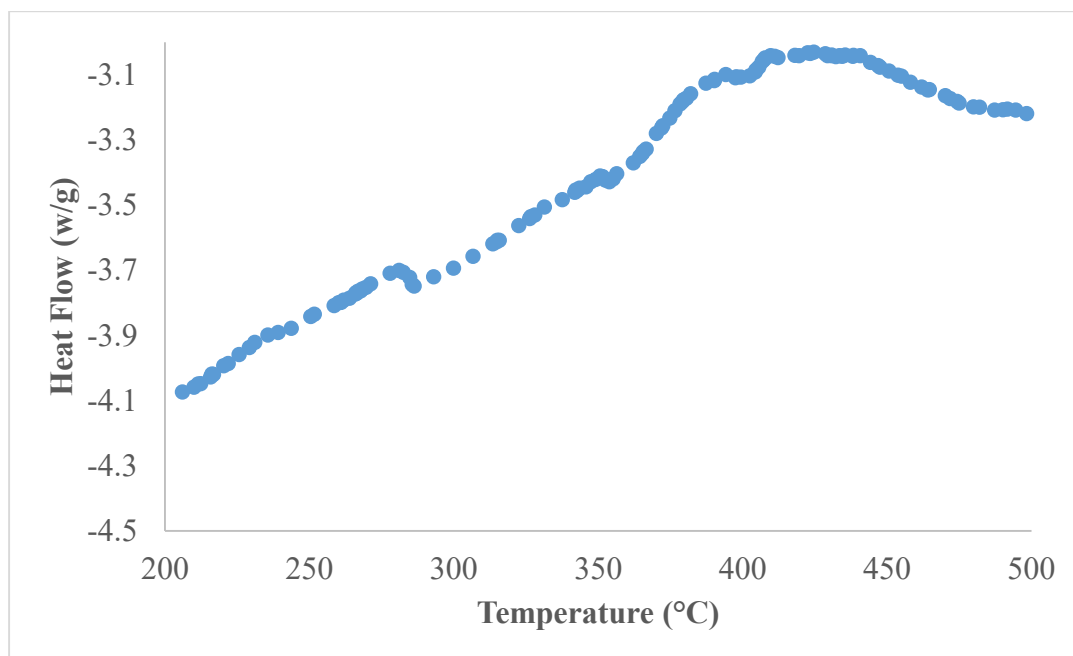


Figure 3.22: DSC curve for Al1.5Mg0.2Sc powders with 710-850 μm size range

Before running the samples, pure aluminum was run at the same setting, and the result was used as a baseline. As the precipitation energy of 0.2wt%Sc was considerably small compared to the overall peak, resulting temperature vs. energy curves were subtracted from the pure aluminum baseline to establish a more detailed plot. The subtracted plot for the curve is shown in Figure 3.23.

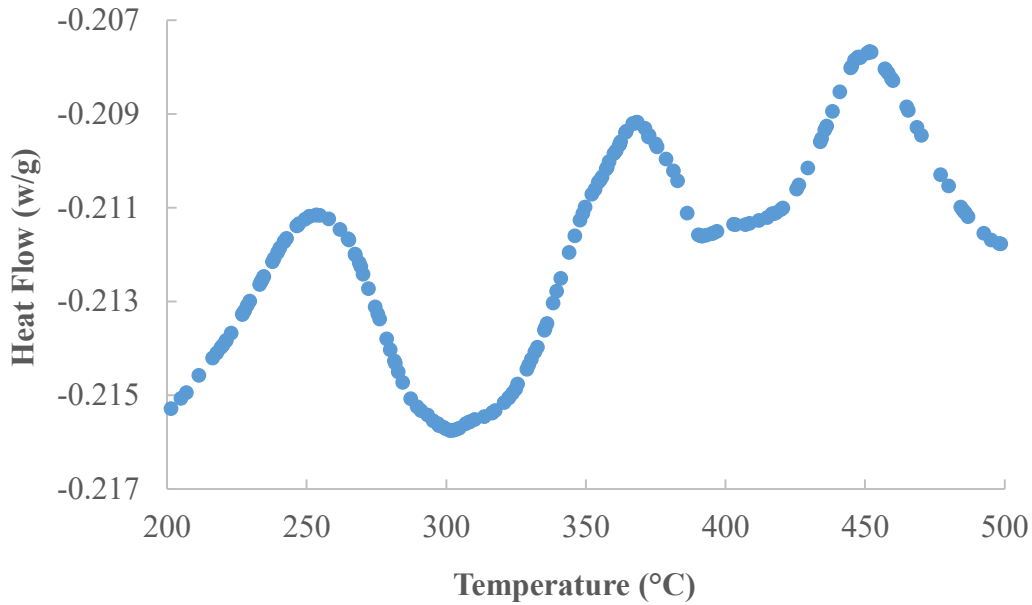


Figure 3.23: DSC curve for Al1.5Mg0.2Sc powders with 710-850 μm size range subtracted by the pure aluminum baseline

The DSC experiments were repeated at least one more time to ensure the results were repeatable. Some energy changes were observed in the above figure. The analysis of DSC results will be presented in next chapter.

3.4. Summary

Powders with Al1.5Mg0.2Sc and Al3Mg0.2Sc were produced with IA at 800-900°C atomization temperature. Strips of Al1.5Mg0.2Sc and Al3Mg0.2Sc were produced by IASD at 800°C, 900°C, and 1000°C atomization temperature. Nozzle plates with 350 μm orifice diameters were used for the above runs. Ar was used as the atomization gas. An infrared camera and an emissivity probe were selected to measure the top interface

temperature of the strip during spray deposition process, and a two-color pyrometer was selected to monitor the bottom interface temperature through a 0.45mm hole on the copper substrate.

The produced powders have a log-normal size distribution, and their $D_{50}/D_{\text{orifice}}$ is in a ratio of 1.3-1.5 range. Keller's solution was used to etch the powders and strips to reveal their microstructure. The chemical analysis acquired from ICP showed that as the atomization temperature increase, more Mg in the alloying system would be evaporated; but the amount of Mg vaporized was not critical comparing to the addition amount. Cell spacing measurement done on the powders and strips suggested a smaller particle size would relate to a finer cell spacing. Microhardness measurement done on the as-atomized and as-deposited products showed that cell spacing has a limited effect on the microhardness value. DSC results showed some energy change variation occurred as the temperature increases.

In next chapter, a relationship between the measured cell spacing and cooling rate will be drawn. Microhardness change as a function of aging time will be established. The effect of Sc precipitation during aging will be analyzed based on the DSC data.

4. Discussion

In this chapter, the cooling rate of the powder produced will be estimated with the use of a thermal model; and from the temperature measurement done during spray deposition process, the cooling rate of strips on the substrate will be estimated. The effect of cooling rate on cell spacing will be investigated. The microhardness change during age hardening process will be discussed. DSC results will be used to explain the aging behavior of Al_3Sc precipitates. In the end, a comparison will be made between the IA, IASD, and twin belt casting process.

4.1. Thermal Profile

4.1.1. Thermal Model

The background of this thermal model is described in the literature review section. Material properties data for $\text{Al}_{1.5}\text{Mg}_{0.2}\text{Sc}$ and $\text{Al}_3\text{Mg}_{0.2}\text{Sc}$ used in this thermal model are listed in Table 4.1 below:

Table 4.1: Material properties used in thermal model

Properties	Al_{1.5}Mg_{0.2}Sc	Al₃Mg_{0.2}Sc
ρ @ $T_{\text{atomization}}$ (kg/m ³)	2389	2319
K (w/m·k)	203.9	203.2
T_{liquidus} (K)	925	918
T_{eutectic} (K)	754	723
Latent Heat (J/kg)	372000	356000
ρ @ T_{room} (kg/m ³)	2679	2661
$C_{p\text{liquid}}$ (J/kg·K)	1179	1183

The material properties are found with the use of *Thermocalc TTAL7* database. The eutectic temperatures are determined by the temperature of last liquid to solidify under Scheil simulation. In addition to these constant values, the change of fraction solid, heat capacity and density as a function of temperature are needed.

Two equations are used in the model to describe the change of fraction solid as a function of temperature:

$$F_{s_1} = a_1 - \left(\frac{b_1 - T}{c_1} \right)^{d_1} + e_1 \cdot (T - f_1) + g_1 \cdot (T - 273)^2 + h_1 \cdot (T - 273)^3 \quad 4.1$$

And,

$$F_{s_2} = a_2 + b_2 \cdot (T - c_2) \quad 4.2$$

The constants in the equations above were determined with curve fit method in Excel. To obtain a solid fraction change as a function of temperature, a Scheil solidification paths were drawn using *Thermocalc* (*TTAL7 database*) for both Al1.5Mg0.2Sc and Al3Mg0.2Sc. Figure 4.1 shows such a curve for Al1.5Mg0.2Sc.

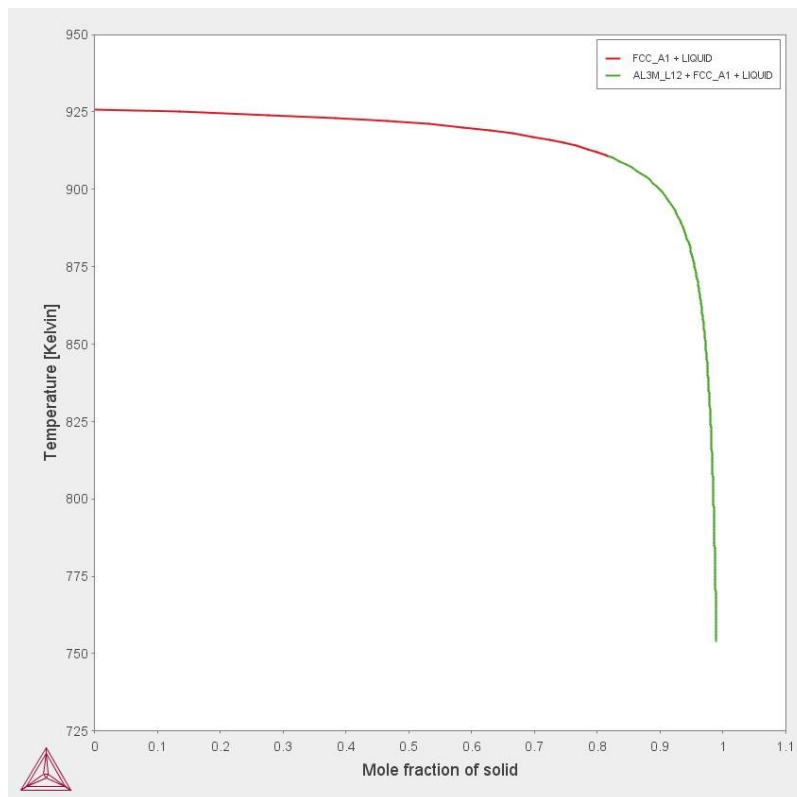


Figure 4.1: Al1.5Mg0.2Sc Scheil solidification path

A software *DataDigitizer* was used to transfer the curve into data points (fs, T) and entered into Excel. The constants in equations 4.1 and 4.2 were set to a series of randomly guessed numbers, as well as the transition temperature to switch from equation 4.1 to 4.2. By doing so, for each temperature, a solid fraction could be calculated. An absolute difference in solid fraction read from the curve and calculated from the equations was obtained for each

temperature step. A sum of these absolute difference was done. Using the “Solver” function in Excel, a minimum value for this sum of absolute difference was sought by changing the constants in equations 4.1 and 4.2 as well as the transition temperature. Figure 4-2 below shows the curve fitting result.

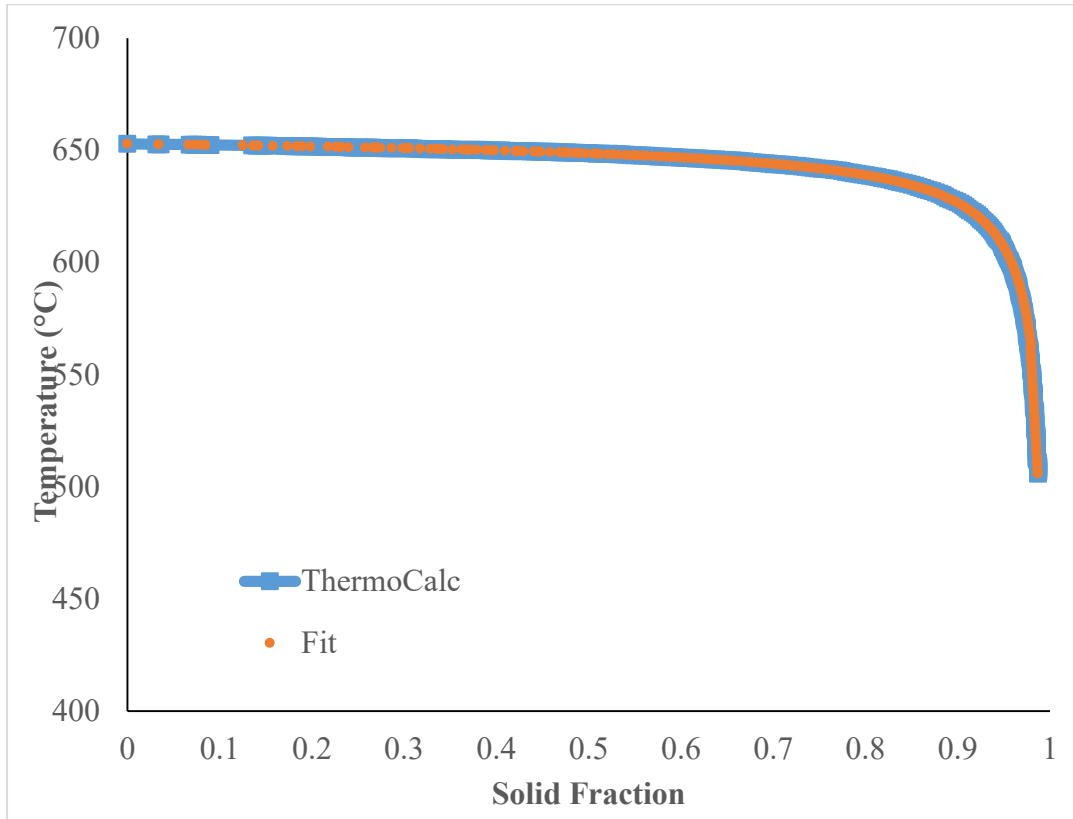


Figure 4-2: Curve fitting Scheil solidification path for Al1.5Mg0.2Sc

This practice was repeated for heat capacity and density for both alloys. After all the material properties had been gathered, the thermal model was run for both alloys with at different powder sizes. When running this model, the atomization atmosphere, gas temperature, droplet size, calculating time step, atomization temperature, simulation stop temperature, and initial velocity were entered. Solidification rate and freezing range are calculated by the model. A data file with droplet height, temperature, velocity, enthalpy, fraction solid, velocity and Reynolds number at each time step is also provided.

In this work, impulse atomization runs were done under Ar atmosphere with an 850°C atomization temperature. The cooling rates for Al1.5Mg0.2Sc and Al3Mg0.2Sc at different powder size can be seen in below.

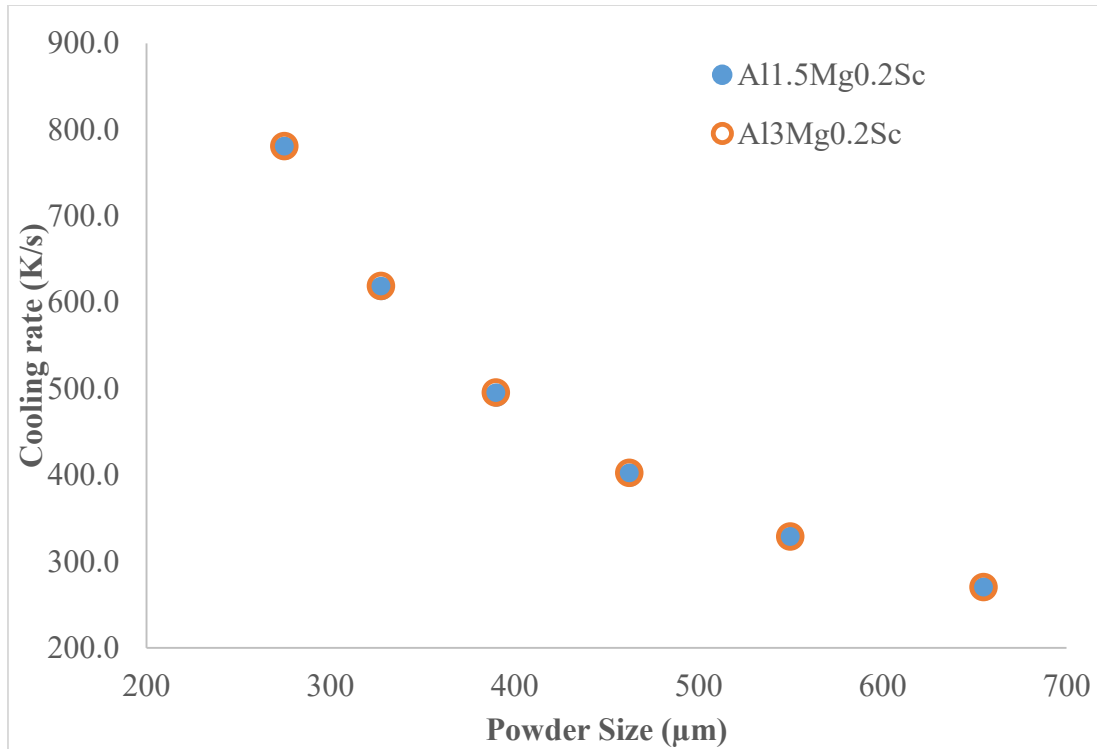


Figure 4-3: Powder size vs. cooling rate for Al1.5Mg0.2Sc and Al3Mg0.2Sc

The thermodynamic properties and density difference between these two alloys do not vary a lot. In the plot, their cooling rates almost overlapped with one and another at the same powder size.

For spray deposition, the thermal model was run with a similar setting as for powders but with the powder, size fixed at $490\mu\text{m}$, which is 1.4 times than the orifice size $350\mu\text{m}$. Different from impulse atomization, the droplets are deposited on a moving substrate 378mm below the nozzle plate. Therefore, in addition to the cooling rate, the solid fraction when the droplets hit the moving substrate is also important. A summary of solidification fractions at 378 mm below the nozzle plate and cooling rates for both Al1.5Mg0.2Sc and Al3Mg0.2Sc at different atomization temperatures can be seen in Table 4.2 below.

Table 4.2: Summary of thermal model result for spray deposition runs

Composition	Initial T (°C)	wt% solid @ 378mm	Cooling Rate (K/s)
Al1.5Mg0.2Sc	1000	0%	384
	900	26.1%	379
	800	46.2%	372
Al3Mg0.2Sc	1000	0%	383
	900	12.6%	378
	800	32.8%	369

At the same atomization temperature, the difference in cooling rate between these two alloys is marginal due to their similar thermodynamic properties. Compared to powder size, the atomization temperature has much less influence on the cooling rates of the droplets.

At 800°C and 900°C, Al1.5Mg0.2Sc reaches about 10wt% more solid due to its higher liquidus temperature compared to Al3Mg0.2Sc. At 1000°C, both of these alloys are still in the fully liquid state. As mentioned in the literature review section, a 40% solid fraction is found to provide the best balance between bonding and shrinkage porosity. Therefore, spray deposition of Al1.5Mg0.2Sc should be carried out in between 800-900°C; while for Al3Mg0.2Sc should be in the range below 800°C.

The thermal history for solidifying impulse atomized powder could be estimated by the thermal model. However, for spray deposition strips, another part of the solidification process takes place on the moving substrate. The thermal history of this part of solidification process is measured by the infrared camera, emissivity probe, and two color pyrometer system.

4.1.2. Interface temperature measurement

Before the use either Al1.5Mg0.2Sc or Al3Mg0.2Sc alloys, a temperature measurement atomization run was done with Al4.5Cu and 400µm orifice diameter nozzle plate at 800°C. Due to some technical issue, the data stored by the infrared camera could not be loaded. The data from emissivity probe could be seen in Figure 4.4 below:

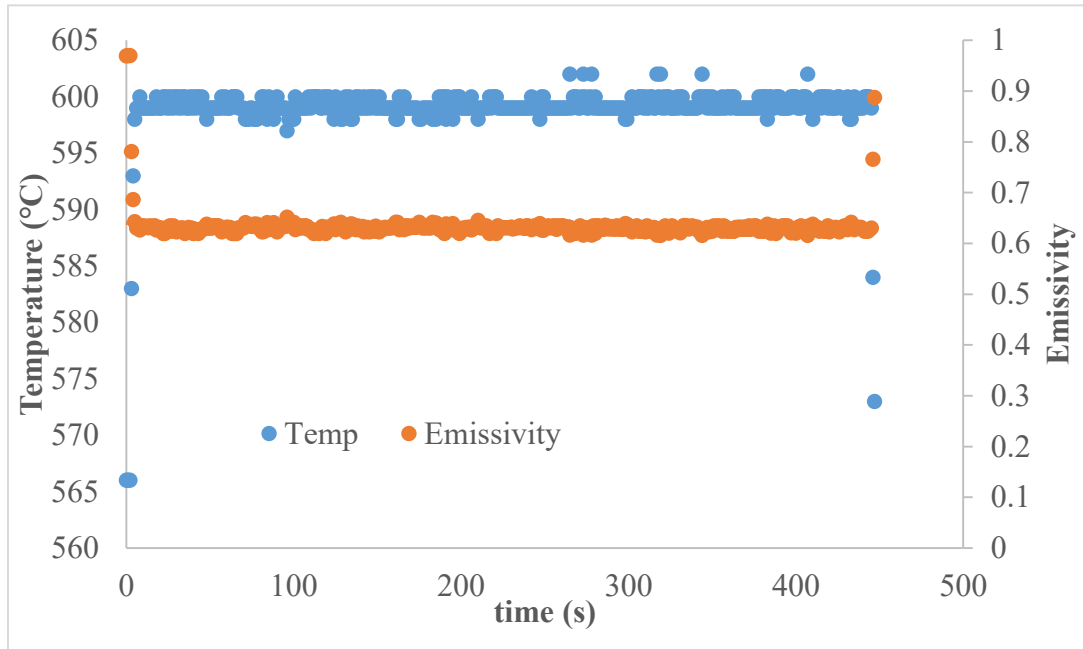


Figure 4.4: Emissivity Probe reading for Al4.5Cu

The temperatures shown in the plot are the temperatures for droplets just landing on the substrate. The aforementioned thermal model was run with Al4.5Cu material data published in previous research [12] [13]. With this setup (400 μ m orifice size, Ar, and 800°C atomization temperature), the estimated landing temperature should be around 594°C, which is close to the measured value 600°C. The emissivity measured from the probe is around 0.62, which is higher than the emissivity of aluminum reported in the literature [63]. The higher emissivity reading is due to the measurement was performed at an angle. The results from the two color pyrometer reading is shown in Figure 4.5:

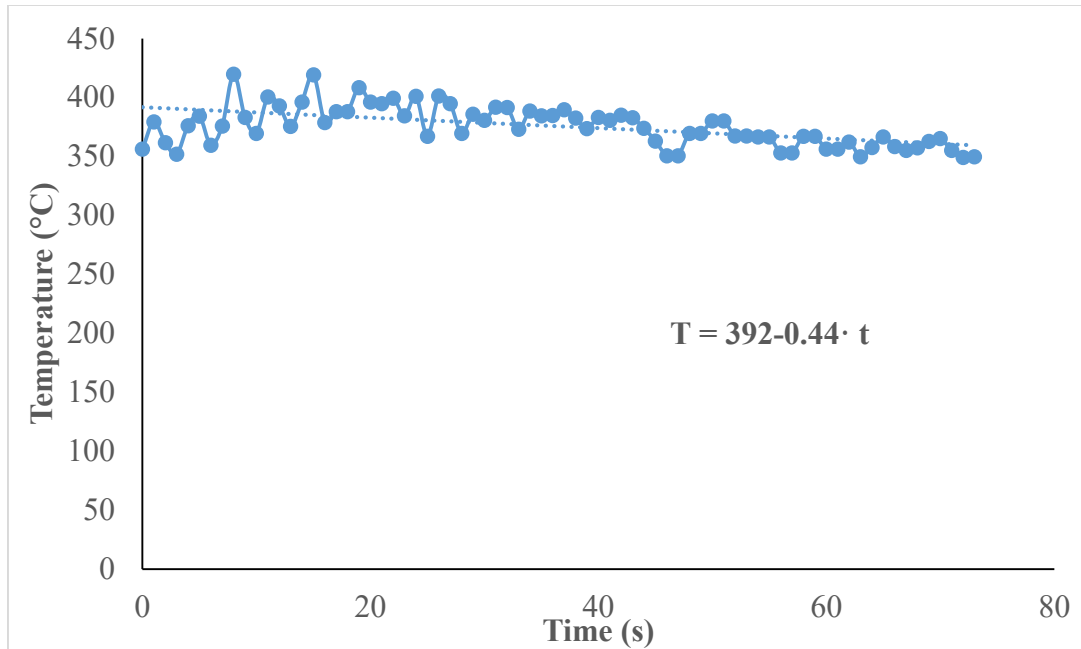


Figure 4.5: Two color pyrometer reading for Al4.5Cu

The temperature measured was the bottom interface temperature, where the deposited strip was in contact with the copper substrate. A linear trend line is fit on the curve. The equation suggests a cooling rate of 0.44K/s. As mentioned in the experiment section, the lower limit of the two color pyrometer is 350°C, and some of the data points fall off the limit. Therefore, for the temperature measurement run with Al3Mg0.2Sc, the atomization temperature was chosen to be 1000°C.

The emissivity probe and two color pyrometer data for Al3Mg0.2Sc with 350µm nozzle plate impulse atomized at 1000°C are shown in Figure 4.6 and Figure 4.7 below

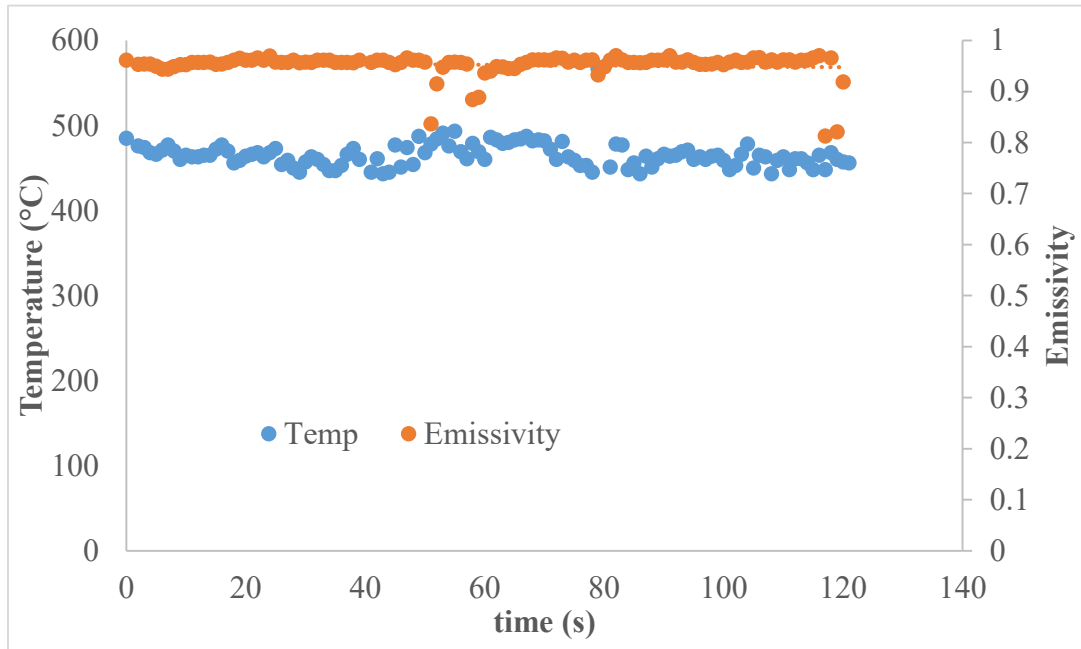


Figure 4.6: Emissivity Probe reading for $Al_3Mg_{0.2}Sc$

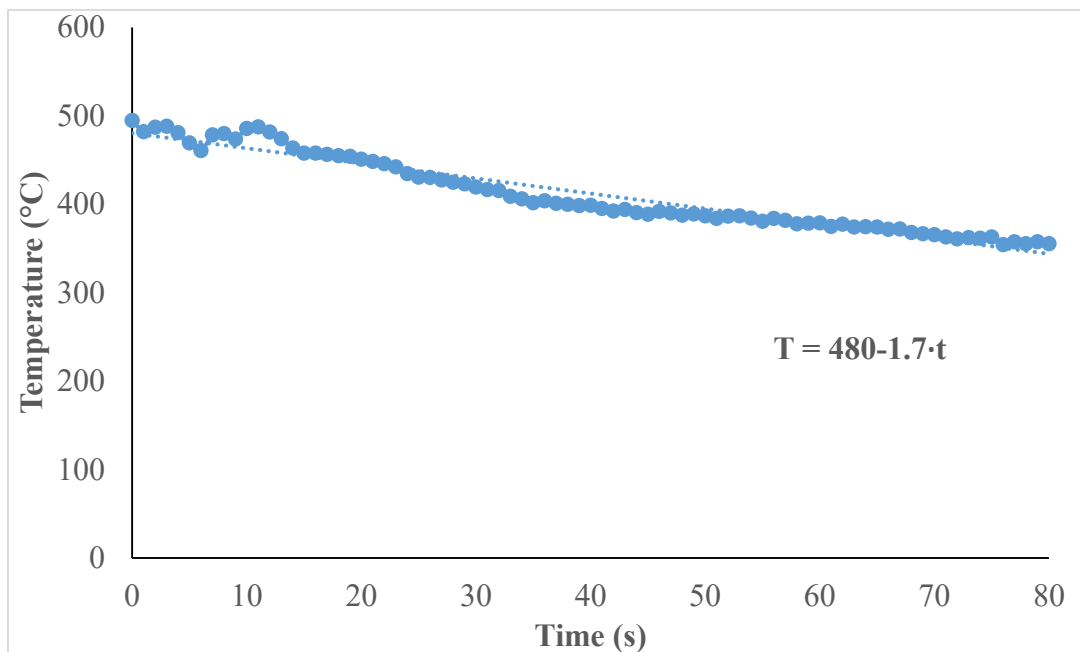


Figure 4.7: Two color pyrometer reading for $Al_3Mg_{0.2}Sc$

The emissivity probe reading is not valid since a significant amount of Mg was found to evaporate due to high atomization temperature. Some of them deposited on the cold IR window and blocked the view of the emissivity probe. With a higher atomization

temperature, on the other hand, resulted in a better two color pyrometer reading. The linear fit suggests a cooling rate of 1.7K/s was achieved after the droplets being deposited on the substrate.

Heat Removal

For powders, the heat transfer coefficient for a 490 μ m diameter Al3Mg0.2Sc powder, the average heat removal rate over the freezing range is reported to be 218 kW/ m² from the thermal model, assuming an ambient temperature of 25°C.

The average heat removed through the substrate in order to achieve a 1.7K/s cooling rate is calculated using the following equation:

$$\dot{q} = C_p \times \dot{T} \times \rho \times \frac{h}{2} \quad 4.3$$

In which, C_p is the heat capacity, \dot{T} is the cooling rate, ρ is the density, and h is the thickness of the strip (5mm). \dot{q} is calculated to be 28 kW/m².

4.2. Cell Spacing and Cooling Rate

In this section, the cooling rate's effects on cell spacing are investigated for both powders and strips.

4.2.1. Powder

The cooling rate's effects on the cell spacing measured are briefly discussed in the previous chapter. A more detailed analysis is performed here. By combining the cell spacing vs. powder size and cooling rate vs. powder size plot, a relation between the cell spacing and cooling rate could be drawn, as shown below:

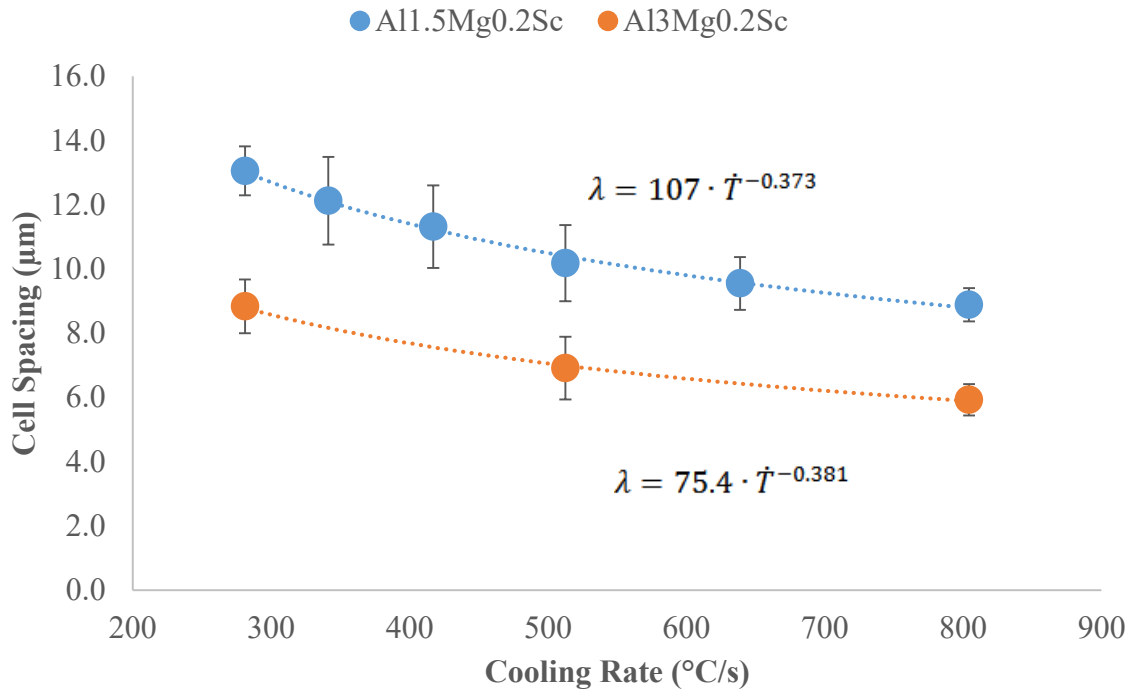


Figure 4.8: Cell spacing vs. cooling rate for Al1.5Mg0.2Sc and Al3Mg0.2Sc powders

Cell spacing could be expressed as a function of cooling rate as [64]:

$$\lambda = B \cdot \dot{T}^{-n} \quad 4.4$$

Another form of the cell spacing equation is described by the coarsening law, shown in equation 4.5:

$$\lambda = 5.5 \cdot (Mt)^{1/3} \quad 4.5$$

Where

$$t = \frac{\Delta T}{\dot{T}} \quad 4.6$$

And

$$M = \frac{\Gamma \cdot D \cdot \ln \left[\frac{c_l^m}{c_o} \right]}{m \cdot (1 - k) \cdot (c_o - c_l^m)} \quad 4.7$$

Γ is the Gibbs-Thompson coefficient; D is the diffusion coefficient of solute (Mg) in the liquid (Al), c_l^m is the last liquid to solidify (eutectic composition), c_0 is the overall composition, m is the slope of liquidus line, and k is the partition coefficient. Sc is not considered in this calculation. The diffusivity D could be calculated by:

$$D = D_0 \exp\left(\frac{-Q_a}{RT}\right) \quad 4.8$$

The material properties used are summarized in below:

Properties	Al1.5Mg0.2Sc	Al3Mg0.2Sc	Reference
D_0 (m ² /s)	1.49·10 ⁻⁵		[65]
Q_a (kJ/mol)	121		[66]
Γ (K·m)	10 ⁻⁷		[66]
c_l^m	34wt%		
c_0	1.5wt%	3.0wt%	[19]
m	-0.16		
k	0.42		
ΔT	195	171	
T_{liquidus} (K)	918	925	[67]
T_{eutectic} (K)	723	754	

The change of pre-exponential factor M in equation 4.5 with the change of T could be seen in Figure 4.9.

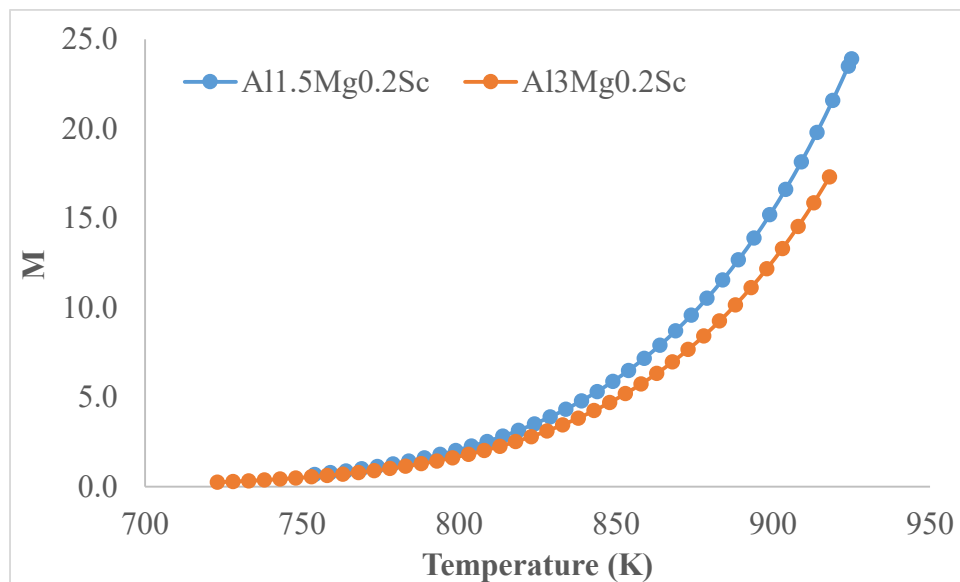


Figure 4.9: The pre-exponential factor M change with temperature

In order to compare the empirically determined pre-exponential factor B from the cell spacing vs. cooling rate plot (Figure 4.8), the calculated ranges of M values are converted to B using equation 4.9:

$$B = 5.5 \cdot (M \cdot \Delta T)^{1/3} \quad 4.9$$

This equation is derived by equating equation 4.4 and 4.5 while assuming n in equation 4.4 equals to 1/3.

The calculated maximum, minimum and average value of B over the freezing range for both Al1.5Mg0.2Sc and Al3Mg0.2Sc are tabulated below:

Table 4.3: Calculated constant B

Temperature	Al1.5Mg0.2Sc	Al3Mg0.2Sc
@T _{liquidus} (K)	87.9	82.5
@T _{eutectic} (K)	26.9	20.0
Avg. over ΔT	54.5	46.6

For both alloys, n should be around 0.33; in this work, the n values measured for Al1.5Mg0.2Sc and Al3Mg0.2Sc are 0.37 and 0.38 respectively, which agree with the theoretical value within 15%. For Al3Mg0.2Sc, the measured B value is within the suggested range. For Al1.5Mg0.2Sc, the measured B is 107, which lies outside the proposed range. There are several reasons might cause this. First, the calculation of B is very sensitive to the diffusivity of Mg; however, the diffusivity reported in the literature varies at least by 10%. Also, the c_l^m value also has a large impact on the result. However, from Scheil solidification path, no eutectic should form for Al1.5Mg; and hence, the c_l^m used here should not be the eutectic composition. If c_l^m used in the calculation was 10wt% instead of eutectic composition, the upper limit will be changed to 110, which the measured value will be within.

Once the relationship between the cooling rate and cell spacing has been established, the cooling rate measured by the two color pyrometer during the Al3Mg0.2Sc spray deposition run could be checked against the cell spacing measured.

4.2.2. Spray deposit

Figure 3.19 below shows the cell spacing vs. the vertical location of the spray deposit strips.

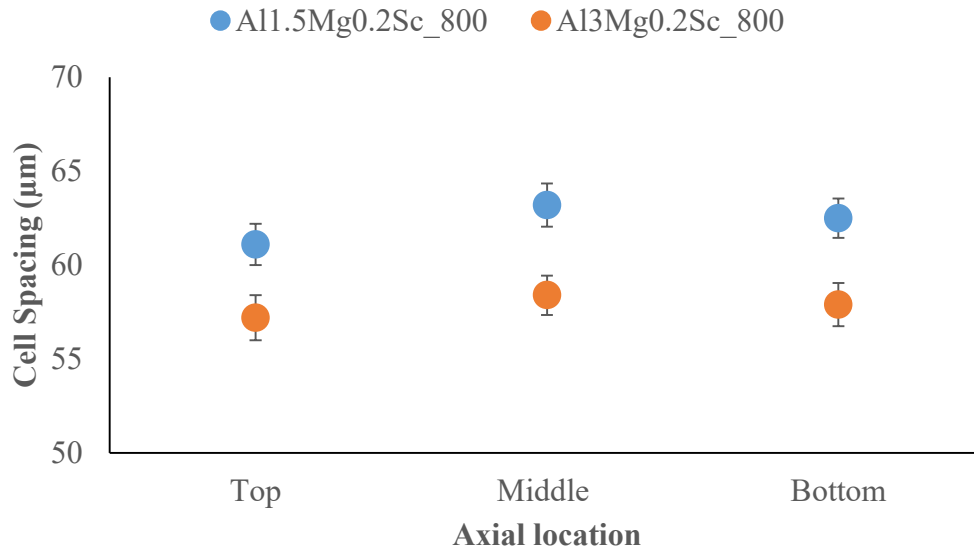


Figure 4.10: Cell spacing for Al1.5Mg0.2Sc_800 and Al3Mg0.2Sc_800 deposits at different sampling locations

The cell spacing near the middle position along the thickness of the strip is about the same as the ones near the bottom of the strip. The homogeneity of cell spacing is due to the high thermal conductivity of these aluminum alloys and rather small thickness of the spray deposited strip.

The Effect of Atomization Temperature

Figure 4.11 above shows that the increase of atomization temperature will lead to an increase in cell spacing. As the atomization temperature increase, the temperature at which the droplets land on the substrate also increases. Moreover, because of the cooling by conductive heat transfer through the copper substrate is much lower than cooling by forced convective heat transfer through Ar during free falling, a higher solidification rate could be achieved at a lower atomization temperature. Due to a slow solidification rate, the cell spacing of the deposit is about seven times greater than the cell spacing for the largest powder measured in this work. Another result could be seen in the figure above is that as the atomization temperature increase, the cell spacing difference between Al1.5Mg0.2Sc and Al3Mg0.2Sc samples is reduced.

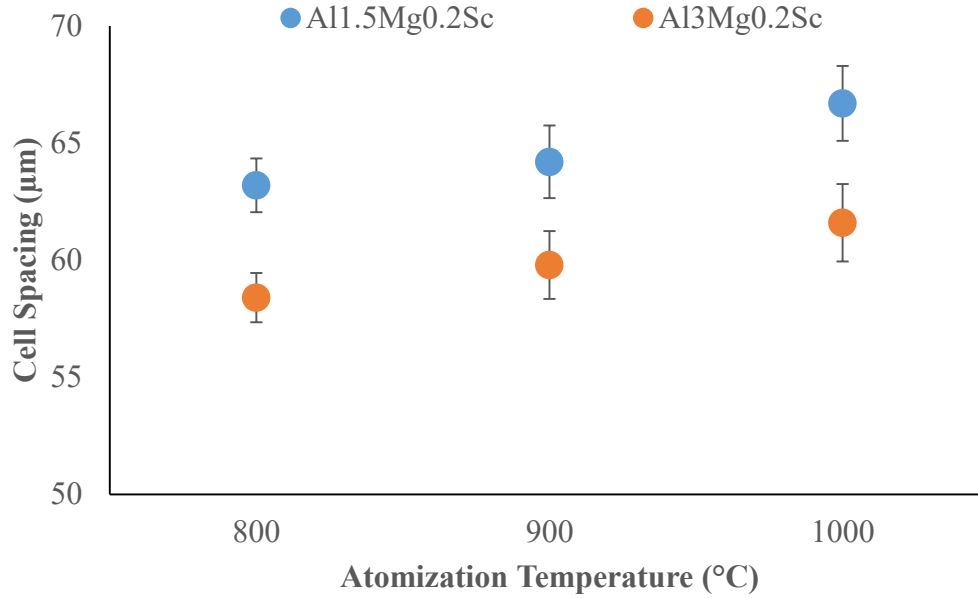


Figure 4.11: Cell spacing for Al1.5Mg0.2Sc and Al3Mg0.2Sc deposits

At 1000°C atomization temperature, the measured cell spacing is about 61.6 µm, which should be about the same for the cell spacing near the bottom height of the strip. The measured cooling rate at near the bottom interface is 1.7K/s. Based on the n and B values estimated based on our measurement, the calculated cell spacing is 61 µm. This agreement further proves the validity of the measurements done in this work.

To sum up, for spray deposited strips, Al3Mg0.2Sc alloys have smaller cell spacing, i.e. finer structure than Al1.5Mg0.2 under the same experiment condition. In the same run, the cell spacing tends to be homogenous through the thickness of the sample due to the strip is thin. The cell spacing is about seven times greater than powders. A higher atomization temperature tends to lead to a higher cell spacing.

4.3. Microhardness

Microhardness measurements are taken on the impulse atomized powders and spray deposited strips.

4.3.1. Powders

Figure 4.12 below shows the Vickers microhardness measured from Al1.5Mg0.2Sc and Al3Mg0.2Sc powders at different cell spacings.

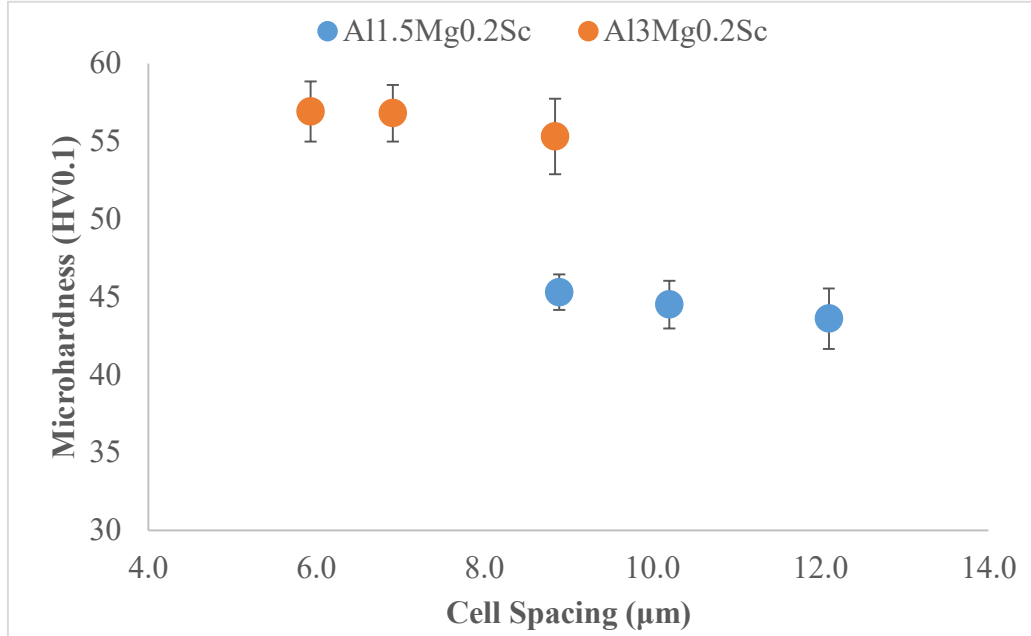


Figure 4.12: Microhardness for Al1.5Mg0.2Sc and Al3Mg0.2Sc powders

The Effect of Mg

It can be seen from Figure 4.12 that at each size range; Al3Mg0.2Sc samples shows a higher microhardness than Al1.5Mg0.2Sc. The extra hardening for Al3Mg0.2Sc is the result of the substitutional solid solution hardening effect of Mg. Due their similarity in size, Mg atoms substitute Al atoms in the α matrix lattice leading to a spherical strain field around the solute atoms due to the size and modulus differences between the Al matrix and the Mg solute atoms. The movement of dislocations will be blocked by this force field during deformation [23]. The hardness increase $\Delta\sigma_{ss}$ due to the addition of Mg could be estimated by using Equation 4.10 below [68]:

$$\Delta\sigma_{ss} = H \cdot C^\alpha \quad 4.10$$

Where H and α are material constants that are found to be 13.8 MP/wt% α and 1.14 respectively [69]. The $\Delta\sigma_{ss}$ difference between substitution in 3wt% Mg and 1.5wt% Mg is calculated to be 26.4 MPa.

The other trend that was found in Figure 4.12 is that the microhardness for Al1.5Mg0.2Sc and Al3Mg0.2Sc samples increase with smaller cell spacing. As the cell spacing reduces with increasing cooling rate, i.e. smaller powder size, the finer powders will result in better

microhardness. The effect of cell spacing to the microhardness will be discussed in detail after the presentation of microhardness data for strips.

4.3.2. Spray deposit

The Effect of location

Similar to what have been done to the cell spacing measurement, the microhardness for deposits at different locations were compared. The result could be seen below.

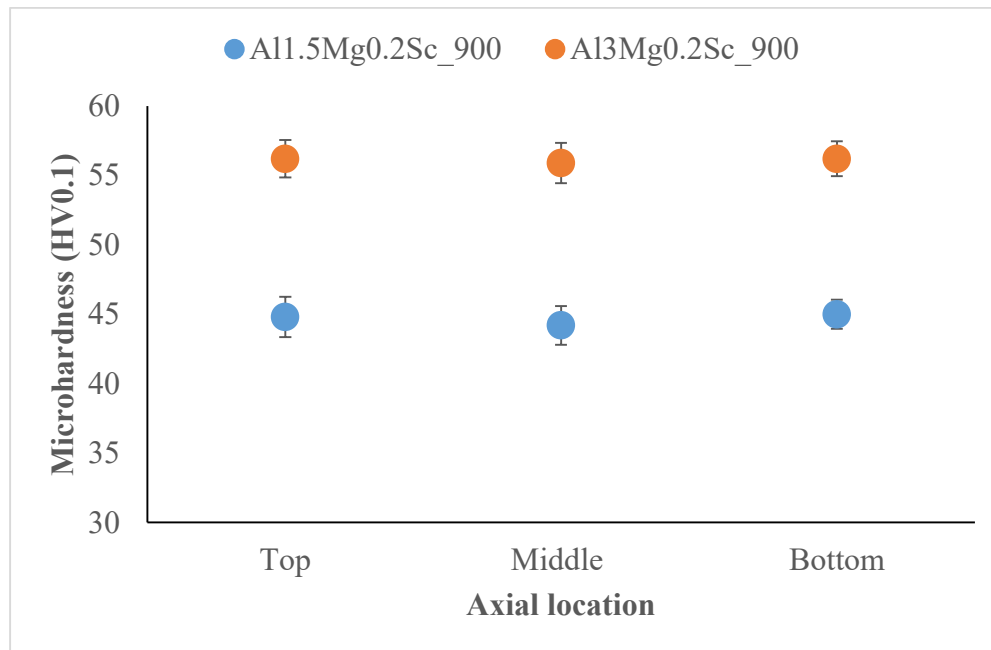


Figure 4.13: Microhardness for Al1.5Mg0.2Sc_900 and Al3Mg0.2Sc_900 at different axial locations

The microhardness at the middle part for both samples are slightly lower than the microhardness from the top and bottom part; however, if the standard deviations are considered, the microhardness at these three different locations are overlapping. The slightly decrease at the middle part of the deposit can be explained by its relatively low cooling rate which leads to a little larger grain size. The effect of atomization temperature is discussed next.

The Effect of Atomization Temperature

Al1.5Mg0.2Sc and Al3Mg0.2Sc deposits produced at different atomization temperature was measured. The result could be seen in Figure 4.14 below.

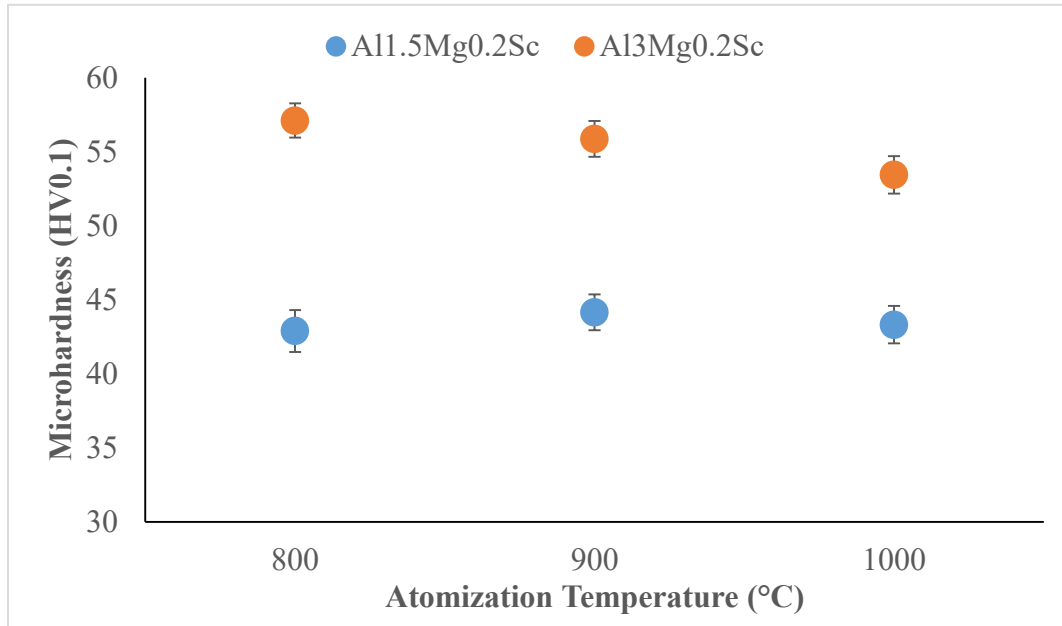


Figure 4.14: Microhardness for Al1.5Mg0.2Sc and Al3Mg0.2Sc deposits

It can be seen that the atomization temperature does not have any effect on the microhardness of the strip. As mentioned before, Mg contributes to the strengthening of as-cast Al-Mg alloys. From the ICP result, a slight decrease in Mg concentration is measured as atomization temperature increases for Al3Mg0.2Sc. This difference in Mg level could be used to explain a slight reduction in microhardness with increase atomization temperature for Al3Mg0.2Sc.

4.3.3. Cell Spacing vs. Microhardness

Hall-Petch effects describes the yield strength decreases as a function of grain size increases due to grain boundary's effect on obstacle the movement of dislocations during plastic deformation. In this study, due to the fact that the microstructure of the powder is a single crystal [70] and the obvious difficulty to apply a tensile test, a direct relation between yield strength and grain boundary is not applicable.

As for powders, cell spacing is used to evaluate the scale of microstructure and microhardness (which could be related to the yield strength) is used to assess the mechanical properties. Therefore, the idea of Hall-Petch effect is borrowed in this work to correlate cell spacing and microhardness value to see how a finer microstructure relates to

the microhardness for powders and strips. According to Hall-Petch effect, an inverse relationship should exist between the yield strength $\Delta\sigma_{gb}$ and the grain size (D):

$$\Delta\sigma_{gb} = kD^{-1/2} \quad 4.11$$

The k_h is reported to be $40 \text{ HV}\mu\text{m}^{1/2}$ and $45 \text{ HV}\mu\text{m}^{1/2}$ for 1.5wt% and 3wt% Mg addition to the Al-Mg alloys [71]. Figure 4.15 shows the relation between the $d^{-1/2}$ and microhardness for powders and strips.

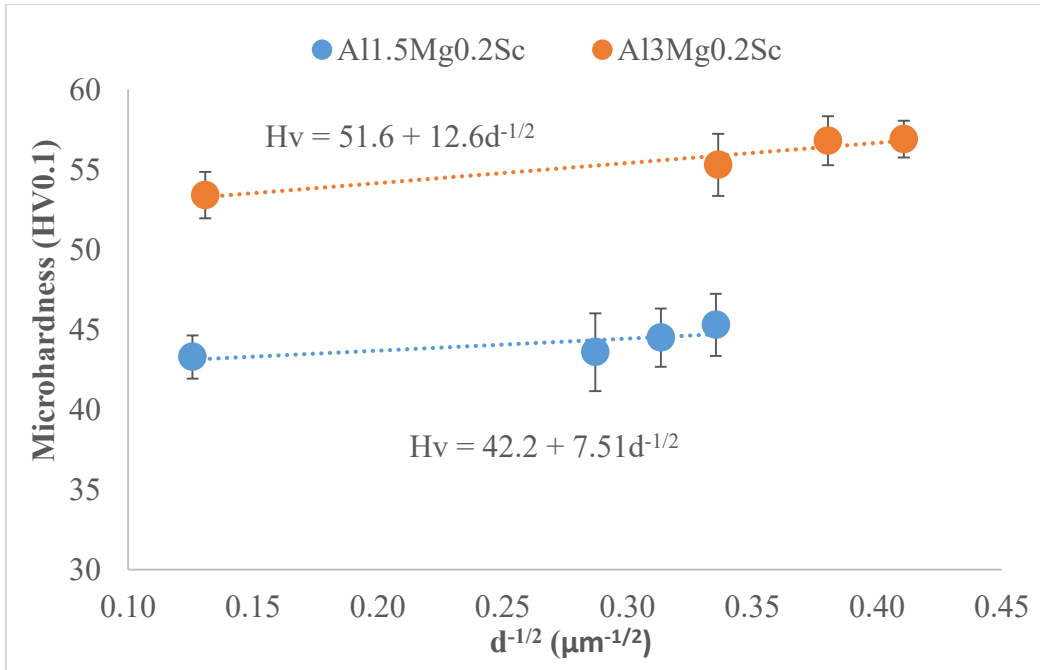


Figure 4.15: Microhardness for Al1.5Mg0.2Sc and Al3Mg0.2Sc deposits

Our measured values are $7.51 \text{ HV}\mu\text{m}^{1/2}$ and $12.6 \text{ HV}\mu\text{m}^{1/2}$ for Al1.5Mg0.2Sc and Al3Mg0.2Sc, which shows the same trend as the Hall Petch relationship. It is also worth noting that the strengthening effect of cell boundary is much less effective than the effect of grain boundary.

4.4. Age Hardening

One of the advantages of Impulse Atomized produced powders and deposits are the restriction of Macro-segregation making the solute dispersed more homogeneously in the matrix than in a casting. Therefore, age hardening could be performed directly on the as-atomized samples without being solutionizing, quenching then age hardening. In this study,

the age hardening of the sample was carried out at 300 °C and held for different aging times. The reason for age hardening at 300 °C is that Al₃Sc precipitate, which is stated to promote the precipitation hardening of Al-Mg alloys [72].

4.4.1. Age Hardening Effect on Powders

Al_{1.5}Mg_{0.2}Sc

The effect of age hardening for powders was studied first. Figure 4.16 below shows the microhardness for Al_{1.5}Mg_{0.2}Sc age hardened at 300 °C for different aging times.

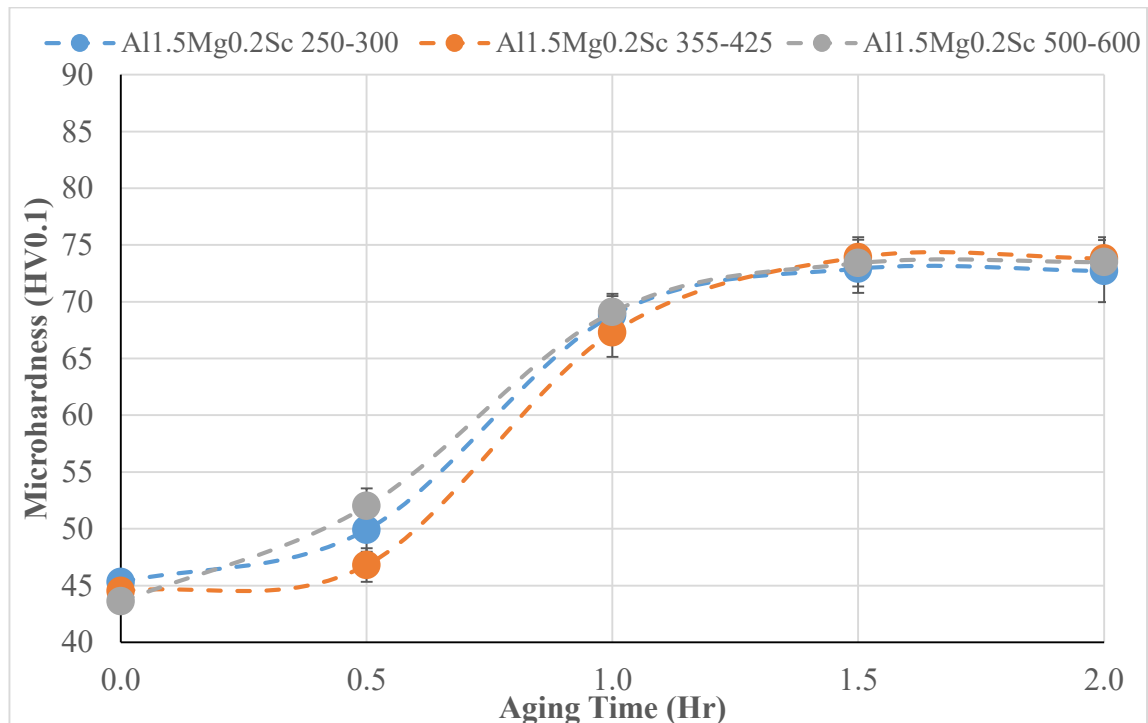


Figure 4.16: Microhardness for Al_{1.5}Mg_{0.2}Sc powders aged at 300 °C

The age hardening effect increased in the first 1 hour; an additional 30 min would barely increase the microhardness. The age hardening effect reduced significantly after 1.5hrs as the hardness for sample age hardened for 2 hrs does not change from the hardness measured for samples age hardened for 1.5 hrs. In age hardening, two things happen simultaneously: precipitation hardening and grain growth. After 1 hour of age hardening, the precipitate formation rate slowdown and the strengthening effect from it is countered by grain growth.

The Al_{1.5}Mg_{0.2}Sc powders start off with about the same microhardness and following similar age hardening path, and finally reach to the same maximum microhardness value

after age hardening. Therefore, it can be concluded that, for the Al1.5Mg0.2Sc IA powders, the different in particle size, i.e. different cell spacing and cooling rate is not the rate determine step in establishing age hardening.

Al3Mg0.2Sc

Figure 4.17 below shows the microhardness for Al3Mg0.2Sc powders age hardened at 300 °C for different aging times.

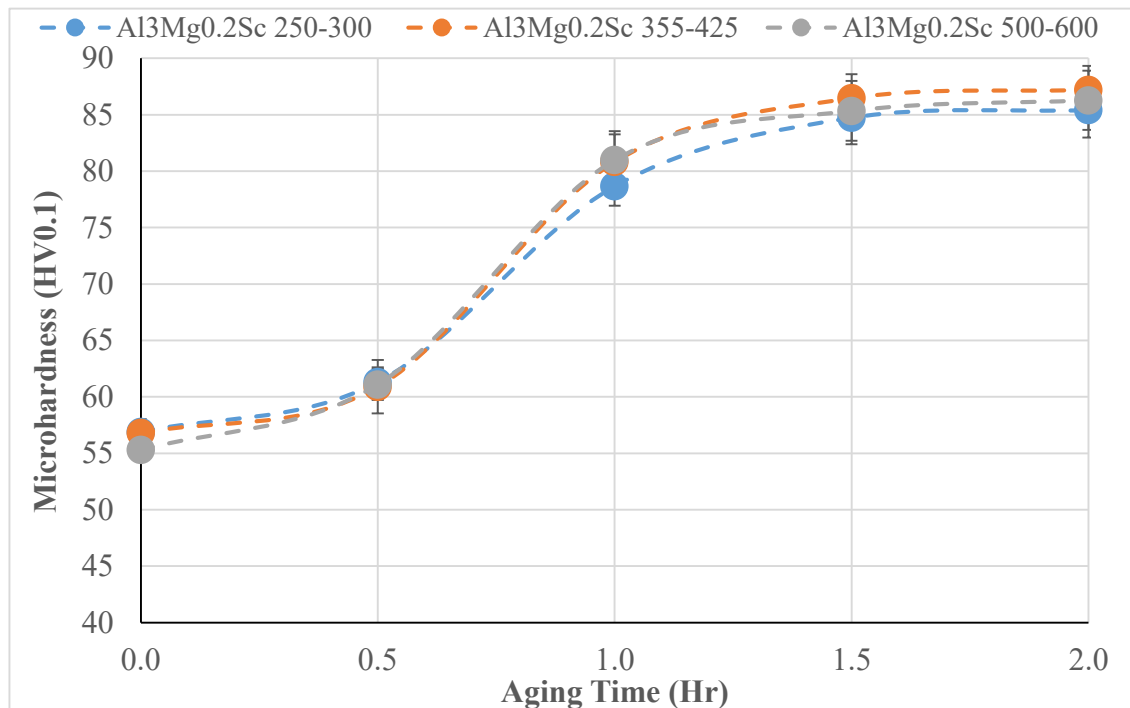


Figure 4.17: Microhardness for Al3Mg0.2Sc powders aged at 300 °C

Similar to Al1.5Mg0.2Sc powders, the first 1 hour of age hardening shows an increase in microhardness and the aging effect stopped after 1.5 hours of holding. Similar to IA Al1.5Mg0.2Sc powders, the powder size, cell spacing and cooling rate are negligible for age hardening effect for Al3Mg0.2Sc impulse atomized powders as well.

For Al1.5Mg0.2Sc and Al3Mg0.2Sc, at time zero, a difference in microhardness is observed due to the difference in Mg addition. After aging for 1.5 hours at 300°C, a similar microhardness increases are observed for Al1.5Mg0.2Sc and Al3Mg0.2Sc. The same amount of microhardness increase indicating that this is the role of Sc precipitates. In

addition, the addition of 1.5wt% Mg and 3.0wt% Mg do not seem to alter the precipitation hardening effect of Sc. This is suggested to be the extremely low solubility of Sc and Mg within each other [30].

4.4.2. Spray deposits

The age hardening effect on spray deposited samples will now be discussed

A11.5Mg0.2Sc

Figure 4.18 below shows the microhardness for A11.5Mg0.2Sc deposits age hardened at 300 °C for different age hardening times.

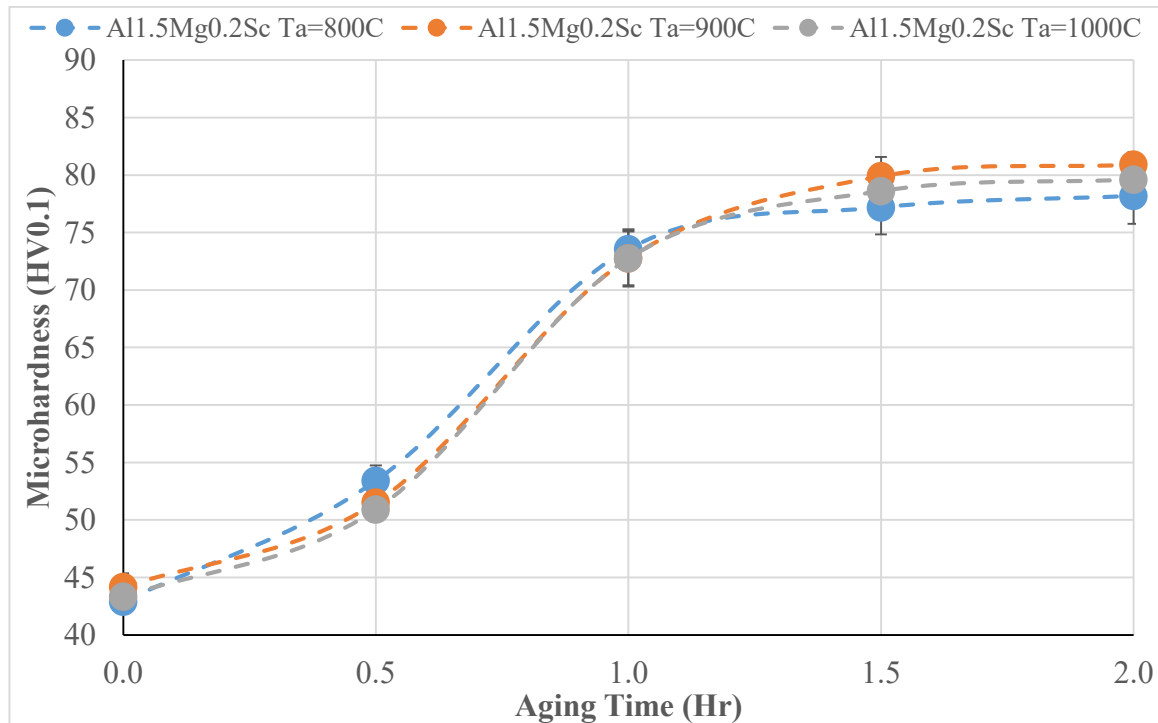


Figure 4.18: Microhardness for A11.5Mg0.2Sc deposits aged at 300 °C

The age hardening effect is similar to A11.5Mg0.2Sc powders. The difference is that the holding time stops causing microhardness to increase after 1.5 hrs rather than 1 hour for the powders; the peak microhardness for powders and deposits are the same. This further confirms that the cooling rate of alpha phase has limited effect on the age hardening performance of A11.5Mg0.2Sc IA powders and IASD strips.

Al₃Mg_{0.2}Sc

Figure 4.19 below shows the microhardness for Al₃Mg_{0.2}Sc deposits age hardened at 300 °C for different age hardening times.

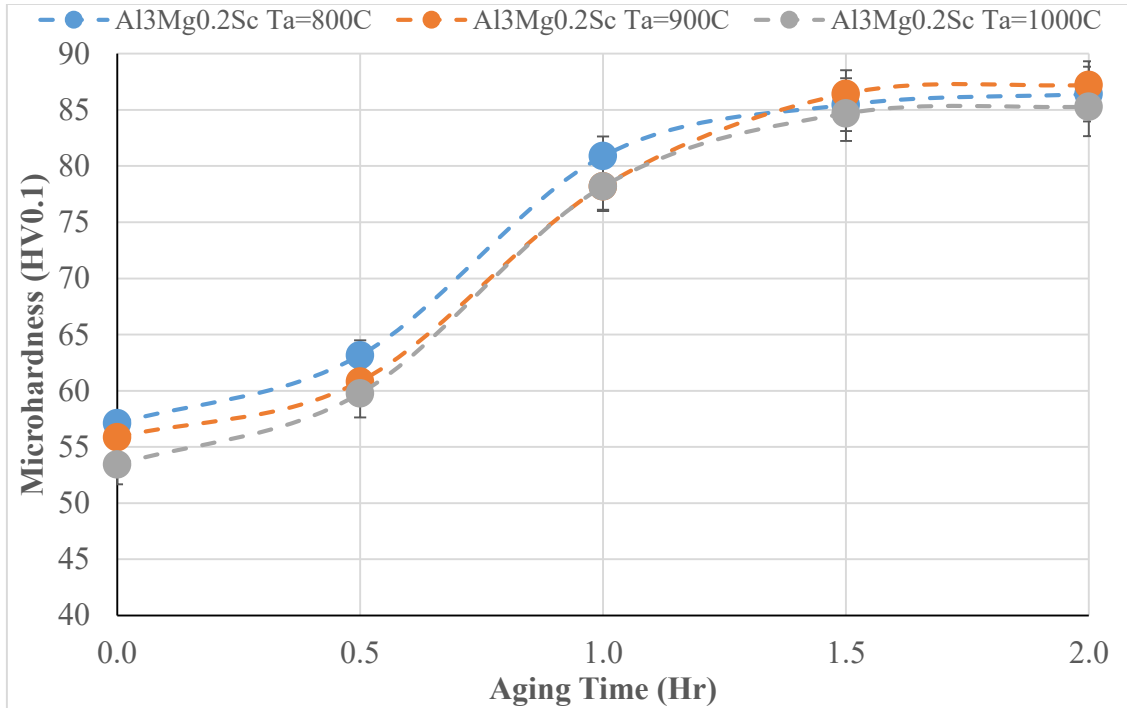


Figure 4.19: Microhardness for Al₃Mg_{0.2}Sc deposits aged at 300 °C

The age hardening trend for Al₃Mg_{0.2}Sc deposits is the same as it for the powders. Microhardness reaches its peak value after 1.5 hours of holding. Also, the strips produced at 1000 °C atomization temperature tends to have an overall slightly lower microhardness value. From the ICP results, Al₃Mg_{0.2}Sc atomized at 1000°C shows the least amount of Mg. Hence, the overall Mg solid solution strengthening effect is reduced.

In summary, for the same alloy composition, in both IA powders and IASD strips, the cooling rate of alpha phase does not affect the aging behavior of Sc. This suggests that the cooling rate range for IA and IASD is enough to achieve a reasonable supersaturation of Sc in aluminum alpha for both Al_{1.5}Mg_{0.2}Sc and Al₃Mg_{0.2}Sc. By comparing Al_{1.5}Mg_{0.2}Sc and Al₃Mg_{0.2}Sc, although a difference in microhardness is observed before age hardening, the overall microhardness increases are the same for these two compositions after 1.5 hours aging times. This indicates that the Sc precipitation

hardening effect of 0.2wt%Sc addition into aluminum magnesium alloy does not vary with 1.5wt%Mg and 3.0wt%Mg addition to the IA powders and IASD strips.

The mechanical property changes should be correlated to microstructural changes. Differential scanning calorimetry (DSC) was done to both powders and strips samples to see the how the heat flux change during the aging process.

4.4.3. DSC

As discussed in literature review section, Al-Mg alloys with Mg concentration less than 5wt% do not have any response to age hardening and are considered to be non-heat-treatable. In this work, the increase in strength after aging is attributed to the addition of 0.2wt% Sc.

When heated in a DSC, a temperature vs. heat flux plot could be drawn to see the change of heat flux as a function of temperature. If no microstructural change occurs, a smooth curve should be observed. A pure aluminum was aged first with the same settings as for the samples to be tested. A baseline for aluminum alloys was then established. After the samples had been run under DSC, the curve was then subtracted from the aluminum baseline curve to reveal the subtle changes. The results for impulse atomized powders of Al1.5Mg0.2Sc in 600-710 μ m size range are shown in Figure 4.20 below.

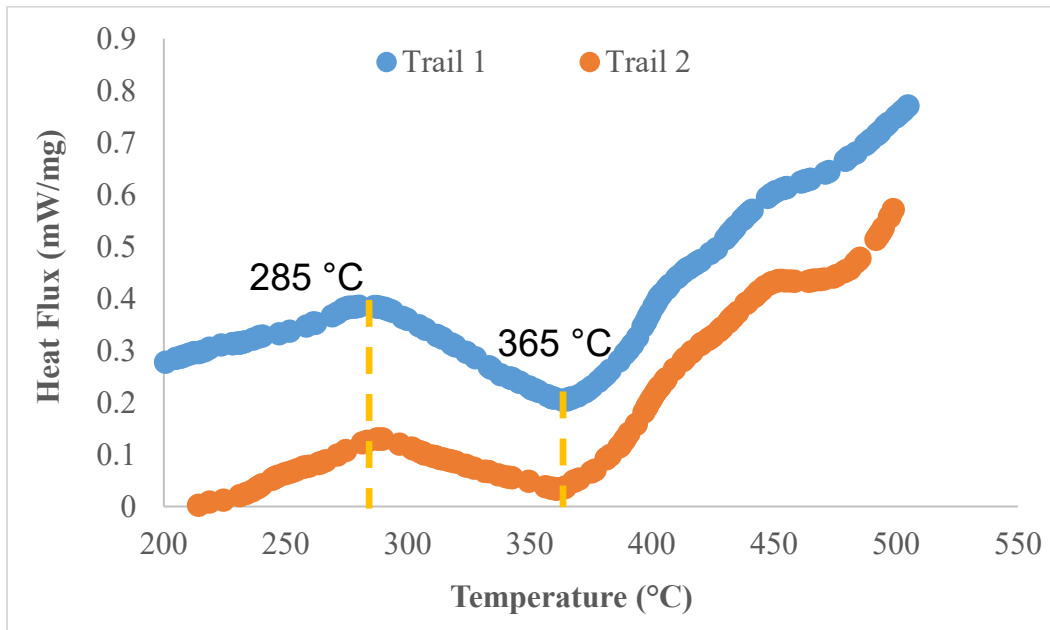


Figure 4.20: DSC result for two trials done on Al1.5Mg0.2Sc powders in 600-710 μ m diameter size range

An exothermic heat flux can be observed started at 285°C and ending at 365°C. Our aging temperature 300°C lies within this range. A ternary phase diagram corner for Al-Mg-Sc at 300°C is generated in *ThermoCalc* with the use of *TTAL7* database (Figure 4.21).

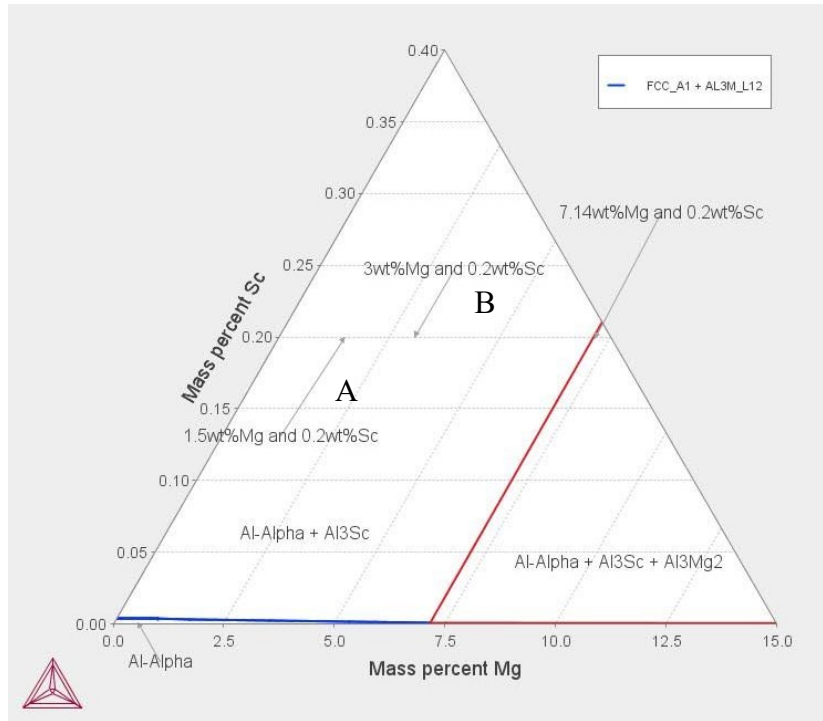


Figure 4.21: A corner of Al-Mg-Sc ternary phase diagram at 300°C

The two alloys tested in this work are shown by labels A and B. It can be seen from the ternary phase diagram corner, at 300°C, both of the alloy compositions investigated in this work are in the Al-Alpha and Al₃Sc area. Due to the high cooling rate, Sc is supersaturated in the primary alpha phase; and during aging, one would expect Sc precipitates to form. The size of the Al₃Sc precipitates is reported to be in the range of several nanometers (Figure 4.22).

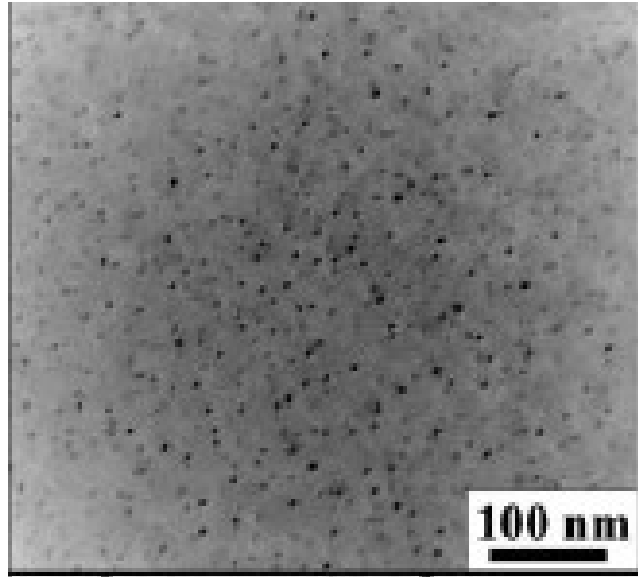


Figure 4.22: TEM micrograph of Al_3Sc precipitates for Al-2wt%Mg-0.2wt%Sc aged at 300°C for 24 hrs [5]

Due to the scope of this work, TEM has not been performed to visualize the size, shape, location and distribution of Al_3Sc precipitates after aging. The precipitates radius changing with the aging time at different aging temperatures is reported in Figure 4.24. At 300°C, the precipitates radius should be about 1 nm based on the plot after 2 hours. As mentioned in the literature review section, for Al_3Sc precipitates, the critical particle diameter where the maximum strengthening can be achieved is in the range of 2-3.7nm [4].

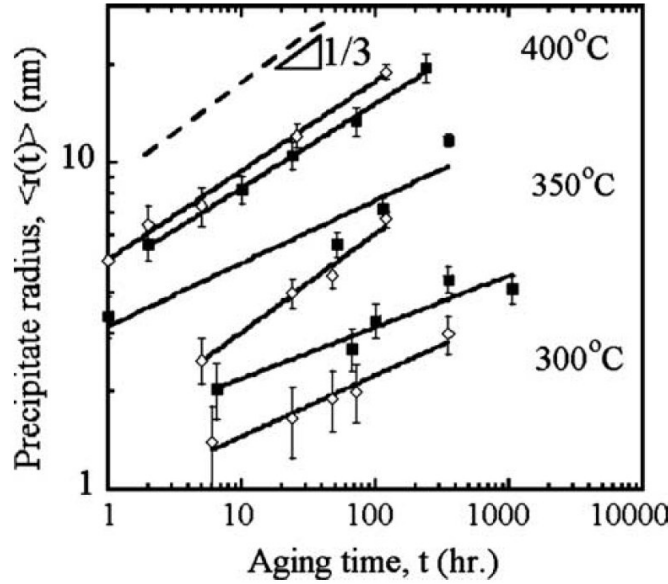


Figure 4.23: Al_3Sc precipitates radius growth at the different aging time under different aging temperature. [73]

As we establish the possible precipitate size during aging, it would be critical for us to see if precipitation is possible. A two-dimension random walk calculation was done for Mg and Sc atoms in the aluminum matrix at 300°C for various aging times. Equation 4.12 is used.

$$\overline{x^2} = 4 \cdot D \cdot t \quad 4.12$$

In which x is the average distance an atom could diffusive, D is the diffusivity of the atom and t is the time allowed for this diffusion to take place. The diffusivities of Mg and Sc atoms in the aluminum matrix at 300 °C are calculated to be $1.55 \times 10^{-4} \mu\text{m}^2/\text{s}$ and $1.29 \times 10^{-7} \mu\text{m}^2/\text{s}$ using equation 4.8. The activation energy and diffusion coefficient used for the calculation are 121 kJ/mol and $1.49 \times 10^{-5} \text{m}^2/\text{s}$ for Mg atoms in aluminum matrix [65]; and 168 kJ/mol and $2.64 \times 10^{-4} \text{m}^2/\text{s}$ for Sc atoms in aluminum matrix [74]. The random walk distance as a function of time could be seen in Figure 4.24 below. After 2hrs, the random walk distance for Sc in the aluminum matrix at 300°C is calculated to be $0.06 \mu\text{m}$, which is 60nm, about 60 times larger than the radius of the Al_3Sc precipitates. Therefore, the precipitation of Al_3Sc is possible.

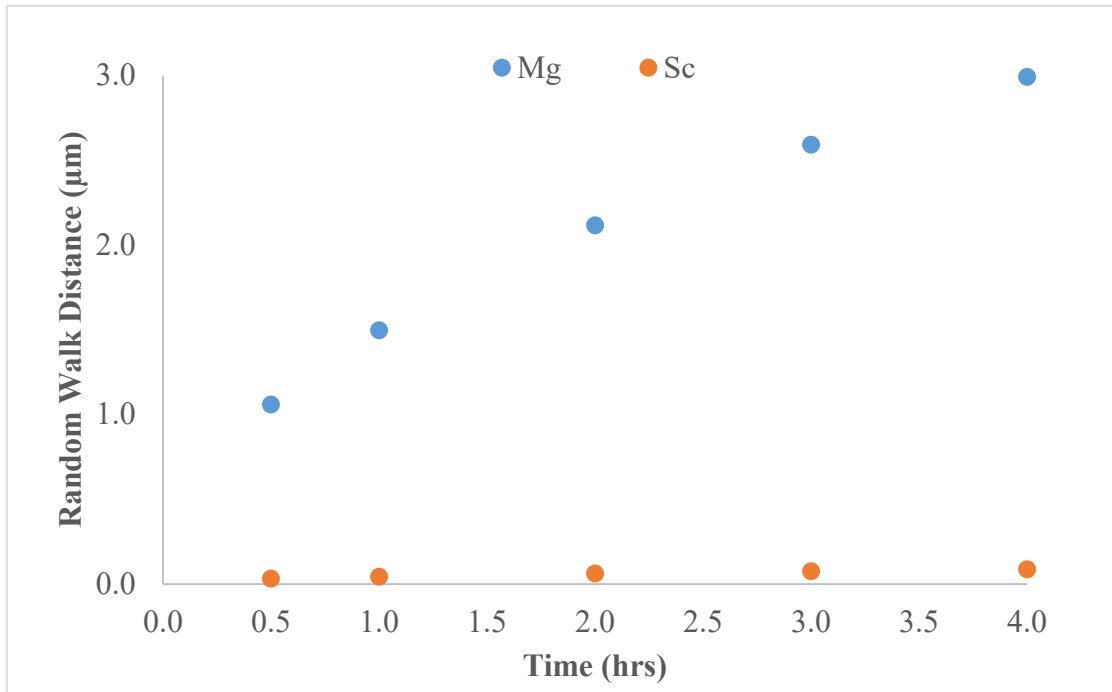


Figure 4.24: Random walk distance vs. time.

In summary, the microhardness increase after aging is due to the formation of Al_3Sc precipitates in nanometer radius after aging. The energy associated with this precipitation behavior has been observed by DSC measurement. Although TEM is not done due to the scope of this work, the radius of the precipitate should be 1-2nm based on literature. A random walk calculation shows the formation of these nano-sized precipitates is possible as the diffuse distance for Sc at 300°C for 2hrs is about 60 times larger than the precipitations radius.

4.5. Industrial Relevance

The reported cooling rates that are achieved by twin-belt casting is reported to be around 100K/s , which is in the range of impulse atomization and spray deposition process. The cell spacing reported for twin-belt casting is in the range of $40\text{-}50\mu\text{m}$ [75]. Figure 4.25 below shows a grain structure of the as strip casted $\text{Al}_{13}\text{Mg}_{0.4}\text{Sc}$ alloy 1mm from the cast surface. By applying the same cell spacing measurement method on the image, an average $48.7\mu\text{m}$ cell spacing is measured.

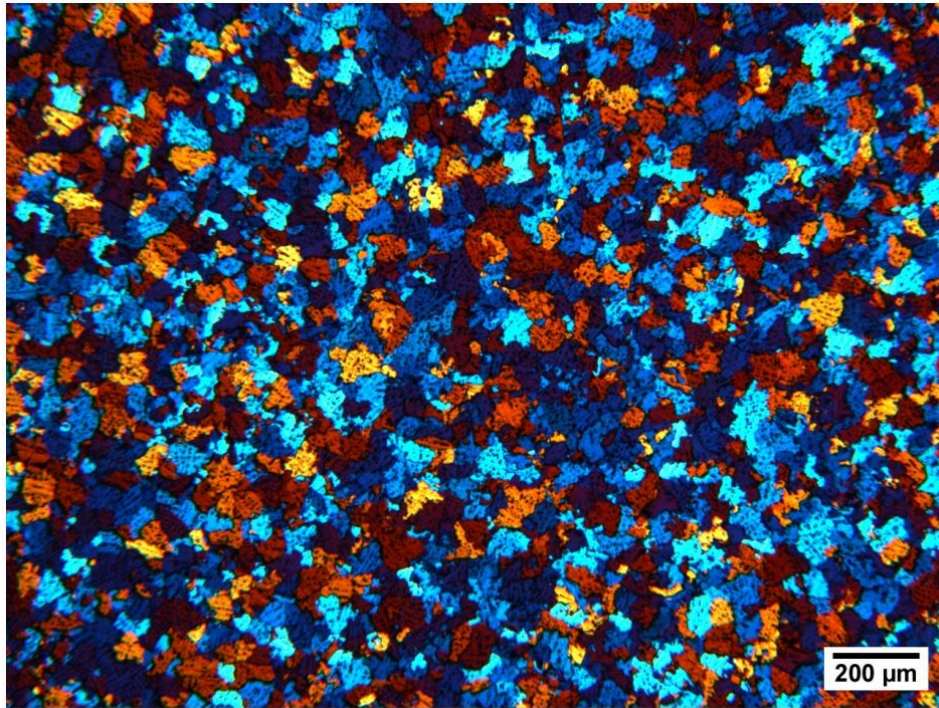


Figure 4.25: Al₃Mg_{0.4}Sc as-casted grain structure [4]

The measured cell spacing is also within the cell spacing range acquired in this study. Figure 4.26 below shows an example of age hardening effect on Al₂Mg_{0.2}Sc of samples. The cast sample used in that study was homogenized at 617°C for 24 hours after casting, and then water quenched to room temperature, followed by age hardening at 300°C. The homogenization and water quench was done to achieve a uniformly distributed Sc in aluminum alpha matrix [5].

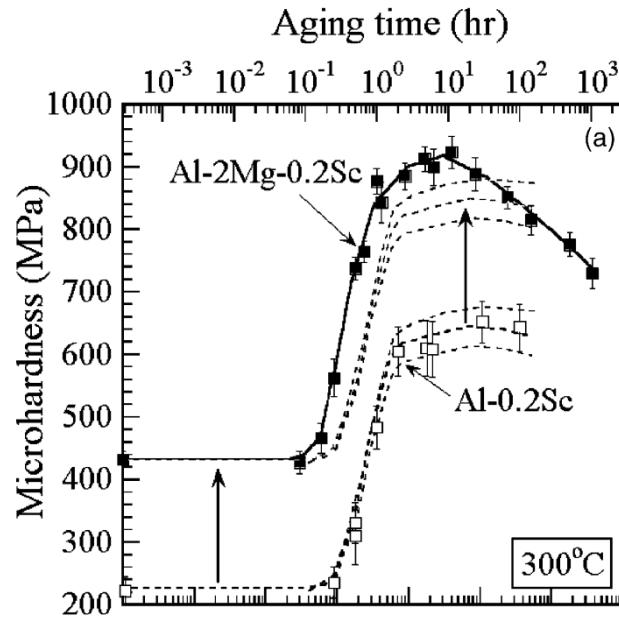


Figure 4.26: Vickers microhardness vs. aging time for Al₂Mg_{0.2}Sc at 300°C [5]

The reported Vickers microhardness unit could be converted from MPa to kgf/mm² by multiplying 9.81N/kg, which will give us 45 HV before aging and 90 HV after aging. The increase in Vickers microhardness is about 45HV. Which is comparable to what is observed in this work 30-35HV. The extra 10HV might be due to a more supersaturated condition achieved by a complete homogenization process.

4.6. Summary

The cooling rates for impulse atomized powders with Al_{1.5}Mg_{0.2}Sc and Al₃Mg_{0.2}Sc alloys are estimated to be in the range of 300K/s to 900K/s depending on different particle size. When the semi-solidified droplet deposited on the moving copper substrate, the cooling rate dropped to about 1.7K/s.

Relationships between cell spacing and cooling rate are established based on Al_{1.5}Mg_{0.2}Sc and Al₃Mg_{0.2}Sc powders. The exponential values in the equations are close to the theoretical value; for Al₃Mg_{0.2}Sc the pre-exponential constant is within the possible range of theoretical values while for Al_{1.5}Mg_{0.2}Sc it is not. The Al₃Mg_{0.2}Sc show a higher microhardness value at the same cell spacing; while for the same alloy composition, the cell spacing has a negligible effect. For spray deposited strips, the

different in atomization temperature and location along the thickness of the strip do not have an observable effect as well. Upon age hardening, both the powders and strips reach their maximum strength after aging for 2 hours at 300°C. Both of the Al1.5Mg0.2Sc and Al3Mg0.2Sc powders and strips achieved a 30-35HV increase in microhardness after aging. Their increases in hardness after aging are about the same, showing Mg addition does not have an effect on the age hardening behavior of Sc in the range of 1.5wt% to 3wt%.

Comparing these results to industrial applications, the cooling rate and resulting cell spacing range measured in this work covers the twin-belt casting process. The performance of age hardening behavior of supersaturated Sc is close to homogenized and quenched casting product.

5. Conclusions and Future Work

5.1. Conclusions

Al1.5Mg0.2Sc and Al3Mg0.2Sc powders were produced using impulse atomization. Sieve analysis shows that the size distribution of the impulse atomized powders followed a log-normal distribution. The $D_{50}/D_{\text{orifice}}$ is around 1.4. Al1.5Mg0.2Sc and Al3Mg0.2Sc spray deposited strips were produced with the use of impulse atomization technique with different atomization temperature.

Cell spacing measurements were performed on the etched powder and strip samples. It was found that the addition of Mg would refine grain size at the same cooling rate. For spray deposits, a minor grain size difference was found along the thickness. This suggests that the difference in cooling rate does not vary much along the thickness of the deposit.

Cooling rate calculated for the impulse atomized powders are in the range of 300 to 900K/s for powders in the size range of 212 μm to 1000 μm . Based on the cooling rate and cell spacing data, the relationships between these two parameters are established for both Al1.5Mg0.2Sc and Al3Mg0.2Sc. A temperature measurement setup is developed to measure the deposit-substrate interface cooling rate. By applying the cooling rate - cell spacing relationship to spray deposited Al3Mg0.2Sc atomized at 1000°C, the calculated cell spacing based on the measured cooling rate is close to the measured data.

With the microhardness measurement, the addition of Mg is found to strengthen both powders and strips by the same amount. The strengthening effect of grain refinement is limited for both Al1.5Mg0.2Sc and Al3Mg0.2Sc powders and strips. For spray deposits, the microhardness does not vary along the thickness thus showing a homogenous mechanical performance. The superheat shows little impact on microhardness rather the increase in superheat resulting in evaporation of Mg for Al3Mg0.2Sc alloys, which result in a decrease in microhardness.

Age hardening was performed on the powders and strips at 300 °C using an induction furnace. It is found that Al1.5Mg0.2Sc and Al3Mg0.2Sc could reach their maximum microhardness after 2 hours of aging. Both Al1.5Mg0.2Sc and Al3Mg0.2Sc shows an increase of 30 HV0.1 after aging. This is contributed by the 0.2wt%Sc added into the

system. Combining the DSC results with ternary phase diagrams, the precipitation behavior of Al_3Sc is further confirmed.

With the comparison made to industrial applications, it is shown that the impulse atomization and spray deposition process have the potential to simulate industrialized rapid solidification process, such as twin-belt casting. Therefore, a platform is provided to industries to develop novel alloys with less material and cost. Also, when these alloys are processed using a rapid solidification route, there is no need for solutionizing, quench and age processing steps. The cast alloys may be age hardened directly eliminating costly and time consuming processing steps.

5.2. Future Works

- In this study, the top interface temperature measurement was not able to be performed due to the technical issue of the infrared camera. It is recommended to carry on the temperature measurement with the developed setup. Moreover, some modifications such as device mounting or better operation parameters could be further developed to the current setup.
- The aging effect of Sc in $\text{Al}_{1.5}\text{Mg}_{0.2}\text{Sc}$ and $\text{Al}_{13}\text{Mg}_{0.2}\text{Sc}$ is not fully exploited. The nanometer size of Al_3Sc precipitates requires TEM to be used to visualize their size and distribution. The TEM work is suggested to be done in the future.
- For spray deposited strips, a tensile bar could be made to perform a tensile test or creep test on to characterize the products in more details.
- Both 0.2wt%Sc and 0.4wt%Sc addition to Al_{13}Mg alloys shows an excellent response to age hardening. Considering the high cost of Sc, 0.1wt%Sc addition in Al_{13}Mg alloy is worth well to be studied in the future as well.
- For a casted strip, porosity is an important parameter for the integrality of the product as well as for the difficulty of future processing. For IASD process, varying the atomization temperature and/or the distance between the nozzle plate and the copper substrate will be resulted in different droplets solid/liquid fraction upon landing. The effect of the different droplet solid/liquid fractions on the porosities, both surface porosities and internal porosities could be investigated.

References

- [1] M. Jobba, R. K. Mishra and M. Niewczas, "Flow stress and work-hardening behavior of Al-Mg binary alloys," *International Journal of Plasticity*, no. 65, pp. 43-60, 2015.
- [2] I. Polmear, *Light Alloys -- Metallurgy of the Light Metals* 3rd ed., London: Arnold, 1995.
- [3] V. I. Elagin, V. V. Zakharov and T. D. Rostove, "Scandium-alloyed aluminum alloys," *Metal Science and Heat Treatment*, vol. 34, no. 1, pp. 37-45, 1992.
- [4] M. Sohi, "Aging Behavior of Flexcast Al-Mg Alloys with Sc and Zr Additions," The University of British Columbia, Vancouver , 2012.
- [5] E. A. Marquis, D. N. Seidman and D. C. Dunand, "Effect of Mg addition on the creep and yield behavior of an Al-Sc alloy," *Acta Materialia*, vol. 51, pp. 4751-4760, 2003.
- [6] T. Herding, O. Kebler and H. W. Zoch, "Spray formed and rolled aluminum-magnesium-scandium alloys with high scandium content," *Materialwiss Werkstofftech*, vol. 38, no. 10, pp. 855-861, 2007.
- [7] R. R. Sawtell and C. L. Jensen, "Mechanical properties and microstructures of Al-Mg-Sc alloys," *Metallurgical and Materials Transactions A*, vol. 21, no. 1, pp. 421-430, 1990.
- [8] B. A. Parker, Z. F. Zhou and P. Nolle, "The effect of small additions of scandium on the properties of aluminium alloys," *Journal of Materials Science* , vol. 30, no. 2, pp. 452-458, 1995.
- [9] J. Gambogi, "Mineral Commodity Summaries," U.S. Geological Survey, Jan 2016.
- [10] H. Henein, "Single fluid atomization through the application of impulses to a melt," *Material Science Engineering A*, vol. 92, no. 326, 2002.

- [11] N. Ellendt, R. Schmidt, J. Knabe, H. Henein and V. Uhlenwinkel, "Spray deposition using impulse atomization technique," *Materials Science and Engineering: A*, vol. 383, no. 1, pp. 107-113, 2004.
- [12] J. B. Wiskel, H. Henein and E. Maire, "Solidification study of aluminum alloys using Impulse Atomization: Part I: Heat Transfer Analysis of An Atomized Droplet," *Canadian Metallurgical Quarterly*, vol. 41, no. 2, pp. 97-110, 2002.
- [13] J. B. Wiskel, K. Navel, H. Henein and E. Maire, "Solidification Study of Aluminum Alloys using Impulse Atomization: Part II. Effect of Cooling Rate on Microstructure," *Canadian Metallurgical Quarterly*, vol. 41, no. 2, pp. 193-204, 2002.
- [14] A. Sverdlin, "Introduction to Aluminum," in *Handbook of Aluminum*, vol. 1, D. S. M. George E. Totten, Ed., New York, Marcel Dekker, INC., 2003, pp. 1-32.
- [15] F. Habashi, "Extractive Metallurgy of Aluminum," in *Handbook of Aluminum*, vol. 2, D. S. M. George E. Totten, Ed., New York, Marcel Dekker, Inc., 2003, pp. 1-46.
- [16] G. Ram, D. Janaki, Y. Yang and B. E. Stucker, "Effect of process parameters on bond formation during ultrasonic consolidation of aluminum alloy 3003," *Journal of Manufacturing System*, vol. 25, no. 3, pp. 221-238, 2006.
- [17] Y. Li and D. Gu, "powder, Parametric analysis of thermal behavior during selective laser melting additive manufacturing of aluminum alloy," *Materials and Design*, vol. 63, pp. 856-867, 2014.
- [18] R. N. Caron and J. T. Staley, *Aluminum and Aluminum Alloys, Effects of Composition, Processing, and Structure on Properties of Nonferrous Alloys*, vol. Vol 20 Materials Selection and Design, ASM International, 1997, pp. 383-415.
- [19] H. Baker, "Alloy Phase Diagrams," in *ASM Handbook*, ASM International, 1992, p. Vol 3.

- [20] J. Murray, "The Al–Mg (Aluminum–Magnesium) system," *Bulletin of Alloy Phase Diagrams*, vol. 3, no. 1, pp. 60-74, 1982.
- [21] J. E. A. Starke, "Aluminum Alloys of the 70s: Scientific Solutions to Problems. An invited review.," *Materials Science and Engineering*, vol. 29, no. 2, pp. 99-115, 1977.
- [22] A. Fontaine, "Clustering Effects in Splat-Cooled Al-Transition Metal Alloys," *Rapidly Quenched Metals*, vol. 1, pp. 163-167, 1976.
- [23] M. Tiryakioglu and J. T. Staley, "Physical Metallurgy and the Effect of Alloying Additions in Aluminum Alloys," in *Handbook of Aluminum, Volume 1 Physical Metallurgy and Processes*, New York, Marcel Dekker, Inc, 2003, pp. 81-210.
- [24] R. E. Sanders, S. F. Baumann and H. C. Stumpf, "Non-Heat-Treatable Aluminum Alloys," in *Aluminum Alloys -- Physical and Mechanical Properties Vol. 1*, 1986, pp. 1441-1484.
- [25] E. L. Huskins, B. Cao and K. T. Ramesh, "Strengthening Mechanism in an Al-Mg Alloy," *Materials Science and Engineering A*, no. 527, pp. 1292-1298, 2010.
- [26] L. S. Toropova, *Advanced Aluminum Alloys Containing Scandium, Structure and Properties*, Moscow: Baikov Institute of Metallurgy, 1998.
- [27] S. Lathabai and P. G. Lloyd, "• The effect of scandium on the microstructure, mechanical properties and weldability of a cast Al–Mg alloy," *Acta Materialia*, no. 50, pp. 4275-4292, 2002.
- [28] L. Willey, "Aluminum scandium alloy". United States Patent 3619181 , 9 Nov. 1971.
- [29] J. L. Murray, "The Al-Sc (aluminum-scandium) system," *Journal of Phase Equilibria*, vol. 19, no. 4, pp. 380-384, 1998.
- [30] M. S. Kaiser, S. Datta, A. Roychowdhury and M. K. Banerjee, "Age Hardening Behavior of Wrough Al-Mg-Sc Alloy," *Materials and Manufacturing Processes*, no. 23, pp. 74-81, 2008.

- [31] Z. Ahmad, "The Properties and Application of Scandium-reinforced Aluminum," *Aluminum Composites*, pp. 35-39, 2003.
- [32] C. Watanabe, "Coarsening Behavior of Al₃Sc Precipitates in an Al-Mg-Sc Alloy," *Materials Transactions*, vol. 47, no. 9, pp. 2285-2291, 2006.
- [33] K. L. Kendig and D. B. Miracle, "Strengthening mechanisms of an Al-Mg-Sc-Zr alloy," *Acta Materialia*, no. 50, pp. 4165-4175, 2002.
- [34] F. Fazeli, W. J. Poole and C. W. Sinclair, "Modeling the effect of Al₃Sc precipitates on the yield stress and work hardening of an Al-Mg-Sc alloy," *Acta Materialia*, no. 56, pp. 1909-1918, 2008.
- [35] H.R. Shercliff, et al., "Process Modelling Applied to Age Hardening Aluminum Alloys," in *Proceedings of the Third International Conference on Aluminum Alloys*, June 1992.
- [36] T. B. Bhat and V. S. Arunchalam, "Strengthening Mechanisms in Alloys," in *Alloy Design*, Indian Academy of Science, 1981, pp. 23-44.
- [37] R. Colas, E. Velasco and S. Valtierra, "Castings," in *Handbook of Aluminum Volume 1 Physical Metallurgy and Processes*, New York, Marcel Dekker, Inc. , 2003, pp. 591-642.
- [38] M. Van Lancker, *Metallurgy of Aluminum Alloys*, New York: John Wiley & Sons Inc. , 1967.
- [39] L. A. Narayanan and F. H. Samuel, "Dissolution of iron intermetallics in Al-Si Alloys through nonequilibrium heat treatment," *Metallurgical and Materials Transactions A*, vol. 26, no. 8, pp. 2161-2184, 1995.
- [40] R. Howard, N. Bugh and D. S. MacKenzie, "Heat Treating Process and Equipment," in *Handbook of Aluminum Volume 1 Physical Metallurgy and Process*, New York, Marcel Dekker, Inc., 2003, pp. 881-970.

- [41] Arvind, "Microsegregation studies of rapidly solidified binary Al-Cu alloys," University of Alberta, Edmonton, 2006.
- [42] J. E. Hatch, "Constitution of Alloys," in *Aluminum Properties and Physical Metallurgy*, Ohio, ASM International, 1984, p. 37.
- [43] A. J. Yule and J. J. Dunkley, "10.3 Heat transfer from particles and solidification," in *Atomization of Melts: For Powder Production and Spray Deposition*, Oxford, England, Clarendon Press, 1994, pp. 281-287.
- [44] D. Yuan, *Ph.D Thesis*, Edmonton, Alberta, Canada: The University of Alberta, 1998.
- [45] J. B. Wiskel and H. Henein, *Proceedings of Fluid Flow Phenomena in Metals Processing*, N. R. D. J. S. a. V. V. El-Kaddash, Ed., TMS, Warrendale, 1999, pp. 517-524.
- [46] J. B. Wiskel, H. Deng, C. Jefferies and H. Henein, "Infrared thermography of TMCP microalloyed steel skelp at upcoiler and its application in quantifying laminar jet/skelp interaction," *Inromaking and Steelmaking*, vol. 38, no. 1, pp. 35-44, 2011.
- [47] T. B. Wolfe and H. Henein, "Characterization of arc during hardfacing in plasma transfer arc welding," *Canadian Metallurgical Quarterly*, vol. 000, no. 000, pp. 1-12, 2014.
- [48] Quantum Logic Corporation, "Theory of Operation," in *Operation Instruction for Quantum Logic Model QL3600-2B*, Westport, 1995, pp. 10.1-10.4.
- [49] Y. A. Cengel, "9-6 Combined Natural and Forced Convection," in *Heat transfer: a practical approach*, New York, McGraw-Hill, 1998, pp. 486-514.
- [50] Edmund, "75mm Dia. x 5mm Thick, 3-12 μ m AR Coated, Ge Window," Edmund, 2015. [Online]. Available: <http://www.edmundoptics.com/optics/windows-diffusers/ultraviolet-uv-infrared-ir-windows/germanium-ge-windows/64380/>. [Accessed 12 2 2015].

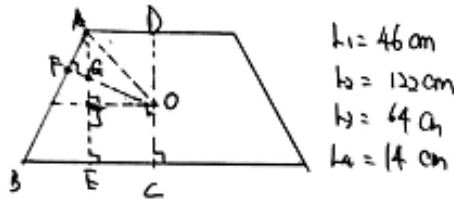
- [51] Edmund, "75mm Diameter Uncoated, Calcium Fluoride Window," Edmund, 2015. [Online]. Available: <http://www.edmundoptics.com/optics/windows-diffusers/ultraviolet-uv-infrared-ir-windows/calcium-fluoride-caf2-windows/87705/>. [Accessed 6 4 2015].
- [52] J. Taylor, "The variation with wavelength of the spectral emissivity of iron and molybdenum," *The Journal of the Optical Society of America*, vol. 42, no. 1, pp. 33-36, 1952.
- [53] F. Bierbrauer and J. Chen, "A study of the surface emissivity of oxidized steel using a three layer model," *Proc. Asia Pacific Microwave Conference*, vol. 2, pp. 11-14, 1993.
- [54] T. Iuchi, T. Furukawa and S. Wada, "Emissivity modelling of metals during the growth of oxide film and comparison of the model with experimental results," *Applied Optics*, vol. 42, no. 13, pp. 2317-2326, 2003.
- [55] LumaSense, "Pyrometer IMPAC IS 50-AL-LO plus," 2015. [Online]. Available: <http://www.lumasenseinc.com/EN/products/infrared-thermometers-and-switches/series-50/pyrometer-impac-is-50-al-lo-plus.html>. [Accessed 24 3 2015].
- [56] LumaSense, *ISR 12-LO and IGAR 12-LO Operation Manual*, LumaSense Technologies, 2009, p. 12.
- [57] P. Natzke, "Microstructural analysis of Al-Cu Spray Deposits using Impluse Atomization," Technische Universität Dresden and the University of Alberta, Dresden, Germany and Edmonton, Canada, 2014.
- [58] J. A. Sorenson and M. E. Phelps, "The Anger Camera: Performance Characteristics," in *Physics in Nuclear Medicine*, Harcourt Brace Jovanovich, Inc., p. 336.
- [59] ASTM, Standard Practice for Microetching Metals and Alloys, E407 – 07 ed., West Conshohocken: ASTM International, 2007.

- [60] M. Easton and D. StJohn, "Grain refinement of aluminum alloys: Part I. the nucleant and solute paradigms—a review of the literature," *Metallurgical and Materials Transactions A*, vol. 30, no. 6, pp. 1613-1623, June 1999.
- [61] K. T. Kashyap and T. Chandrashekar, "Effects and mechanisms of grain refinement in aluminum alloys," *Bulletin of Material Science*, vol. 24, no. 4, pp. 345-353, 2001.
- [62] P. Khatibi, "Ph.D. Thesis: Microstructure investigation of D2 tool steel during rapid solidification," The University of Alberta, Edmonton, Alberta, Canada, Spring 2014.
- [63] C.-D. Wen and I. Mudawar, "Modeling the effects of surface roughness on the emissivity of aluminum alloys," *International Journal of Heat and Mass Transfer*, vol. 49, pp. 4279-4289, 2006.
- [64] W. Kurz and D. J. Fisher, in *Fundamentals of Solidification*, Trans Tech, 1989, pp. 85-87.
- [65] Y. Du, "Diffusion coefficients of some solutes in fcc and liquid Al: Critical evaluation and correlation," *Material Science and Engineering*, vol. A, no. 363, pp. 140-151, 2003.
- [66] D. Stefanescu, "Equilibrium and non-equilibrium during solidification," in *Science and Engineering of Casting Solidification, 2nd Edition*, Columbus, Springer, 2002, pp. 5-24.
- [67] J. O. Andersson, T. Helander, L. Höglund, P. F. Shi and B. Sundman, *Thermo-Calc Software TTAL7 database*, 2002.
- [68] T. Suzuki, S. Takeuchi and H. Yoshinaga, "Dislocation dynamics and plasticity," *Springer Series in Materials Science*, vol. 12, pp. 32-44, 1990.
- [69] D. J. Lloyd and S. A. Court, "Influence of grain size on tensile properties of Al-Mg alloys," *Materials Science and Technology*, vol. 19, no. 10, pp. 1349-1354, 2003.

- [70] M. Bedel, G. Reinhart, A. -A. Bogno, C. -A. Gandin, S. Jacomet, E. Boller, H. Nguyen-Thi and H. Henein, "Characterization of dendrite morphologies in rapidly solidified Al-4.5w.% Cu droplets," *Acta Materialia*, vol. 89, pp. 234-246, 2015.
- [71] S. Yutaka, "Microstructural Factors Governing Hardness in Friction-Stir Welds of Solid-Solution-Hardened Al Alloys," *METALLURGICAL AND MATERIALS TRANSACTIONS A*, vol. 32A, p. 3042, 2001.
- [72] M. S. Kaiser, S. Datta, A. Roychowdhury and M. K. Banerjee, "Age hardening Behavior of Wrought Al-Mg-Sc Alloy," *Materials and Manufacturing Processes*, vol. 23, no. 1, pp. 74-81, 2007.
- [73] E. A. Marquis and D. N. Seidman, "Coarsening kinetics of nanoscale Al₃Sc precipitates in an Al-Mg-Sc alloy," *Acta Materialia*, vol. 53, pp. 4259-4268, 2005.
- [74] M. A. Kerkove, T. D. Wood, P. G. Sanders, S. L. Kampe and D. Swenson, "The diffusion Coefficient of Scandium in Dilute Aluminum-Scandium Alloys," *Metallurgical and Materials Transactions A*, vol. 45, no. 9, pp. 3800-3805, June 2014.
- [75] P. Z. Zhao, T. Anami, I. Okamoto, K. Mizushima, K. Gatenby, M. Gallerneault, S. Barker, K. Yasunaga, A. Goto, H. Kazama and N. Hayashi, "Development of twin-belt cast AA5XXX series aluminum alloy materials for automotive sheet applications," *TMS*, pp. 11-17, 2009.

Appendix

Calculations for θ and h



$$\begin{aligned} l_1 &= 46 \text{ cm} \\ l_2 &= 122 \text{ cm} \\ h_2 &= 64 \text{ cm} \\ L_4 &= 14 \text{ cm} \end{aligned}$$

$$AD = \frac{1}{2}l_1 = 23 \text{ cm}, \quad AE = H = 51.5 \text{ cm}$$

$$BC = \frac{1}{2}l_2 = 61 \text{ cm}, \quad AF = L_4 = 14 \text{ cm}, \quad AB = L_4 = 64 \text{ cm}$$

$$\therefore BE = BC - AD = 38 \text{ cm} \Rightarrow \angle BAE = \arcsin \frac{BE}{AB} = \arcsin \frac{38}{64} = 36.4^\circ$$

$$\therefore \angle AFG = \angle AEB = 90^\circ$$

$$\angle AFG = \angle BAE$$

$$\therefore \triangle ABE \sim \triangle AFG$$

$$\therefore \frac{AG}{AB} = \frac{AF}{AE} = \frac{GF}{BE}$$

$$\therefore \frac{AG}{64 \text{ cm}} = \frac{14 \text{ cm}}{51.5 \text{ cm}} = \frac{GF}{38 \text{ cm}}$$

$$\therefore \begin{aligned} AG &= 17.4 \text{ cm} \\ GF &= 10.3 \text{ cm} \end{aligned}$$

$$\therefore \angle AFG = \angle GJG = 90^\circ$$

$$\angle AGF = \angle JGQ$$

$$\therefore \triangle AFG \sim \triangle JGQ$$

$$\therefore \angle GQJ = \angle FAG = \angle BAE = 36.4^\circ$$

$$\therefore \angle GQD = 90^\circ - \angle GQJ = 90^\circ - 36.4^\circ$$

$$\boxed{\begin{aligned} \therefore \angle GQD &= 53.6^\circ > 40^\circ \\ \rightarrow \text{Measuring angle} \end{aligned}}$$

$$\therefore \triangle AFG \sim \triangle JGQ$$

$$\therefore \frac{GJ}{GF} = \frac{QJ}{GF} = \frac{AD}{BF}$$

$$\therefore \frac{GJ}{10.3 \text{ cm}} = \frac{23 \text{ cm}}{14 \text{ cm}}$$

$$\therefore GJ = 16.9 \text{ cm}$$

$$\therefore AJ = AG + GJ = 17.4 \text{ cm} + 16.9 \text{ cm}$$

$$AJ = 34.3 \text{ cm}$$

$$\therefore h = JE = AE - AJ = 51.5 \text{ cm} - 34.3 \text{ cm}$$

$$\boxed{h = 17.2 \text{ cm}}$$

Calibration profile for K-type thermocouples

University of Alberta
Instrument Shop Calibration

Date		T/C	Description	SV	Actual	T/C	Error	Professor
11/4/2015	0.040" Ktc	2012-41	20" long, 0.040" dia.	50	49.99	49.45	-0.54	Inst Shop
11/4/2015	0.040" Ktc	2012-41	20" long, 0.040" dia.	100	100	99.65	-0.35	Inst Shop
11/4/2015	0.040" Ktc	2012-41	20" long, 0.040" dia.	150	150.01	150.61	0.6	Inst Shop
11/4/2015	0.040" Ktc	2012-41	20" long, 0.040" dia.	200	199.99	200.91	0.92	Inst Shop
11/4/2015	0.040" Ktc	2012-41	20" long, 0.040" dia.	250	250.01	250.77	0.76	Inst Shop
11/4/2015	0.040" Ktc	2012-41	20" long, 0.040" dia.	300	299.98	300.41	0.43	Inst Shop
11/4/2015	0.040" Ktc	2012-41	20" long, 0.040" dia.	350	350.02	350.33	0.31	Inst Shop
11/4/2015	0.040" Ktc	2012-41	20" long, 0.040" dia.	400	400.06	400.43	0.37	Inst Shop
11/4/2015	0.040" Ktc	2012-41	20" long, 0.040" dia.	50	49.99	49.65	-0.34	Inst Shop
11/4/2015	0.040" Ktc	14-032	20" long, 0.040" dia.	50	49.99	50	0.01	Inst Shop
11/4/2015	0.040" Ktc	14-032	20" long, 0.040" dia.	100	100	100.47	0.47	Inst Shop
11/4/2015	0.040" Ktc	14-032	20" long, 0.040" dia.	150	150.01	150.74	0.73	Inst Shop
11/4/2015	0.040" Ktc	14-032	20" long, 0.040" dia.	200	199.99	200.33	0.34	Inst Shop
11/4/2015	0.040" Ktc	14-032	20" long, 0.040" dia.	250	250.01	250.09	0.08	Inst Shop
11/4/2015	0.040" Ktc	14-032	20" long, 0.040" dia.	300	299.98	299.69	-0.29	Inst Shop
11/4/2015	0.040" Ktc	14-032	20" long, 0.040" dia.	350	350.02	349.49	-0.53	Inst Shop
11/4/2015	0.040" Ktc	14-032	20" long, 0.040" dia.	400	400.06	399.52	-0.54	Inst Shop
11/4/2015	0.040" Ktc	14-032	20" long, 0.040" dia.	50	49.99	50.15	0.16	Inst Shop